MECHANICAL CONDITIONS BENEATH A SURGE-TYPE GLACIER

by

URS HEINRICH FISCHER

M.Sc., Trent University, 1989

B.Sc. (Honours), Trent University, 1986

Bacchalaureus-Diplom, Albert-Ludwigs-Universität, 1984

A THESIS SUBMITTED IN PARTIAL FULFILLMENT OF

THE REQUIREMENTS FOR THE DEGREE OF

DOCTOR OF PHILOSOPHY

in

THE FACULTY OF GRADUATE STUDIES

Department of Geophysics and Astronomy

We accept this thesis as conforming

to the required standard

THE UNIVERSITY OF BRITISH COLUMBIA

April 1995

In presenting this thesis in partial fulfilment of the requirements for an advanced degree at the University of British Columbia, I agree that the Library shall make it freely available for reference and study. I further agree that permission for extensive copying of this thesis for scholarly purposes may be granted by the head of my department or by his or her representatives. It is understood that copying or publication of this thesis for financial gain shall not be allowed without my written permission.

(Signature)

Department of _Geophysics & Astronomy_

The University of British Columbia
Vancouver, Canada

Date _April 25, 1995_

DE-6 (2/88)

ABSTRACT

The interaction of basal processes with the subglacial drainage system is a critical issue in understanding glacier dynamics. This is especially true for glaciers that exhibit a flow instability known as "surging", characterized by cyclical alternation between slow and fast flow regimes. It is accepted that sustained high subglacial water pressure causes glacier surging by decoupling the glacier from its bed, but how basal hydrological conditions control coupling at the ice–bed interface remains the subject of debate.

I have applied new investigative techniques for measuring basal sliding and exploring mechanical conditions of the subglacial material at Trapridge Glacier, a small surge-type glacier in the St. Elias Mountains, Yukon Territory, Canada. The data presented in this thesis are unique and important because they were obtained directly at the glacier bed using new subglacial sensors, designed and constructed at the University of British Columbia. Basal sliding is measured with a "drag spool" which consists of a multi-turn potentiometer connected to a spooled string. The drag spool is suspended within the borehole close to the glacier bed, and measures continuously the length of string payed out to an anchor in the bed. Mechanical interactions between the glacier and its bed are sensed with a device, dubbed a "ploughmeter", which is essentially a steel rod instrumented with strain gauges. The ploughmeter is installed at the bottom of a borehole with its tip protruding into subglacial sediment, and measures the bending moment acting near the rod tip which is dragged through the sediment as a result of glacier sliding.

Field data from the drag spool instruments show that, during the melt season, basal sliding can account for up to 45–65% of the total flow observed at the glacier surface. The contribution from ice creep is known to be small, so most of the remaining surface motion must be attributed to subglacial sediment deformation. Ploughmeter measurements reveal a spatial variability in subglacial processes or sediment texture. Quantitative analysis of the interaction of the ploughmeter with the basal layer yields

estimates of rheological parameters. If the sediment is assumed to behave as a Newtonian viscous fluid, the estimated effective viscosity is 3.0×10^9–3.1×10^{10} Pa s; if it is assumed to behave as an ideal plastic solid, the estimated yield strength is 48–57 kPa. For clast-rich sediments, the rate of collision between clasts and the ploughmeter provides us with an estimated basal sliding rate of 30–50 mm d^{-1}, in good agreement with the drag spool results.

Diurnal signals recorded with both types of instruments appear to be correlated to fluctuations in subglacial water pressure. These diurnal variations in the response of both instruments can be interpreted in terms of changes in sliding velocity and basal resistance as the mechanical conditions at the glacier bed vary in response to changes in the subglacial water system. I have developed theoretical models that describe the sliding motion of ice over a surface with variable basal drag and have demonstrated how the models can be used in numerical simulations to generate data, which can be compared with my field observations. The results from my model calculations provide strong evidence for time-varying sticky spots and for stick–slip sliding motion, both of which are linked to changes in basal lubrication in response to fluctuations in subglacial water pressure.

TABLE OF CONTENTS

LIST OF FIGURES

LIST OF TABLES

LIST OF SYMBOLS

a	radius, minor semi-axis (m)
a^+, a^-, $a^\pm$	slope of drag coefficient function
A	area of part of glacier bed (m^2)
A_i	fitted signal amplitude (V)
b	constant, $b = D/3$
b^+, b^-, $b^\pm$	intercept of drag coefficient function
B	Glen Flow Law parameter (s^{-1} Pa^{-3})
B_i	fitted azimuth offset (°)
c	major semi-axis (m)
C	constant of proportionality
C_i	fitted voltage offset (V)
D	fractal dimension
D_c	fractal dimension (cumulative statistics)
D_E	Euclidian dimension
D_T	topological dimension
E	Young's modulus (Pa)
f	drag coefficient (Pa s m^{-1})
f^A	drag coefficient in connected region of glacier bed (Pa s m^{-1})
f^A_{max}	maximum drag coefficient in connected region (Pa s m^{-1})
f^A_{min}	minimum drag coefficient in connected region (Pa s m^{-1})
f^A_{trig+}	drag coefficient at p_W^{max} (upper line) (Pa s m^{-1})
f^A_{trig-}	drag coefficient at p_W^{min} (lower line) (Pa s m^{-1})
f^B	drag coefficient in unconnected region of glacier bed (Pa s m^{-1})
f^0	background component of drag coefficient (Pa s m^{-1})
f'	perturbation component of drag coefficient (Pa s m^{-1})

f'_+, f'_-	peak perturbation drag coefficient $(\mathrm{Pa\,s\,m^{-1}})$
$\widetilde{f}'$	Fourier transform of f'
f_T	frequency $(\mathrm{s^{-1}})$
f_λ	spatial frequency $(\mathrm{m^{-1}})$
F	force per unit length $(\mathrm{N\,m^{-1}})$
F_D	drag force (N)
F_L	load force (N)
F_i	force coordinates (N)
F_s	static friction force (N)
g	gravitational acceleration $(\mathrm{m\,s^{-2}})$
G_f	gauge factor
G_I	shear modulus of ice (Pa)
G_S	shear modulus of substrate (Pa)
h_I	thickness of glacier ice (m)
h	linear dimension of fractal cube
I	second moment of cross-sectional area $(\mathrm{m^4})$
k, k_x, k_y	wavenumber $(\mathrm{m^{-1}})$
k_P	plastic yield strength (Pa)
k_S	spring constant $(\mathrm{N\,m^{-1}})$
ℓ	length of strained material (m)
L	characteristic length scale
L_i	load (N)
L_I	strain equilibration distance in ice (m)
L_S	strain equilibration distance in substrate (m)
L_x, L_y	linear dimensions of area A of glacier bed (m)
m	mass (kg)
M	bending moment $(\mathrm{N\,m})$

n	flow law exponent
N, N_n	number of objects
N_{nc}	number of objects (cumulative statistics)
N_x, N_y	number of grid points
p	fluid pressure (Pa)
p_W	subglacial water pressure (m(H$_2$O))
p_W^{max}	maximim subglacial water pressure (m(H$_2$O))
p_W^{min}	minimim subglacial water pressure (m(H$_2$O))
p_W^{trig+}, p_W^{trig-}	threshold level for slip initiation (m(H$_2$O))
r, r_n	linear dimension of object (m)
r_0	characteristic distance (m)
$\mathbf{r}$	distance (m)
$\mathbf{r}^\star$	dimensionless distance
$R_1...R_4$	strain gauge resistance (Ω)
S	surface
$S(f_T), S(f_\lambda)$	spectral density function
t	time (s)
t_0	characteristic time (s)
$t^\star$	dimensionless time
T	time interval (s)
u	distance from neutral surface (m)
U	translational velocity (m s^{-1})
$\mathbf{U}$	translational velocity field (m s^{-1})
v	sliding velocity (m s^{-1})
v_b	basal sliding velocity (m s^{-1})
v_i	velocity coordinates (m s^{-1})
v_s	shear wave velocity (m s^{-1})

$v_{\mathrm{b}}^0,\ v_x^0$	background component of basal sliding velocity $(\mathrm{m\,s^{-1}})$
v_{b}'	perturbation component of basal sliding velocity $(\mathrm{m\,s^{-1}})$
v_0'	characteristic velocity $(\mathrm{m\,s^{-1}})$
$\mathbf{v}'$	perturbation velocity field $(\mathrm{m\,s^{-1}})$
$\mathbf{v}'^{\star}$	dimensionless velocity field
V	volume $(\mathrm{m^3})$
$\widetilde{\mathbf{V}}'$	Fourier transform of $\mathbf{v}'$
$\widetilde{V}_i'$	Fourier transform of v_i'
V_{out}	output voltage (V)
V_{in}	input voltage (V)
$w_x,\ w_y$	width of blocks representing sticky spots (m)
x	horizontal coordinate, $x = x_1$ (m)
$x(t)$	time domain function
x_i	spatial coordinates (m)
$\mathbf{x}$	position vector, distance (m)
X	Fourier transform of $x(t)$
y	horizontal coordinate, $y = x_2$ (m)
z	vertical spatial coordinate, $z = x_3$ (m)
z_{g}	vertical coordinate of strain gauge (m)
α	area fraction of connected region of glacier bed
$\alpha_{\mathrm{T}},\ \alpha_\lambda$	spectral intercept
β	spectral slope
γ	rescaling factor
δ	transition zone for ice slip $(\mathrm{m(H_2O)})$
δ_{ij}	Kronecker delta
ϵ	bending strain
$\dot{\epsilon}_{ij}$	strain rate tensor $(\mathrm{s^{-1}})$

η	dynamic viscosity of ice (Pa s)
μ	fluid viscosity, effective viscosity of till (Pa s)
ν	kinematic viscosity ($m^2 s^{-1}$)
ϕ	azimuth angle (°)
θ	surface slope of glacier (°)
ρ_I	density of ice ($kg\,m^{-3}$)
ρ_S	density of substrate ($kg\,m^{-3}$)
σ	bending stress (Pa)
σ^A	shear stress in connected region of bed (Pa)
σ^B	shear stress in unconnected region of bed (Pa)
σ_{ij}	stress tensor (Pa)
$\tilde{\sigma}'_{xz}$	Fourier transform of τ'_b
τ_b, σ_{xz}	basal shear stress (Pa)
τ_b^0	background component of basal shear stress (Pa)
τ_b'	perturbation component of basal shear stress (Pa)

ACKNOWLEDGEMENTS

To my parents, Hildegard and Alexander,
who gave me the motivation to attempt a task such as this, yet never
precisely knew what I was doing out there in the world of ice.

I find great pleasure in acknowledging the help which I received from many sources. Particular thanks are due to my supervisor, Garry Clarke, whose thoughtful guidance, creative thinking and continued encouragement have contributed immeasurably to this study. His enthusiasm is contagious, and it is a delight to work with him. Perhaps one of Garry's greatest attributes is his open-minded support: *Mens sana in corpore sano* — he never discouraged me in my pursuit of other, non-academic interests, but instead seemed rather suprised to find me working at my desk on occasional weekends ("Did you break your skis?").

I was very fortunate in being able to share the excitement and frustrations of field oriented research with a dedicated and diverse group of people. I acknowledge all those who assisted in the field and contributed intellectual insights to this study, especially, Brian Waddington, Shawn Marshall, Tavi Murray, Erik Blake, Dan Stone, Mathew Jull and Barry Narod. I also thank Colin Farquharson who endured endless discussions on many mathematical details ("Is a factor of $\pi/2$ really crucial?"). Critical scientific advice and guidance throughout the course of this research were given by my supervisory committee members Bob Ellis, Rosemary Knight and Don Russell. I express my gratitude to Dieter Schreiber for his technical assistance in the design and construction of subglacial instruments.

I have made good friends on my long and winding path to the completion of my thesis. I am grateful to all of them for always being ready to help when I needed it and for sharing many happy times with me. Of those not already mentioned above, I express my appreciation especially to Jane Rea ("I can't believe you boys went to see that movie!"), Phil Hammer, Karl Butler, Dave Butler, Martyn Unsworth and Laurent Mingo. Finally, the entire staff, faculty and student body of the Department of Geophysics and Astronomy is second-to-none for providing an interesting and pleasant working and social environment which makes this a truly wonderful place to be.

2.

Chapter 1

INTRODUCTION

"Wanted for hazardous journey. Small wages, bitter cold, ..., constant danger, safe return doubtful. Honour and recognition in case of success."

- Ernest Shackleton

The geometry, velocity and stability of glaciers and ice sheets are, in large part, determined by how flowing ice interacts with the subglacial bed. The bed may be rugged so that ice must flow over and around obstacles. There may be spatial or temporal variations in the subglacial drag such that at some places or times ice can slide easily and at others hardly at all. Because of the inaccessibility of the bed, conditions and processes prevailing beneath ice masses are difficult to study and therefore poorly understood. These uncertainties plague all current numerical models of ice sheet behaviour.

Soft-bedded glaciers and ice sheets flow by some combination of ice creep, basal sliding and subglacial sediment deformation (Alley, 1989). Most studies of glacier motion have tended to measure spatial and temporal variations in surface motion and interpreted velocity variations in terms of changes in basal motion (Iken and others, 1983; Kamb and others, 1985, 1994; Iken and Bindschadler, 1986; Kamb and Engelhardt, 1987; Meier and others, 1994). There have been few studies that have attempted to identify the relative contributions of ice deformation and basal motion to the overall surface velocity. Notable exceptions are the work of Raymond (1971) on Athabasca Glacier and of Hooke and others (1987, 1992) on Storglaciären. The processes that control coupling at the ice–bed interface, and thus partitioning between sliding and sediment deformation, are even less completely understood. It is generally accepted that there is a strong correlation between subglacial water pressures

and both sliding (Kamb and others, 1985; Iken and Bindschadler, 1986; Kamb and Engelhardt, 1987, Hooke and others, 1989) and sediment deformation (Boulton and Hindmarsh, 1987; Iverson and others, 1995). Increased sliding rates can result from the submergence of roughness features since high water pressures promote separation of the ice from the bed (Weertman, 1964; Kamb, 1970; Lliboutry, 1979), whereas high pore water pressures reduce the shear strength of sediment allowing increased deformation rates (Boulton and others, 1974). Thus, the basal water system is expected to play a crucial role in controlling the mechanics of glacier and ice sheet motion. However, the complex links between changes in subglacial water pressure and variations in basal drag, sliding and sediment deformation require further study. In this thesis we describe an investigation of the interactions between hydrological and mechanical conditions at the ice–bed interface of a surge-type glacier.

1.1 Glacier surging

Surge behaviour as described by Meier and Post (1969) is characterized by a two-phase cyclic flow instability involving a period of accelerated velocities (surge) and a period of stagnation in the lower glacier and thickening in the upper reaches (quiescence). During a surge, ice flow rates increase by more than an order of magnitude and large volumes of ice are rapidly transported from an upglacier reservoir area to a downglacier receiving area. The active surge phase represents only a relatively short portion of the total cycle, usually lasting between one and six years; the intervening quiescent phase may typically last from 15 to 100 years. Glaciers that surge appear to do so repeatedly.

Roughly four percent of contemporary glaciers are known to surge (Sharp, 1988); their geographical distribution is, however, markedly non-random (Post, 1969; Clarke and others, 1986; Raymond, 1987). Notable concentrations of surge-type glaciers are found in the mountain ranges of Alaska, Yukon Territory and northwestern British Columbia (Clarke and others, 1986), the Canadian Arctic Archipelago, the Pamirs,

the Tien-Shan, the Caucasus, the Karakoram, the Andes, Svalbard, Iceland and East Greenland (Paterson, 1994, p. 358), whereas they are virtually absent in other areas such as the Alps, Scandinavia and the Rocky Mountains (Sharp, 1988). The geographical clustering of surge-type glaciers suggests that environmental factors have an influence on surging. Post (1969) considered obvious factors such as climatic conditions, geologic setting, glacier geometry and thermal regime but failed to explain the control on surging. He proposed that a likely explanation of the non-random distribution of surging glaciers involves distinctive subglacial conditions, such as the roughness and permeability characteristics of glacier beds, a subject about which very little is known. Clarke and others (1986) and Clarke (1991) used statistical analysis to pursue the question of a geometrical influence and concluded that glacier length correlates strongly with surge behaviour.

Although well-documented, surges remain incompletely explained. There is wide agreement that surges involve interaction between the subglacial hydrological system and sliding processes. High subglacial water pressure decouples the glacier from its bed and thereby promotes rapid flow. This high water pressure is believed to result from the disabling of the normal subglacial drainage system causing increased water storage. Outstanding questions concern the basal processes that trigger hydrological changes and control coupling at the ice–bed interface.

1.2 The ice–bed interface

Physical conditions beneath glaciers and ice sheets lying on unlithified material can be complex. Sediment is inhomogeneous and rheologically complex; influential parameters such as effective pressure can vary both spatially and temporally. If the sedimentary bed is frozen to the overlying ice, slip motion is inhibited and ice is strongly coupled to the bed. Strong coupling can also result from ice infiltrating unfrozen sediment; this process is promoted by low pore water pressure within the bed (Shoemaker, 1986;

Boulton and Hindmarsh, 1987; Iverson, 1993). Alternatively, complete decoupling of ice and sediment can result from the presence of a water layer at the interface (Shoemaker, 1986; Lingle and Brown, 1987). If the bed is incompletely coupled to overlying ice, both sliding and sediment deformation can contribute to glacier motion. When clasts protrude across an interface between partially coupled ice and sediment, ploughing of the substrate can occur (Brown and others, 1987).

1.2.1 Previous investigations of basal conditions

Despite the difficulty of making observations at the base of glaciers, numerous studies of processes and conditions at the ice–bed interface have been performed. Initially, these studies were confined to easily accessible parts of glaciers not flooded by subglacial streams and where the overlying ice is comparatively thin. Early observations of basal sliding were carried out in deep, marginal crevasses (Carol, 1947), in natural subglacial cavities (Vivian and Bocquet, 1973; McKenzie and Peterson, 1975) and in tunnels excavated in the marginal regions of glaciers (Haefeli, 1951; McCall, 1952; Kamb and LaChapelle, 1964, 1968). Tunnels were also used to access basal sediments, allowing the measurement of deformation rates (Boulton and Jones, 1979; Boulton and Hindmarsh, 1987). The advent of hot-water drilling permitted borehole access in central regions of glaciers where basal conditions are probably more characteristic of the bed as a whole. This development has allowed photographic observations of basal sliding and conditions (Harrison and Kamb, 1970, 1973; Engelhardt and others, 1978; Kamb and others, 1979) and the retrieval of sediment samples (Engelhardt and others, 1990a; Clarke and Blake, 1991). It has also enabled the emplacement of sensors to measure directly the deformation of the substrate (Blake and Clarke, 1989; Kohler and Proksch, 1991; Blake and others, 1992; Iverson and others, 1995), the shear strength of sediments (Humphrey and others, 1993; Fischer and Clarke, 1992, 1994a; Iverson and others, 1994, 1995) and the sliding of ice over unlithified material (Boulton and

Hindmarsh, 1987; Blake and Clarke, 1989; Kamb and Engelhardt, 1989; Engelhardt and others, 1990b; Blake and others, 1994; Fischer and Clarke, 1993, 1994b).

1.3 Trapridge Glacier

Our study was performed on Trapridge Glacier, a surge-type glacier located within the Steele Creek drainage basin in the northern St. Elias Mountains, Yukon Territory, Canada (Fig. 1.1). The glacier last surged sometime between 1941 and 1949 and is currently believed to be in the late stages of its quiescent phase. Trapridge Glacier is small (length $\approx 4\,\mathrm{km}$, width $\approx 1\,\mathrm{km}$), relatively thin (depth ≈ 70–$80\,\mathrm{m}$) and presently ranges in elevation from roughly $2200\,\mathrm{m}$ to $2900\,\mathrm{m}$ (Clarke and Blake, 1991). Over much of its ablation area, the surface and basal slopes are both 7° in the direction of glacier flow. Over the past decade, the mean annual flow rate has varied somewhat from year to year, ranging from $80\,\mathrm{mm\,d^{-1}}$ to $100\,\mathrm{mm\,d^{-1}}$ (Waddington, 1992). The direction of ice flow is nearly due east and the glacier terminus has formed a cliff that we refer to as "the bulge". The glacier rests on a deforming sediment substrate (Blake, 1992; Blake and others, 1992) which is thought to be water-saturated (Stone, 1993). The substrate is believed to be up to $\sim 10\,\mathrm{m}$ thick in places (Stone, 1993) of which the top $0.5\,\mathrm{m}$ is assumed to be deforming (Blake and Clarke, 1989). The thermal regime of Trapridge Glacier is sub-polar (Clarke and Blake, 1991; Clarke and others, 1984); the temperature in the upper layers is subfreezing and warms to the melting point at the base. The warm-based zone is bounded downslope by a margin of cold-based ice.
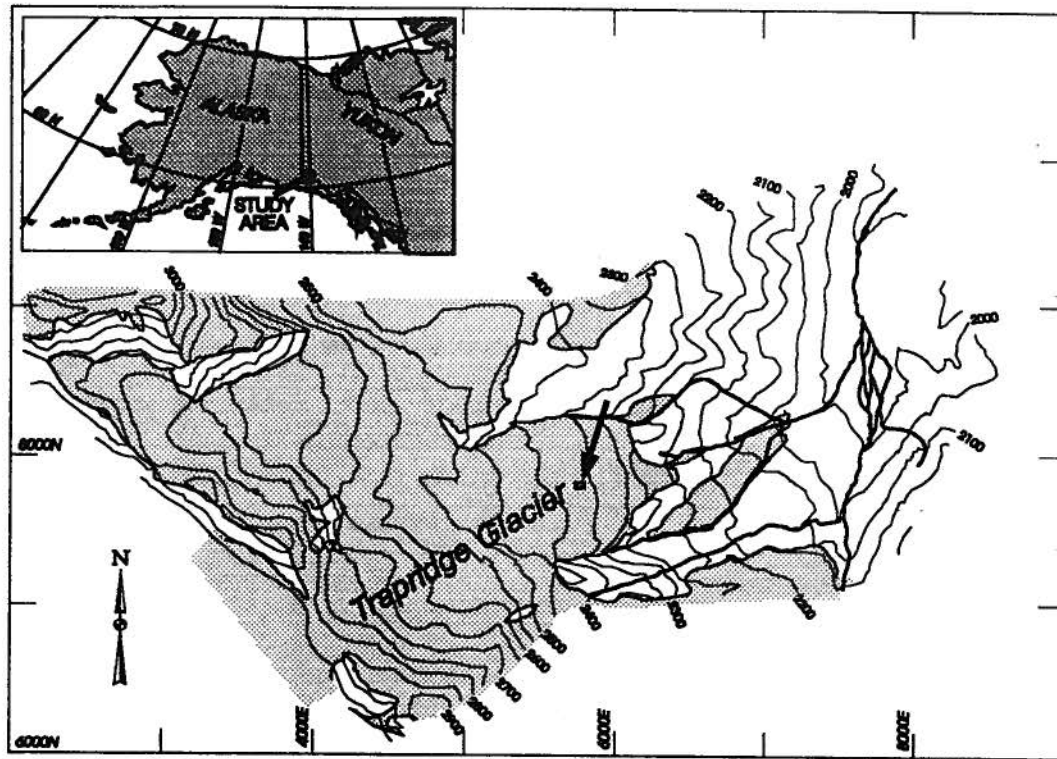
Fig. 1.1: Trapridge Glacier study site. Topographic map of Trapridge Glacier showing the entire catchment area. The shaded area represents glacier ice, based on 1981 photogrammetric mapping (Canadian Government photographs A25841-34,36). The glacier has advanced about 300 m since that time. The rectangular box indicates the area in which data discussed in this thesis were collected. Inset shows a location map of the study site in western Yukon Territory, Canada.

1.4 Thesis overview

A persistent question is what processes control the coupling of ice to the underlying sediment at the base of glaciers. Without new instruments and extensive subglacial measurements, it is doubtful that this question can be settled. To this end, we have developed new instruments to measure basal sliding and sense the mechanical interaction between a glacier and its bed. The first of these instruments, which we term a "drag spool", was originally developed by Erik Blake (Blake, 1992; Blake and others, 1994)

and deployed during the 1990 field season. The second instrument has been named a "ploughmeter" and was designed and constructed especially for this study.

In this thesis, we describe the construction, calibration, field operation and interpretation theory of the two types of instruments. Analysis of ploughmeter data from the 1991 field season, in which we interpret our observations in terms of a translational motion through a homogeneous, fine-grained substrate, enabled us to quantify rheological parameters for the sediment layer beneath Trapridge Glacier. These estimates provide the first continuous *in situ* determinations of effective viscosity and yield strength of subglacial material. For a heterogeneous or clast-rich sediment, the linear viscous assumption is clearly inappropriate and we introduce the concept of clast collision frequency to describe the ploughmeter response. We further demonstrate that the particle-size distribution of Trapridge sediment is fractal, a fact which is used to examine the self-similar character of the ploughmeter response spectrum. If the subglacial sediment texture is known and assumed to be spatially and temporally homogeneous, the collision frequency as indicated by a ploughmeter can be related to the basal sliding rate.

Measurements of subglacial water pressure, basal sliding and ploughmeter response were simultaneously recorded during the 1992 field season. These measurements confirm that the interaction of basal processes with the subglacial hydrological system is complex. The drag spool and ploughmeter records appear to be correlated to fluctuations in subglacial water pressure. This correlation suggests that mechanical conditions at the bed vary temporally in response to changes in the basal water system. We develop a theoretical framework for the sliding motion of ice over a surface with temporal and spatial variations in basal drag. We subsequently show how we can apply our theoretical models by numerically generating instrument responses which we can then compare to field data. Interpretation of our model results leads to a qualitative characterization of the basal stress system.

The original aspiration of this study was simultaneously to measure basal sliding, subglacial strain, sediment strength and subglacial water pressure. For three consecutive field seasons, we battled the difficulties associated with installing and operating arrays of drag spools, tilt sensors, ploughmeters and pressure transducers. Recording data using these four types of instruments at the same location and over the same time period is an important requirement for a comprehensive analysis. Due to the short life span and proneness to failure of some of our devices, in particular the tilt sensors, we never succeeded in making simultaneous measurements involving all four types of instruments for any significant length of time. We were nevertheless able to identify fundamental aspects of the coupling process at the ice–bed interface but a comprehensive study using all four types of instruments remains on the agenda for the Trapridge Glacier project.

All of the material from Chapter 2 and portions of Chapter 5, which deals with description of and measurements using drag spools, appeared recently in the *Journal of Glaciology* (Fischer and Clarke, 1994a; Blake and others, 1994). The substance of Chapter 3 discussing clast collision frequency and estimation of basal sliding rate is currently under review by that journal.

Chapter 2

PLOUGHING OF SUBGLACIAL SEDIMENT

"They [ploughmen] are so inattentive, as to leave good soil in some places,
and turn up till in others."

<div align="right">

- A. Dickson, 1765

</div>

2.1 Introduction

For a glacier resting on a deformable bed, both sliding and subglacial sediment deformation can contribute to total basal motion (Alley, 1989). Because the operation of these processes depends upon contact conditions at the ice–bed interface, the mechanical and hydrological coupling between a glacier and its bed are topics of interest. A review of observations of processes at the ice–bed interface reported previously in the literature is given in Chapter 1. Of special relevance to the study presented in this chapter is the work of Humphrey and others (1993) who described an *in situ* measurement of the strength of deforming subglacial sediment. Their analysis was based on an examination of the plastic deformation of a drill stem that was inadvertently stuck in the bed of Columbia Glacier, Alaska.

At Trapridge Glacier, Yukon Territory, we are examining processes that control partitioning between bottom sliding and sediment deformation by observing how these flow contributions vary spatially and temporally. By simultaneously measuring subglacial water pressure we seek to quantify the relation between hydrological conditions at the glacier bed and the mode of basal motion.

For the 1991 field season, we devised a new sensor, dubbed a "ploughmeter", that complements our sensors for measuring subglacial strain (Blake and others, 1992) and glacier sliding (see Chapter 5). The device consists of a steel rod with strain

<div align="center">

9

</div>

gauges bonded onto it. To carry out measurements, the ploughmeter is lowered down a borehole so that its tip protrudes into subglacial sediment. Similar to an ice-entrained clast, the immersed section of the ploughmeter is dragged through subglacial sediment. By measuring the bending forces acting on the ploughmeter, we extract information on the mechanical conditions at the ice–bed interface. Hydrological conditions are likely to play a role because high subglacial water pressures weaken sediment and hence affect ploughing. We therefore expect the mechanical properties of the bed material to vary temporally in response to changes in the subglacial water system.

In this chapter, we describe experimental techniques and the analysis of data from two ploughmeters that were installed at the bed of Trapridge Glacier during the 1991 field season. We interpret our ploughmeter observations either in terms of collisions with clasts or as a translational motion through a homogeneous, unlithified sediment layer. Theoretical analysis of the forces on the ploughmeter has yielded *in situ* determination of the effective viscosity of the deforming subglacial material.

2.2 Methods

2.2.1 Description of the device

The ploughmeter (Fig. 2.1a) consists of a 1.54 m long solid steel rod having a diameter of 1.90 cm, onto which two strain gauge networks are mounted. The lower end of the rod terminates in a conical tip. The rod is sheathed in an epoxy-resin-filled, protective, vinyl tube having an inside diameter of 2.54 cm and an outside diameter of 3.18 cm. Eight 20.0 mm long strain gauges (Tokyo Sokki Kenkyujo Co., Ltd, TML, PLS-20-11) are bonded, using a cyanoacrylate-based adhesive, onto a polished section near the rod tip (Fig. 2.2a) and register flexure along two axes. A metal cap covers the conical tip to protect the sandwich construction during insertion. A 10.16 cm long and 0.95 cm diameter guide hole has been drilled along the axis of symmetry into the upper end of

the rod and serves to guide the percussion hammer (Blake and others, 1992) that is used to insert the instrument.
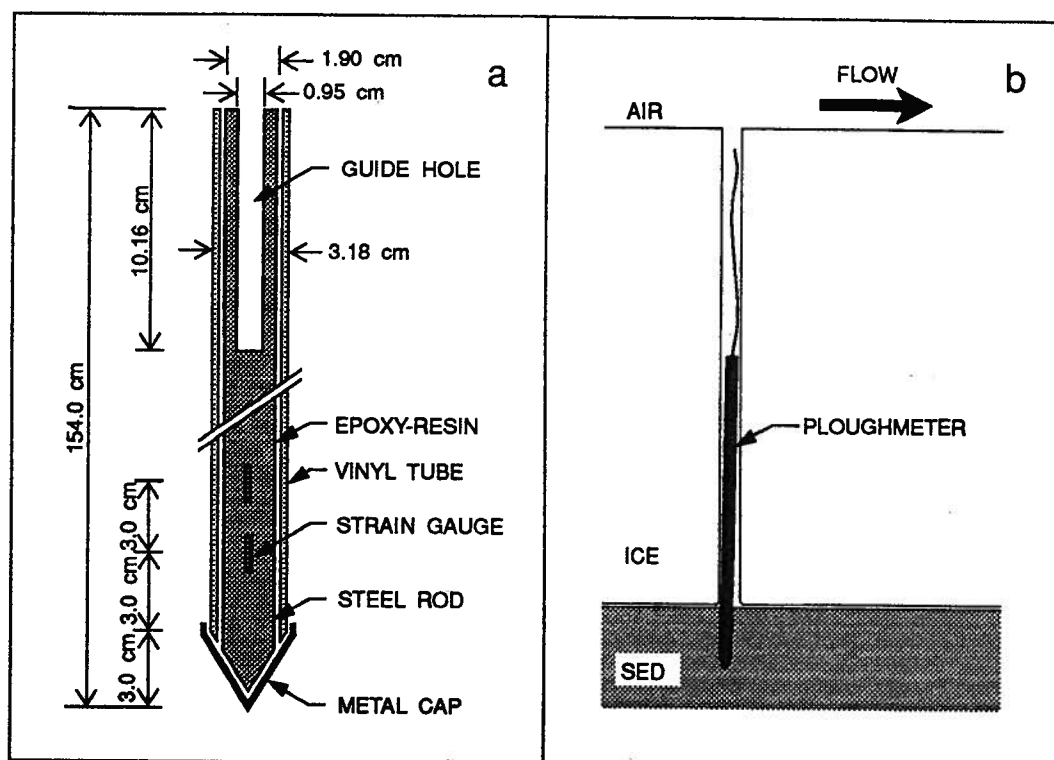
Fig. 2.1: (a) Schematic diagram of the ploughmeter used during the 1991 field season. (b) Diagram of ploughmeter operation (SED indicates sediment).

To install the ploughmeter at the glacier bed, the device is lowered down a borehole (~5 cm diameter) and hammered into subglacial sediment (Fig. 2.1b). The insertion depth must be sufficient to ensure that all eight strain gauges are immersed in subglacial material. The upper section of the ploughmeter extends into the borehole and becomes pinned by the moving glacier.
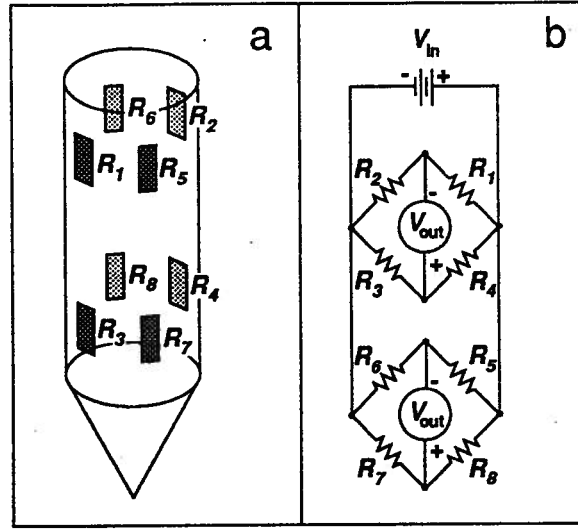
Fig. 2.2: (a) Arrangement of the eight strain gauges near the tip of the steel rod. The two strain gauge networks register flexure along two perpendicular axes. (b) Connection of the eight strain gauges in two full Wheatstone bridge circuits.

2.2.2 Theory of the device

In the following analysis, the ploughmeter is assumed to be subjected to pure bending. Effects of any internal shear force are ignored and flexure stresses are associated only with the internal bending moment. This assumption is safe because beam length is large compared to beam diameter and thus the deformation effect of the shear force is relatively small (Byars and others, 1983, p. 272). For elastic bending of a beam, Hooke's law states that the bending strain ϵ, defined as the fractional change in length ℓ of the strained material, is equal to the bending stress σ divided by Young's modulus E,

$$\epsilon = \frac{\Delta \ell}{\ell} = \frac{\sigma}{E} \tag{2.1}$$

The bending stress σ equals the bending moment M divided by the sectional modulus I/u, a property of the cross-sectional configuration of the beam. This relation is known as the elastic flexure equation (Byars and others, 1983, p. 305) and has the form

$$\sigma = \frac{Mu}{I} \tag{2.2}$$

where I represents the second moment of cross-sectional area about the horizontal centroidal axis of the beam, and u is the distance from the neutral surface (Fig. 2.3). On the neutral surface, fibers comprising the beam undergo no elongation or contraction when the beam is bent; if the beam has a symmetrical cross section, this surface passes through the horizontal centroidal axis. Combining Equations (2.1) and (2.2) yields an expression for the bending strain ϵ in terms of the bending moment M,

$$\epsilon = \frac{Mu}{EI} \tag{2.3}$$

The sign convention is such that strain is tensile for a positive value of u (above the neutral surface) and compressive for a negative value of u (below the neutral surface).
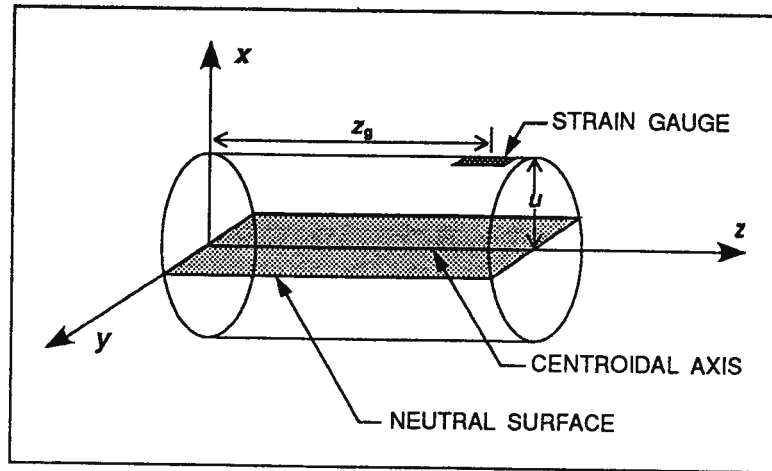
Fig. 2.3: Section of ploughmeter showing geometrical parameters (see text for details).

Eight strain gauges (Fig. 2.2a) are connected as two full Wheatstone bridges (Fig. 2.2b). For each bridge circuit in the unstrained condition, the relationship between input voltage V_{in} and output voltage V_{out} takes the form (Murray and Miller, 1992, p. 158),

$$\left(\frac{V_{out}}{V_{in}}\right)_{unstrained} = \left[\frac{R_3}{R_3 + R_4} - \frac{R_2}{R_1 + R_2}\right] \tag{2.4}$$

where R_1, R_2, R_3 and R_4 are the unstrained values of strain gauge resistance. Defining the change in resistance caused by strain as ΔR, the strained value of gauge resistance is $R + \Delta R$. Thus, for the strained condition, Equation (2.4) becomes

$$\left(\frac{V_{out}}{V_{in}}\right)_{strained} = \left[\frac{R_3 + \Delta R_3}{R_3 + \Delta R_3 + R_4 + \Delta R_4} - \frac{R_2 + \Delta R_2}{R_1 + \Delta R_1 + R_2 + \Delta R_2}\right] \tag{2.5}$$

The strain ϵ is related to the change in gauge resistance ΔR by

$$\epsilon = \frac{\Delta R}{R G_f} \tag{2.6}$$

where the constant of proportionality G_f is the gauge factor.

Combining Equations (2.3) and (2.6) yields

$$\Delta R = \frac{M u G_f R}{EI} \tag{2.7}$$

The product of Young's modulus E and the second moment of area I is known as the bending modulus and is a measure of the stiffness of the beam (Byars and others, 1983, p. 306). For the ploughmeter, the bending modulus is the sum of the individual bending moduli for the three materials involved (steel, epoxy-resin and vinyl). Equation (2.7) relates the change in gauge resistance ΔR to the bending moment M and stiffness of the ploughmeter. The bending moment can vary with distance from the ploughmeter tip, so Equation (2.7) is position-dependent. Substitution of Equation (2.7) into Equation (2.5) allows calculation of the output voltages of the bridge circuits if the loading on the ploughmeter is known.

2.2.3 Calibration

Prior to insertion, the ploughmeter is calibrated by clamping it horizontally near the guide hole and at an intermediate point that serves as a fulcrum. Loads are then applied to the free end by hanging weights from the tip (Fig. 2.4a). Care must be taken to ensure that all eight strain gauges lie between the load at the tip and the fulcrum. This configuration is equivalent to a beam that is subject to a bending stress created by supports at both ends and having a load in-between (Fig. 2.4b). The ploughmeter is calibrated using weights ranging between 1 and 30 kg that correspond to applying a load ranging from 10 to 300 N. For each load, the ploughmeter is rotated about its long axis to obtain a calibration for all possible orientations of the device with respect to the direction of glacier flow. Output voltages from each bridge circuit are fitted for each load, using least squares, to functions of the form

$$V(L_i, \phi) = A_i \, \cos(\phi + B_i) + C_i \qquad (2.8)$$

where L_i are the various loads applied during the calibration, A_i are the fitted signal amplitudes at those loads, B_i are the azimuth offsets for each load, C_i are voltage offsets, ϕ represents the azimuth of the load with respect to the local coordinate system of the ploughmeter and V is the predicted voltage output. Two sets of functions of the form of Equation (2.8) are associated with every ploughmeter—one for each of the two bridge circuits. In a perfect device, the circuit pair would have values of B differing by exactly 90° for a given load. In practice, the orientations of the two groups of strain gauges are not exactly perpendicular and values of B are not orthogonal.
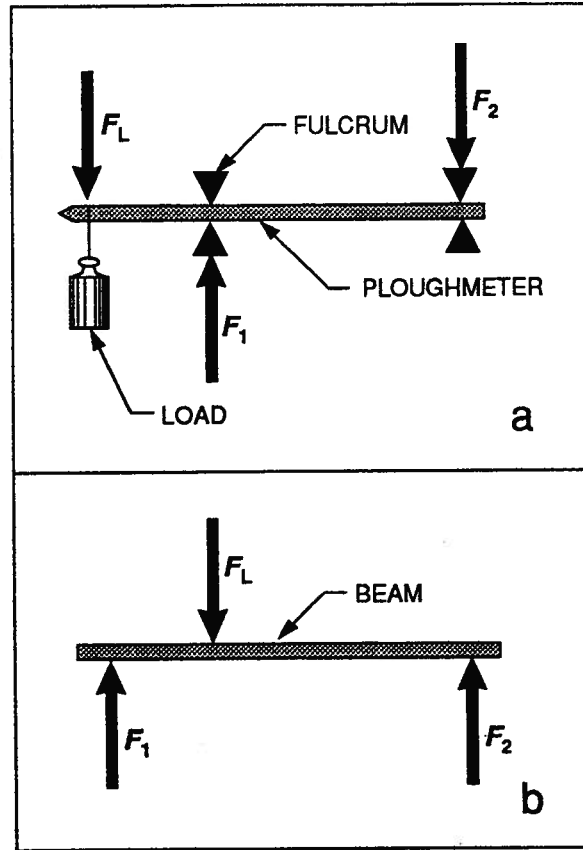
Fig. 2.4: (a) Schematic diagram of ploughmeter forcing in the calibration configuration. (b) Forces on a point-loaded beam which is supported at both ends. With appropriate choices of F_L, F_1 and F_2 the bending in (a) and (b) is identical.

The "three-point" load model (Fig. 2.4b) applies to a ploughmeter installed beneath a glacier, if the ploughmeter is elastically bent by a force concentrated near the tip (the glacier bed) and a force part way up the device (the base of the ice) while the upper part of the ploughmeter is held fixed in the ice. This picture is only appropriate if forces are assumed to be small except at these three pinning points. For this case, the field data can be analyzed by computing values of L and ϕ from Equation (2.8)

using a simplex algorithm (Press and others, 1992, p. 402) that minimizes the difference between predicted and observed output voltages. A linear regression extrapolates values of A, B, and C for loads beyond the calibration range.

If, in Equation (2.7), we set u equal to the radius of the steel rod, while preserving the sign convention of Equation (2.3), and take $M(z_g) = L_i z_g$ then Equation (2.5) can be fitted to the calibration data set. Here, L_i are the loads used during the calibration and z_g is the distance between the point where the load is applied and the position of the strain gauge (Fig. 2.3). In this way, we obtain values of Young's moduli for steel, epoxy-resin and vinyl for individual ploughmeters, as well as precise resistance values R for the eight strain gauges.

For a ploughmeter installed at the glacier bed, the subglacial geometry is likely to differ substantially from that of the "three-point" calibration (Fig. 2.4), but the calibration remains valid. Bending forces acting on the ploughmeter are in general not concentrated near the tip but are distributed along the entire section of the ploughmeter that is immersed in subglacial sediment. We consider these distributed forces in the "Interpretation" section (below). Secondly, at the fulcrum point near the ice–bed interface, pressure melting of the borehole wall might expand the area of contact between the ice and the ploughmeter. As a result, the fulcrum load could become distributed over several centimetres. However, the bending moment $M(z_g)$ at the position z_g of any of the eight strain gauges is not affected as long as the strain gauge is fully immersed in subglacial material and is not located in the region of the distributed fulcrum load. Thirdly, once the ploughmeter is firmly jammed at the base of the borehole, the long axis of the ploughmeter will not necessarily be normal to the applied load at the tip. In our study, any effects of non-normality are likely to be small. Near-verticality of boreholes is confirmed by inclinometry. Ploughmeter length greatly exceeds hole diameter, so within each hole a ploughmeter is closely aligned with the hole axis.

2.3 Field observations

In July 1991, two ploughmeters were inserted into sediment beneath Trapridge Glacier near the centre-line flow markers and approximately 600 m up-flow from the bulge (Fig. 1.1). The insertion sites lie on a single flow line and are approximately 10 m apart. Both boreholes were unconnected to the subglacial drainage system at the time that ploughmeters were installed. The exact insertion depth of the ploughmeters into subglacial sediment is uncertain. Hydraulic excavation by the hot water drill is believed to loosen subglacial material to a depth of several decimetres below the ice–bed interface (Blake and others, 1992). It is likely that a ploughmeter, once lowered to the bottom of the borehole, settles into this disturbed layer simply by its own weight. The measured insertion depth (14 cm for 91PL01 and 8 cm for 91PL02) therefore represents the added penetration that results from the hammering procedure. The thickness of the disturbed layer is estimated as 15–25 cm (Blake and others, 1992), so the insertion depth for the ploughmeters could range from 10–40 cm. During the course of our measurements, the surface velocity of Trapridge Glacier was about 100 mm d^{-1}. Observations of the deformation of boreholes reveal that for this glacier no more than 10 mm d^{-1} of the surface velocity can be accounted for by internal ice creep (Blake, 1992). The remaining 90 mm d^{-1} result from some combination of glacier sliding and sediment deformation that depends on the degree of subglacial ice–sediment coupling.

Figures 2.5 and 2.6 show 13 days of observations for ploughmeters 91PL01 and 91PL02. The data are presented in calibrated, though otherwise raw, form. An obvious feature in the force records for both ploughmeters is a gradual rise during the initial 3–5 days of observation. A diurnal signal is superimposed on the gradually rising force recorded by ploughmeter 91PL01 during the initial three days (Fig. 2.5b). Strong diurnal fluctuations in subglacial water pressure are simultaneously observed in a borehole located approximately 1 m from ploughmeter 91PL01 (Fig. 2.5a). At the same time, the azimuth record (Fig. 2.5c) indicates an apparent rotation of the ploughmeter about
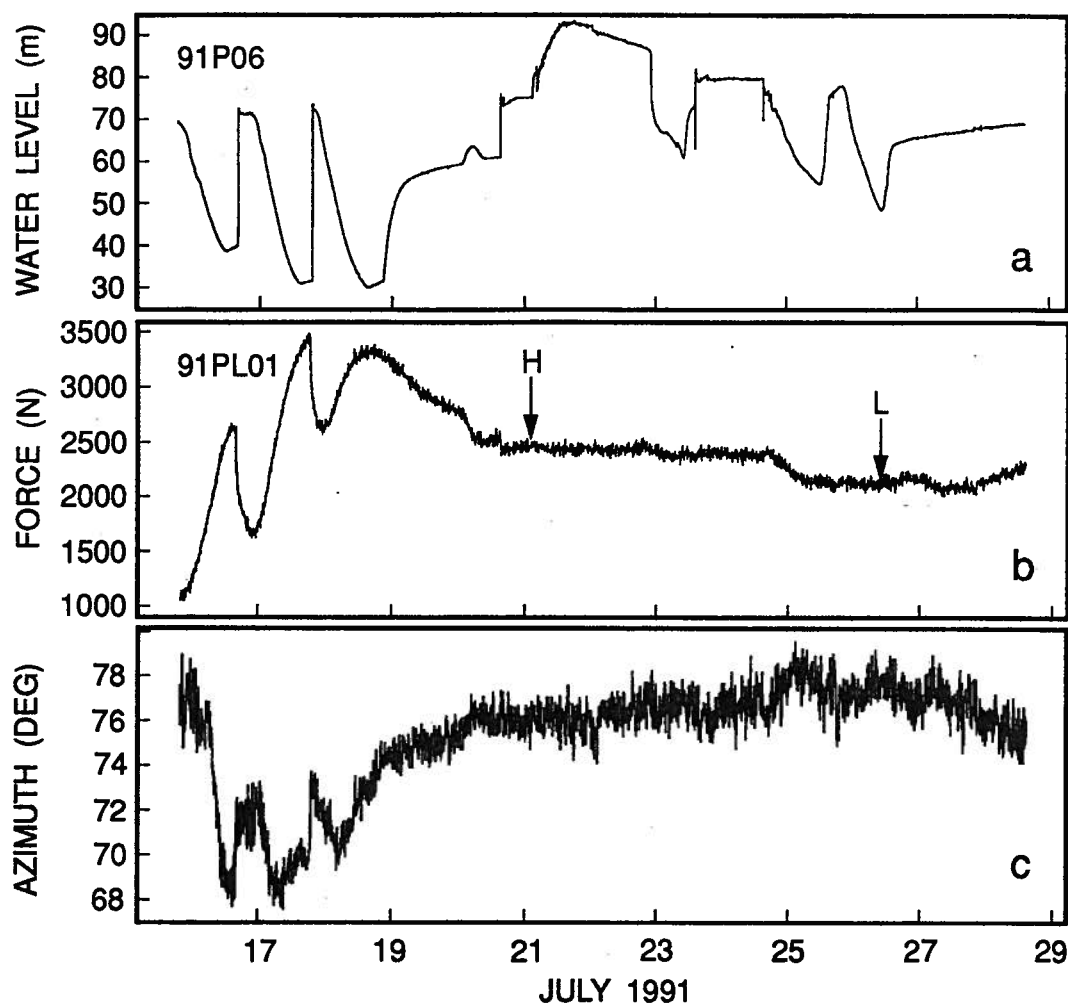
Fig. 2.5: Data from pressure sensor 91P06 and ploughmeter 91PL01. (a) Subglacial water pressure record. Note the diurnal signal during the initial three days. Super-flotation pressures correspond to a water level of more than about 63 m. (b) Force record indicating load applied to the tip of the ploughmeter. The arrows show the two data points that correspond to the highest (H) and lowest (L) loading during the observation period (see text for details). (c) Azimuth of the load with respect to the internal coordinates of the ploughmeter.

its long axis by up to 9°. After the initial phase, the data of ploughmeter 91PL01 display a comparatively smooth character with near-zero ploughmeter rotation. Results obtained from ploughmeter 91PL02 show a completely different character. During

the entire observation period, the force record (Fig. 2.6a) displays a sawtooth appearance, whereas the azimuth record (Fig. 2.6b) indicates that the ploughmeter appears to undergo a 25° back-and-forth rotation about its long axis.
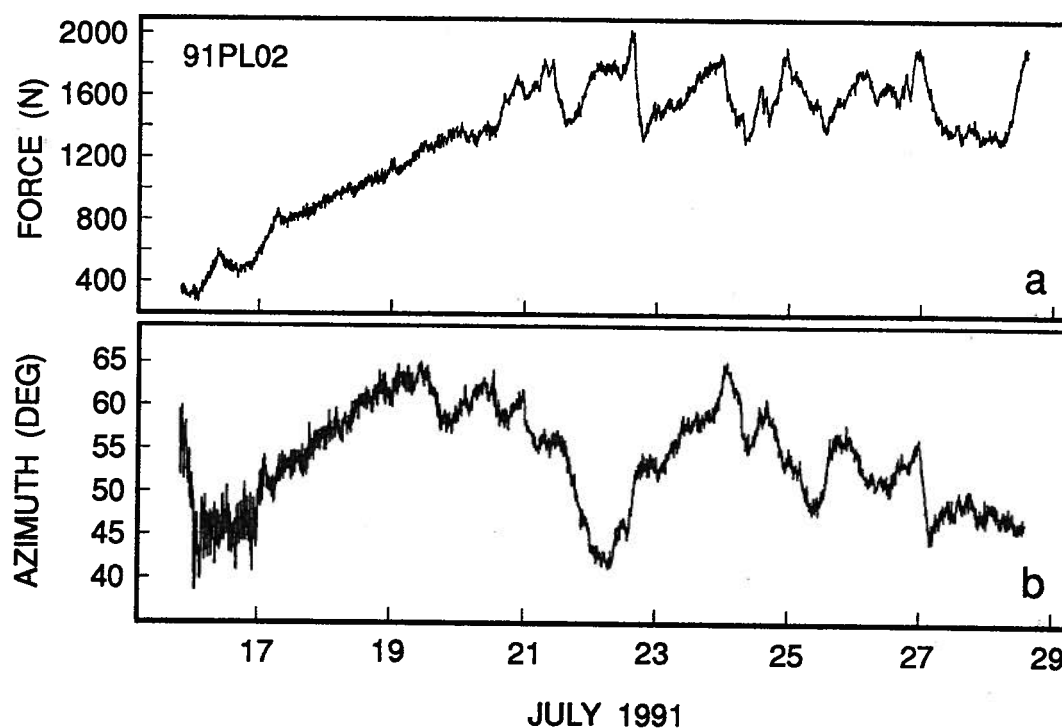
Fig. 2.6: Data from ploughmeter 91PL02. (a) Force record indicating load applied to the tip of the ploughmeter. (b) Azimuth of the load with respect to the internal coordinates of the ploughmeter.

If we assume that the principal direction of ploughmeter motion is down-flow, we can decompose the net force values into down-flow and cross-flow components. The azimuthal angle of the ploughmeter relative to the glacier flow direction is a key element in this decomposition process; any disturbance on the azimuth record indicates non-zero cross-flow motion. To effect down-flow/cross-flow decomposition, we align the average azimuth to the glacier flow direction. There could well be partitioning between rotation of the ploughmeter about its long axis and cross-flow motion but this uncertainty does

not have serious consequences. Any fraction of cross-flow motion that is assigned to ploughmeter rotation reduces the cross-flow force component by that fraction, and the down-flow component will increase slightly to achieve the correct net force. However, since the partitioning has only a minor effect on the down-flow component (Fig. 2.7), we constrain the down-flow/cross-flow decomposition by prohibiting rotation of the ploughmeter about its long axis. Decomposition of the data of ploughmeter 91PL02 shows that there is no apparent correlation between the records of down-flow and cross-flow force components (Fig. 2.7). Intervals over which a positive correlation seems to prevail are followed by intervals where the correlation seems to be negative or non-existent.

2.4 Interpretation

For three to five days after installation, the ploughmeters are believed to be interacting with subglacial material that has been loosened by hydraulic excavation during hot water drilling (Blake and others, 1992). Support for this speculation can be seen in the gradual rise of the force records of both ploughmeters. It is reasonable that this rise occurs because the ploughmeters are transported from initially loosened and disturbed material to undisturbed bed material. The smooth character of the data of ploughmeter 91PL01 might indicate that the ploughmeter was inserted into an area of the glacier bed that consists of mainly fine-grained material, but we cannot confirm this conjecture. On the other hand, the sawtooth appearance of the force record for 91PL02 suggests that the ploughmeter is interacting with a clast-rich area of the glacier bed. This explanation is supported by the fact that inserting ploughmeter 91PL02 was notably more difficult than for 91PL01, suggesting that clasts in the sediment hampered the insertion process.

A relationship between water pressure and ploughmeter–sediment interaction is not surprising, but we have no complete explanation for the data of ploughmeter 91PL01.
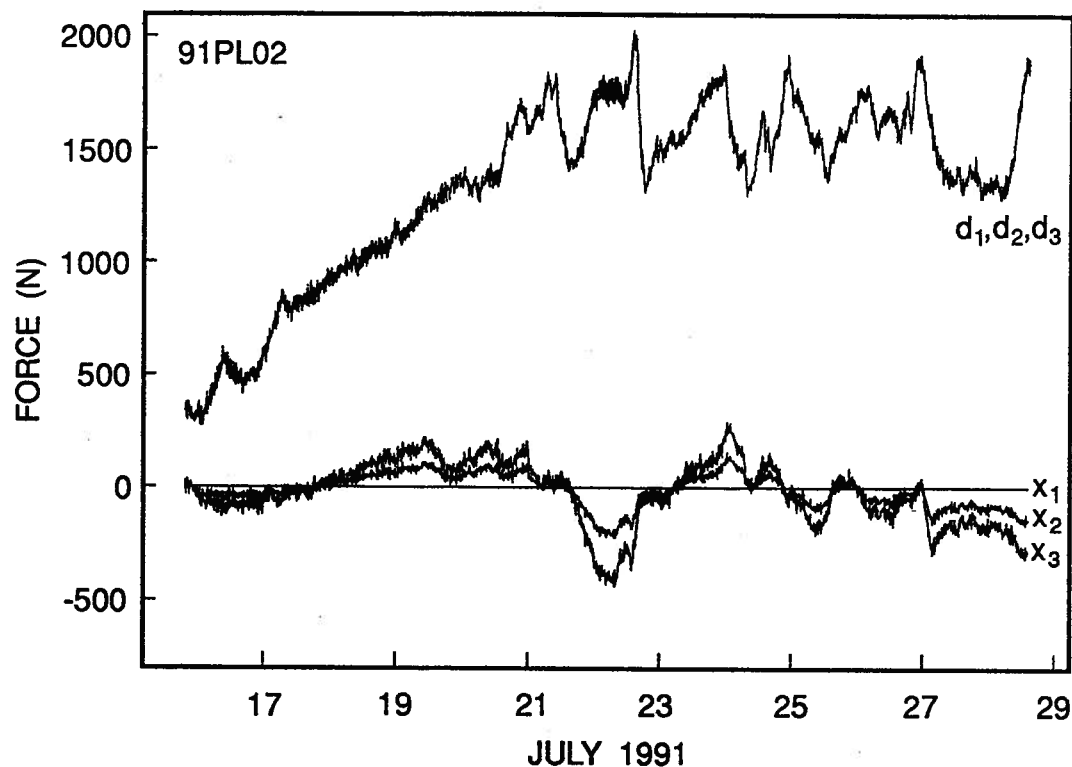
Fig. 2.7: Down-flow/cross-flow decomposition of the data from plough-meter 91PL02 showing the effect of partitioning between ploughmeter rotation and cross-flow motion. Note that the partitioning has only a minor effect on the down-flow component (traces d_1, d_2, and d_3 are indistinguishable) and that cross-flow traces x_2 and x_3 differ in amplitude but have closely similar form. Trace x_1 represents 100% ploughmeter rotation. Trace x_2 represents 50% ploughmeter rotation and 50% cross-flow motion. Trace x_3 represents 100% cross-flow motion.

Vertical uplift of the glacier as a result of super-flotation water pressures could explain the reduced forcing on the ploughmeter, if the ploughmeter was lifted out of the sediment. However, when pressure drops, the forcing increases, suggesting that re-insertion has occured. Re-insertion would be difficult to explain unless the ploughmeter is firmly wedged in the hole.

Alternatively, softening of the subglacial material during intervals of high water pressure could account for a reduced forcing. However, a near-instantaneous response

of the ploughmeter requires rapid penetration of excess water pressure into subglacial sediment. The low pressure diffusivity of typical subglacial sediment makes a fast response unlikely.

Finally, in areas where the bed is hydraulically isolated, vertical uplift of the glacier due to an increase in subglacial water pressure should be accompanied by an essentially simultaneous decrease in the contact pressure of the ice onto the sediment. This reduction in ice-contact pressure would decrease the effective pressure in the sediment and, hence, weaken it. The apparent rotation of ploughmeter 91PL01 during periods of increased forcing might result from minor irregularities in ploughmeter geometry that could cause twisting or from pressure-induced cross-flow components of sediment deformation.

The completely different character of the ploughmeter responses inspires contrasting approaches to further analysis. Our first approach is qualitative and emphasizes the heterogeneity of subglacial sediment; the second is quantitative and emphasizes localized homogeneity. To explain the results for ploughmeter 91PL02 we shall introduce a simple model that represents collisions with clasts. To interpret the results for ploughmeter 91PL01, we shall consider the ploughmeter to be dragged through a layer of homogeneous, unlithified sediment.

2.4.1 Qualitative model

In an attempt to simulate collisions between individual clasts and a ploughmeter as it is dragged through sediment, we developed a simple numerical model to describe a synthetic till created by randomly filling a volume with spheres of different sizes (Fig. 2.8). The spheres represent clasts in a matrix of fine-grained solids and water-filled voids. We assumed a porosity of 0.3 and a clast size distribution that is based on the analysis of grain sizes of basal till from Trapridge Glacier (Clarke, 1987). Only clasts of the five largest size classes were used, corresponding to spheres of diameters

8–32 mm. Grains of smaller size were assumed to form the matrix of fines. Higher porosities would be justified if the sediment was fully dilated and constantly deforming. These conditions were inferred for Ice Stream B (Blankenship and others, 1986, 1987), but are not believed to be the case for Trapridge Glacier. However, it is interesting to note that any changes in the assumptions of porosity and size distribution do not alter the underlying idea of this simple model and have no direct influence on the qualitative nature of our conclusions.

The transverse motion of a vertical line through the volume represents the plough-meter being dragged through subglacial material. Force records are synthetically generated by considering how the path of the vertical line indenter intersects spheres of the model till. In our analysis, we view the spheres as being attached to springs so that they are constrained to move only in a direction that is perpendicular to the motion of the vertical line. The line indenter pushes the spheres to the side as it moves through the volume and experiences a force which is proportional to the sideways displacement of the spheres. Depending on whether the point of collision is to the right or left of the centre of a sphere (Fig. 2.9a), a negative or positive cross-flow component of the force is calculated, (Fig. 2.9b, lower trace). For the case where the line indenter collides with two or more spheres, the cross-flow force components calculated for individual spheres add if the centres of all spheres are on the same side of the path of the line indenter. On the other hand, for spheres with centres located on opposite sides of the path, individual cross-flow effects will cancel out. To obtain the down-flow component of the force record (Fig. 2.9b, upper trace) we sum the absolute values of cross-flow force contributions from individual spheres. The calculation of the force record in this way does not include any real physics of how forces are exerted onto a ploughmeter as it collides with clasts. This simple geometrical analysis is sufficient, because we are attempting to explain the character, but not the magnitudes, of the force component

records. Comparison of Figures 2.7 and 2.10 show that the records generated using this simple model display many of the features seen in the real data.
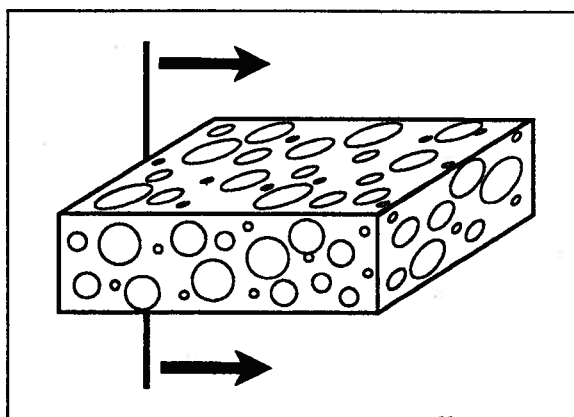
Fig. 2.8: Schematic diagram of the model till. The vertical line represents the ploughmeter moving through subglacial sediment.
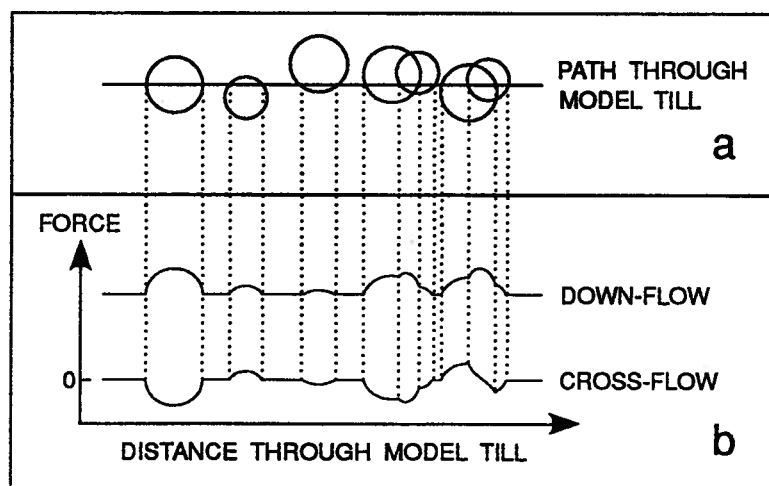
Fig. 2.9: Illustration of how records of down-flow and cross-flow force components are synthetically generated. (a) Plan view of a simple model till consisting of seven spheres. (b) Synthetically generated records of down-flow (upper trace) and cross-flow (lower trace) force components for the model till shown in (a).

Even though it is probable that other descriptions of ploughmeter–till interaction could lead to similar results, we feel that the above is a simple model that explains the available data. Our model also includes reasonable constraints on the nature of the till. Futhermore, it suggests directions for future effort: if till texture is assumed to be spatially homogeneous, then the "collision frequency", indicated by a ploughmeter, is proportional to sliding rate; on the other hand, if the sliding rate is constant, then temporal variation in the collision frequency reflects spatial variations in subglacial sediment texture.
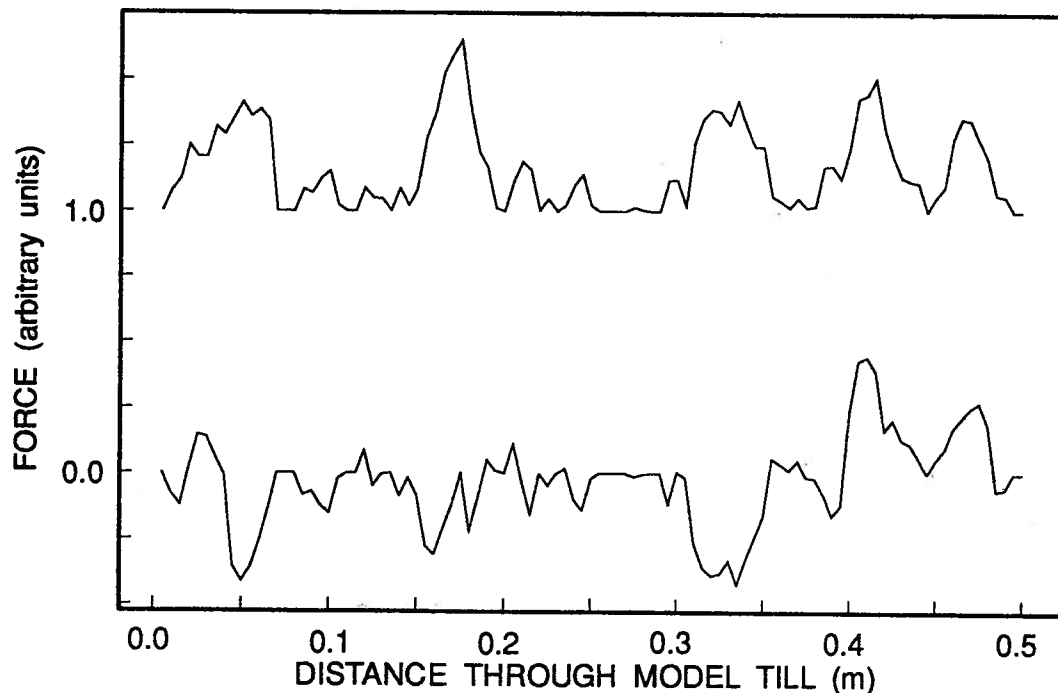
Fig. 2.10: Synthetically generated records of down-flow (upper trace) and cross-flow (lower trace) force components. Note the similar character to that of Figure 2.7.

2.4.2 Quantitative model

For the case where the ploughmeter is dragged through a homogeneous sediment layer, the ploughmeter experiences a distributed force rather than a force concentrated near its tip. We attempt to extract information on the strength of the subglacial material by estimating how forces are distributed along the ploughmeter. However, the lack of a complete rheological description of subglacial sediment makes it difficult to calculate the force distribution on the immersed section of a ploughmeter. We therefore require a rheological model of the bed material that can provide this information. Till has been modelled as a visco-plastic material (Boulton and Hindmarsh, 1987; Alley, 1989) that is taken to have a yield strength below which no deformation occurs and above which it behaves as a viscous fluid. In our study, we separately treat the subglacial sediment as a layer of Newtonian viscous fluid and as an ideal plastic solid.

2.4.2.1 Viscosity estimate

To calculate the force distribution along the section of a ploughmeter that is immersed in sediment, we apply standard hydrodynamic theory to investigate viscous fluid motion around a finite moving cylinder. In this case, sediment is viewed as a Newtonian fluid having viscosity μ and the ploughmeter is represented by a cylinder experiencing Stokes flow. Exact solutions for flow around finite cylinders undergoing uniform translation through a viscous fluid are unavailable but, by approximating cylinders as ellipsoids, standard solutions can be employed (Happel and Brenner, 1973, p. 227).

Under conditions where fluid inertia is negligible, the force distribution along an elongated body can be obtained as an asymptotic expansion involving the ratio of cross-sectional radius to body length (Batchelor, 1970; Cox, 1970; Tillet, 1970). For a body of length $2c$ and cross-sectional radius a that is aligned with the z axis and

moving in the x direction, the force per unit length on the body can be expressed as (see Appendix A for details)

$$F(z) = \mu v L(z; a, c) \qquad (2.9)$$

where

$$L(z; a, c) = \frac{4\pi}{\ln(2c/a)} \left\{ \frac{2\ln(2c/a) - \frac{1}{2}\ln\left[\frac{a}{a(z)}\left(1 - \frac{z^2}{c^2}\right)^{1/2}\right]}{2\ln(2c/a) + 1} \right\} \qquad (2.10)$$

is a characteristic length scale that incorporates the shape and dimensions of the body. In effect, the force per unit length on the body is linearly proportional to the effective fluid viscosity μ, the translational velocity v, and the geometry of the body. Furthermore, the force distribution as given by Equation (2.9) is symmetrical about $z = 0$. If we assume a sharp ice–bed interface, we can regard it as a symmetry plane. With the origin taken to lie on this plane, we need only consider the negative half of the elongated body ($-c \leq z \leq 0$), which represents the section of ploughmeter immersed in subglacial sediment.

In the case of a deforming sediment layer, shear strain rate is assumed constant with depth. Accordingly, the down-flow velocity of sediment decreases linearly with distance from the ice–bed interface and the differential velocity between ploughmeter and surrounding sediment increases with depth. For this case, where the ploughmeter is moving through an already shearing sediment layer, the velocity v in Equation (2.9) represents the differential velocity between the ploughmeter and the sediment and becomes a function of z. The thickness of the deformable sediment layer underneath Trapridge Glacier is assumed to be 0.5 m (Blake and Clarke, 1989).

To calculate the force distribution along the section of a ploughmeter immersed in subglacial sediment (Equation (2.9)), we approximate the shape of the ploughmeter as

either an ellipsoid (Equation (A.9)) or a cylinder (Equation (A.12)). While the ellipsoid assumption likely underestimates the forces in the lower section of the ploughmeter, end effects at the flat faces of the cylinder greatly overestimate the forces near the conical tip. We expect that the true result lies somewhere between that yielded by the ellipsoidal and cylindrical approximations, and regard the ellipsoid as a better overall representation of the ploughmeter.

Once the force distribution on the immersed section of the ploughmeter is known, the bending moment $M(z_g)$ at the position z_g of a strain gauge can easily be calculated according to

$$M(z_g) = \int_{-c}^{z_g} F(z)(z_g - z)\,dz \qquad (2.11a)$$

$$= \mu \int_{-c}^{z_g} v(z)L(z; a, c)(z_g - z)\,dz \qquad (2.11b)$$

Here, z_g is a negative value, since the strain gauge is located below the ice–bed interface, and c corresponds to the depth to which the ploughmeter is immersed in sediment. It is assumed that the viscosity μ is constant with depth in the sediment. Equation (2.11) is substituted into Equation (2.7) for all eight strain gauges of a ploughmeter. An estimate of μ can be obtained by minimizing (Press and others, 1992, p. 402) the objective function

$$f(\mu) = \sum_{i=1}^{2} \left[\left(\frac{V_{out}}{V_{in}} \right)_{observed,i} - \left(\frac{V_{out}}{V_{in}} \right)_{predicted,i} \right]^2 \qquad (2.12)$$

The sum in Equation (2.12) is taken over the two bridge circuits. The data set of ploughmeter 91PL01 supplies the observed voltage ratios and the predicted voltage ratios are calculated using Equation (2.5).

By this method, the apparent viscosity of subglacial sediment has been calculated as a function of ploughmeter insertion depth for three different styles of basal motion (Fig. 2.11). Figures 2.11a and 2.11b represent the two end-member cases of 100% glacier

sliding and 100% bed deformation assuming that the sediment velocity varies linearly with depth. In Figure 2.11c, we assume that 50% of the $90\,\mathrm{mm\,d^{-1}}$ basal velocity is due to glacier sliding and 50% is due to bed deformation. Using the record of ploughmeter 91PL01, the calculations were carried out for two data points that correspond to the highest and lowest loading during the observation period (see arrows labelled H and L in Fig. 2.5b). We have not included the initial five days of the record, because we believe these represent a start-up phase that does not characterize ploughmeter interaction with an undisturbed subglacial bed.

Results are shown for both ellipsoidal and cylindrical shapes. We note that the apparent viscosity calculated for the ellipsoid is greater than that for the cylinder, because forces near the end of a cylinder exceed those near the tip of an ellipsoid. The increase in calculated viscosity as a function of insertion depth that we note in Figure 2.11a is a consequence of the assumed ellipsoidal geometry of the ploughmeter. Within the uncertainties and assumptions listed above, we can limit the viscosity estimate to a spread of one order of magnitude. The 100% deformation model yields an upper bound on apparent viscosity in the range 5.6×10^9 to $3.1 \times 10^{10}\,\mathrm{Pa\,s}$; the 100% sliding model yields a lower bound of 3.0×10^9–$6.6 \times 10^9\,\mathrm{Pa\,s}$. These estimates of Trapridge sediment viscosity are consistent with those of Blake (1992) and Blake and Clarke (1989).

2.4.2.2 Yield strength estimate

Following the analysis by Humphrey and others (1993) we can estimate the plastic yield strength of subglacial material by considering plastic flow around a stiff cylinder. We approximate the cylinder by a flat and long rigid indenter of width equal to the diameter of the ploughmeter. If we define the problem in plane strain, thereby ignoring
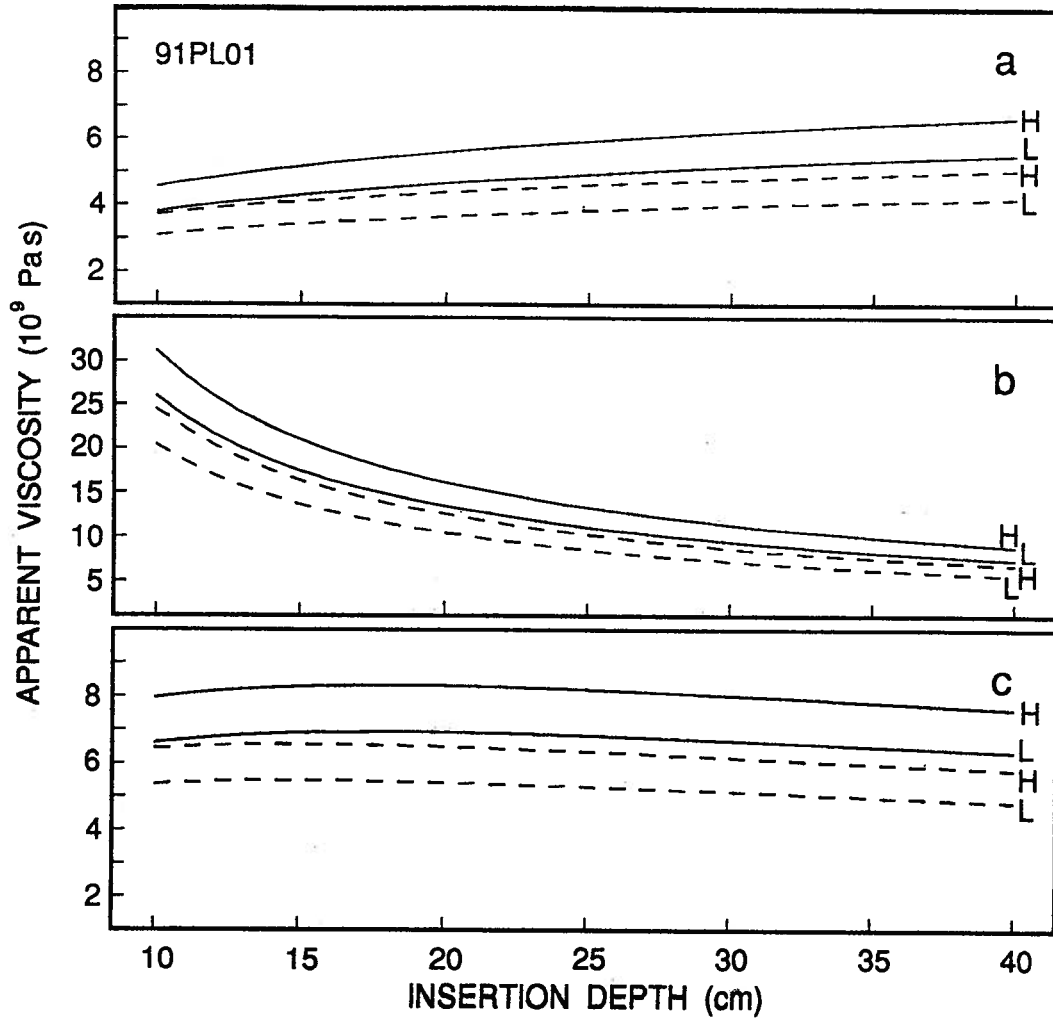
Fig. 2.11: Apparent viscosity of subglacial sediment as a function of insertion depth of ploughmeter 91PL01 for three different styles of basal motion. Solid lines indicate ellipsoidal approximation. Dashed lines indicate cylindrical approximation. Highest and lowest loading (see Fig. 2.5b) is denoted by H and L, respectively. (a) 100% glacier sliding. (b) 100% sediment deformation in a 0.5 m thick layer. (c) 50% glacier sliding and 50% bed deformation. A linear velocity–depth profile was assumed for the deforming sediment.

end effects, the stress that the indenter exerts on the semi-infinite plastic body onto which it is pressed, is uniformly distributed and can be expressed as (Hill, 1971, p. 340)

$$\sigma = (2 + \pi)k_P \tag{2.13}$$

where k_P is the plastic yield strength of the material. To close the wake left by a positive indenter, Humphrey and others (1993) introduced a negative indenter of equal strength and obtained the expression

$$F = 4a(2 + \pi)k_P \tag{2.14}$$

where a is the radius of the ploughmeter. If Equation (2.14) describes the dragging of the ploughmeter through subglacial sediment, then F denotes the constant force per unit length acting on the immersed section of the ploughmeter.

With this constant force distribution, the bending moment $M(z_g)$ can be calculated as

$$M(z_g) = F \int_{-c}^{z_g} (z_g - z)\,\mathrm{d}z \tag{2.15a}$$

$$= 4a(2 + \pi)k_P \int_{-c}^{z_g} (z_g - z)\,\mathrm{d}z \tag{2.15b}$$

where z_g denotes the position of the strain gauge. The development is closely analogous to that of the previous section and proceeds by substituting Equation (2.15) into Equation (2.7) for all eight strain gauges of a ploughmeter. Again, an expression similar to Equation (2.12) is minimized, analyzing the same two data points that were used to obtain a viscosity estimate, to calculate an estimate of k_P. The plastic yield strength obtained by this method is 48–57 kPa.

2.5 Concluding discussion

Our analysis of the strength of subglacial material includes a number of assumptions. These are listed and briefly discussed as follows:

1. Solutions for creeping motion of a viscous fluid around solid bodies are based on the assumption that the bodies are immersed in a homogeneous and incompressible Newtonian fluid. In effect, the deforming bed is treated as a continuum that

has no internal structure and it is assumed that a no-slip boundary exists at the ploughmeter surface. Thus clast-scale interaction processes are neglected.

2. The results of the slender-body theory (see Appendix A) are only applicable for long bodies possessing large length-to-diameter ratios c/a. To get some sense of the error introduced by applying slender-body theory to short objects, we compared the drag calculated using Oberbeck's formula(Equation (A.3)) to the slender-body result (Equation (A.11)). For $c/a = 6.3$ (corresponds to an insertion depth of the ploughmeter of $c = 10\,cm$) the discrepancy is about 0.19% which reduces to about 0.009% for $c/a = 25$ (corresponds to $c = 40\,cm$).

3. Motion of the ploughmeter through ice has been completely neglected. This assumption is probably safe since the protective vinyl tube coating the ploughmeter also acts as a thermal insulator and suppresses the regelation mechanism.

4. Hydrological and mechanical perturbations of the subglacial environment, caused by the presence of a water-filled borehole, have been neglected.

The rheology of subglacial material is doubtless more complex than our simple model rheologies and should probably incorporate pore water pressure, deformation history, and heterogeneity of the material. Nevertheless, the simple models give us some indication of the ability of subglacial material to resist deformation. Estimates of plastic yield strength and effective viscosity derived in this study can be compared to the applied shear stress beneath Trapridge Glacier. Assuming a plane slab geometry, the mean basal shear stress beneath our study site is $77\,kPa$ (based on an ice thickness of $72\,m$ (Blake, 1992)). If subglacial sediment were plastic, then the inferred yield strength is about 70% of the applied shear stress. On the other hand, for the case of Newtonian viscous behaviour, the basal strain rate can be calculated to be about $33\,year^{-1}$. Here, glacier sliding is neglected and the entire basal motion of $90\,mm\,d^{-1}$ is assumed to result from uniform shear deformation in a $0.5\,m$ thick sediment layer. If the deforming layer was Newtonian viscous and resisted the basal shear stress of $77\,kPa$,

then the 33 year^{-1} strain rate represents a viscosity of 4×10^{10} Pa s. The viscosity inferred in our study is from as little as 20–25% to as much as an order of magnitude lower. Thus, for the viscous and plastic rheologies, the estimates of sediment strength yielded by the ploughmeter analysis suggest that the deformational resistance of the bed is comparable to, but somewhat less than, that required to ensure mechanical stability in this region of Trapridge Glacier.

Results of previous work on *in situ* measurements of the strength of deforming sediment mostly differ from those obtained in our study. Humphrey and others (1993) obtained estimates of sediment viscosity and plastic yield strength by analyzing the plastic deformation of a drill stem that became stuck in the bed of Columbia Glacier, Alaska. They reported viscosities (2×10^8–5×10^8 Pa s) and yield strengths (5.5–13 kPa), that are as much as one order of magnitude lower than our estimates. At the same time, the basal shear stress beneath Columbia Glacier (100 kPa) is about 30% greater than that calculated for Trapridge Glacier. Results from tests of basal till from beneath Ice Stream B (Kamb, 1991) indicated a plastic-like behaviour and resulted in estimates of the yield strength (1.6–2.0 kPa) that also tend to be softer than those derived here. Ice Stream B has a significantly lower basal shear stress yet higher flow rate (Alley and others, 1987) than Trapridge Glacier, consistent with a weaker subglacial sediment. Viscosities calculated from the results of the work done by Boulton and Hindmarsh (1987) beneath Breidamerkurjökull in Iceland are generally an order of magnitude higher (10^{10}–10^{11} Pa s) than our estimates. The Breidamerkurjökull observations and those on Trapridge may not be directly comparable. The Breidamerkurjökull measurement were carried out in a tunnel penetrating very thin ice near the glacier margin, where mechanical and hydrological conditions might be unrepresentative. (The calculated shear stress was not corrected for longitudinal stresses, large near the glacier terminus, and the observation tunnel would further disturb the stress system.) In contrast, work done by Iverson and others (1994) on Storglaciären, Sweden, yielded results that are

in agreement with those derived in this study. By recording the force generated on a cylinder with conical ends that was dragged through the till, they were able to obtain an estimate of the yield strength ($\sim$60 kPa) which suggests that the subglacial till of Storglaciären supports on average about two thirds of the calculated winter basal shear stress. In summary, the shear strength of deforming sediment is found to vary greatly beneath different glaciers. We are not troubled by this large range in values since natural variations in sediment texture and composition can easily account for different stiffnesses.

In this chapter, we have demonstrated that the ploughmeter is a useful tool for assessing physical properties of subglacial sediment. In Chapter 3 we examine the possibility that ploughmeter measurements can be used to characterize sediment texture.

Chapter 3

FRACTAL DESCRIPTION OF SUBGLACIAL SEDIMENT

"Clouds are not spheres, mountains are not cones, coastlines are not circles, and bark is not smooth, nor does lightning travel in a straight line..."

- Benoit Mandelbrot

3.1 Introduction

Many natural patterns are known to be self-similar, possessing characteristics which appear to be independent of the length scale of observation. For example, it is nearly impossible to determine absolute sizes in a photograph of many geological features without an object determining scale (Turcotte, 1989). Fractal geometry (Mandelbrot, 1983) incorporates this idea of self-similar scaling and extends the notion of integer spatial dimension, associated with simple geometric structures, to become a parameter characterizing zigzag, rough, and heterogeneous structures of real media. Thus, fractals provide a framework for both the description and mathematical modelling of the irregular and seemingly complex patterns found in nature.

Fractal mathematics and fractal scaling have been applied to a wide range of natural processes (Feder, 1988). Applications have ranged from physically realistic descriptions of topographic relief (Turcotte, 1987; Gilbert, 1989), soil fabric (Moore and Krepfl, 1991) and aquifer permeability (Ross, 1986; Turcotte, 1989) to studies of solid-pore interfaces in porous media (Katz and Thompson, 1985; Thompson and others, 1987; Krohn, 1988a, 1988b; Krohn and Thompson, 1986) and estimation of soil water retention properties (Tyler and Wheatcraft, 1989, 1990). Of special interest to this study is the work by Hartmann (1969), Tyler and Wheatcraft (1989) and Hooke and

36

Iverson (1995) who reported fractal scaling behaviour in the particle-size distributions of a variety of soils and fragmented rocks.

In this chapter, we first give a brief review of the fundamentals of fractal geometry and introduce the necessary notation. Then, we subject results from ploughmeter measurements in the field and from our numerical ploughmeter model to fractal analysis and obtain an estimate of the basal glacier sliding rate. In closing this chapter, we employ simple fractal models to establish a relationship between ploughmeter response and the particle-size distribution of the subglacial material.

3.2 Fractal mathematics

The basic premise upon which fractal concepts are based is the notion of self-similarity. The term self-similarity implies that regular patterns appear at all scales of observation. This self-similar scaling is expressed in the power-law relation which defines a fractal set according to

$$N_n = \frac{C}{r_n^D} \tag{3.1}$$

where N_n is the number of objects having a characteristic linear dimension r_n, C is a constant of proportionality and D is the fractal dimension. In general, the fractal dimension is not an integer but a fraction lying between the topological and Euclidian dimensions ($D_T < D < D_E$) and describes the jaggedness or degree to which the fractal pattern fills up the Euclidian space. For example, a profile of a rough surface is topologically a line (dimension 1), but is defined in Euclidian 2-space, and the fractal dimension falls between 1 and 2. In order to determine D, Equation (3.1) can be written as

$$D = \frac{\log(N_{n+1}/N_n)}{\log(r_n/r_{n+1})} \tag{3.2}$$

Objects that occur in nature rarely exhibit exact self-similarity. However, they often possess a related property, statistical self-similarity. A statistical fractal is defined by extending the fractal distribution (3.1) to a continuous distribution in which the number of objects N with a characteristic linear dimension greater than r satisfies

$$N = \frac{C}{r^D} \tag{3.3}$$

The power-law distributions (3.1) and (3.3) lack characteristic length scales and are thus applicable to scale-invariant phenomena.

The fractal concept can also be applied to the spatial or temporal variations of a single variable. There is, however, a fundamental difference between the fractal behaviour of the geometrical objects discussed above and the fractal behaviour of most random functions. Geometric objects are considered to exhibit fractal behaviour if they are self-similar over a range of scales. For most spatial or temporal random processes, the units of the dependent variable differ from those of the independent variable. In this case, the space/time series are statistically self-affine, *i.e.*, measurements taken at different resolutions have the same statistical characteristics when rescaled by factors that are generally different for the vertical and horizontal coordinates (Mandelbrot, 1983).

We can investigate the statistical features of a temporal random process by obtaining its power spectral density $S(f_T)$. As discussed by Voss (1985), a function $x(t)$ will have a Fourier transform for the period $0 < t < T$ given by

$$X(f_T, T) = \frac{1}{T} \int_0^T x(t) e^{2\pi i f_T t} dt \tag{3.4}$$

and a spectral density of

$$S(f_T) = \langle X(f_T, T) X(f_T, T)^* \rangle \tag{3.5}$$

where angular brackets denote time averaging. The spectral density $S(f_T)$ gives an estimate of the mean square fluctuations at frequency $f_T = 1/T$ and, consequently, of

the variations over a time scale of order $1/f_T$. For a time series that is fractal, the power spectral density has a power-law dependence on frequency

$$S(f_T) \sim f_T^{-\beta} \tag{3.6}$$

Similarly, for a fractal space series, we obtain power spectra of the form

$$S(f_\lambda) \sim f_\lambda^{-\beta} \tag{3.7}$$

where $f_\lambda = 1/\lambda$ is the spatial frequency and λ is the wavelength. A functional relationship between the fractal dimension D and the spectral exponent β was derived by Berry and Lewis (1980) as

$$D = \frac{5 - \beta}{2} \tag{3.8}$$

Numerical results of Fox (1989) suggest, however, that the predicted linear relationship in Equation (3.8) does not hold and can only be used as a reasonable approximation for $1 < \beta < 3$.

The special case of $\beta = 2.0$ in Equation (3.6) implies that the ratio of amplitude to wavelength (aspect ratio) of all component sinusoids is constant over all frequencies. Mixing fractal and spectral analysis terminology, the component sinusoids are self-similar in the case of $D = 1.5$. At all other values, the aspect ratio of the component sinusoids changes as a function of frequency, analogous to the fractal concept of self-affinity. For values of $\beta > 2.0$ ($D < 1.5$), the aspect ratio decreases with increasing frequency. That is, the features of the time series appear smoother at finer scales because the amplitude of high-frequency roughness is small compared to that at low frequencies. Conversely, for $\beta < 2.0$ ($D > 1.5$), the aspect ratio increases with increasing frequency, causing features to appear rougher at smaller scales since high-frequency roughness is more significant. Qualitatively, the fractal dimension is a "jaggedness" parameter, indicating the proportion of high- to low-frequency roughness.

3.3 Field observations

During the 1991 summer field season, two ploughmeters were installed at the bed of Trapridge Glacier (see Fig. 1.1). Figure 3.1 shows roughly 60 days of observation for ploughmeter 91PL02. We estimate that the ploughmeter was inserted ~15 cm into the basal sediment. Figure 3.1a indicates the bending force applied to the tip of the ploughmeter, and Figure 3.1b indicates the azimuth of the force with respect to the internal coordinates of the ploughmeter. During the entire observation period, both the force record and the azimuth record display a jagged appearance with rapid and large fluctuations. Variations in azimuth of the applied force could result either from rotation of the ploughmeter about its long axis or from translational motion in a direction perpendicular to the glacier flow. Because we believe that ploughmeters are firmly gripped by glacier ice (Chapter 2), it is unlikely that they will undergo large and rapid back-and-forth rotations within a borehole (Fig. 3.1b). Furthermore, other ploughmeter observations (see Chapter 4) indicate that the apparent rotation measured simultaneously with two ploughmeters can only be explained in terms of changes of the glacier flow direction. To further interpret the data, we postulate that azimuth variations due to changing glacier flow directions are generally long-term (cycles of one day or more) and that variations due to cross-flow motion are generally short-term (cycles of the order of hours or less). In our analysis, we used a Gaussian low-pass filter (cut-off frequency $\approx 0.074\,\mathrm{d^{-1}}$) to extract the slowly-varying component of the azimuth time series (dashed line in Fig. 3.1b) and attributed this slowly-varying component to changes in the glacier flow direction. Any remaining high-frequency disturbance on the azimuth record indicates non-zero cross-flow motion. By aligning the slowly-varying azimuth component with the glacier flow direction, we can decompose the net force values (Fig. 3.1a) into down-flow and cross-flow components (Fig. 3.2). To effect this decomposition we assume that the principal direction of ploughmeter motion is down-glacier.
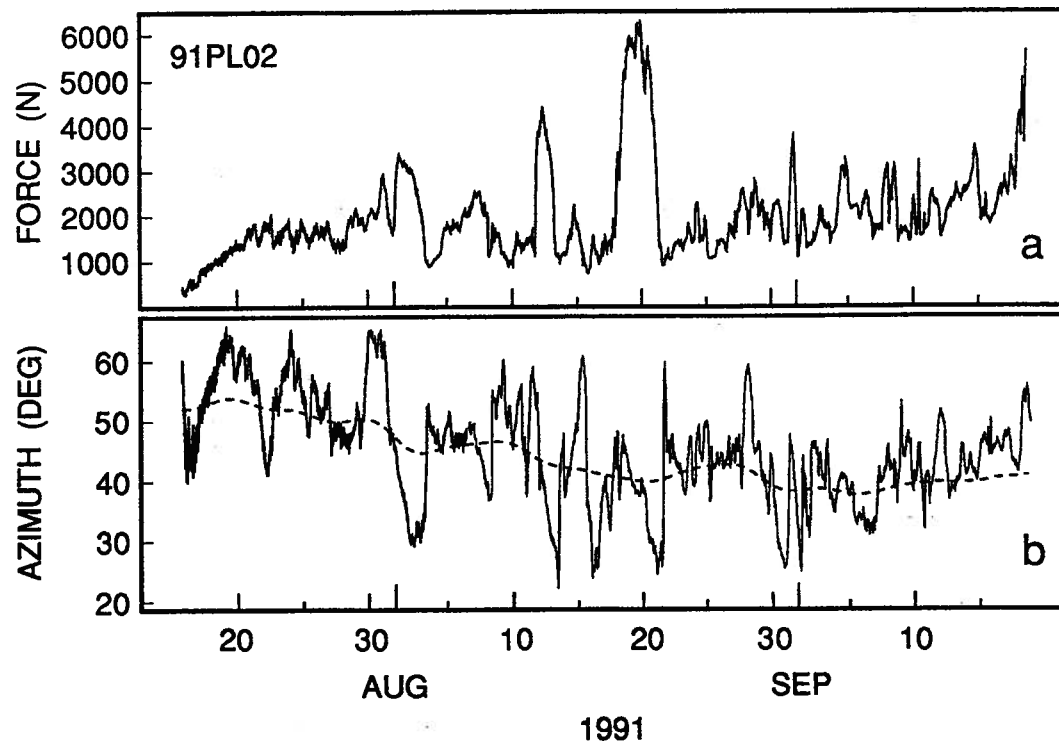
Fig. 3.1: Data from ploughmeter 91PL02. (a) Force record indicating force applied to the tip of the ploughmeter. (b) Azimuth of the force with respect to the internal coordinates of the ploughmeter. Dashed line represents the slowly-varying azimuth component (see text for details).

3.4 Interpretation

The jagged appearance of the force record (Fig. 3.1a) and the lack of an apparent correlation between the records of down-flow and cross-flow force components (Fig. 3.2) suggest that ploughmeter 91PL02 is interacting with a clast-rich area of the glacier bed. The basis for this suggestion lies in the idea that the spikes in the data record are the result of the ploughmeter colliding with individual clasts as it is dragged through basal material.

To support our idea we simulated collisions between a ploughmeter and individual clasts as the ploughmeter moves through a heterogeneous subglacial sediment. Chapter 2 presents a simple numerical model to describe the response of a ploughmeter
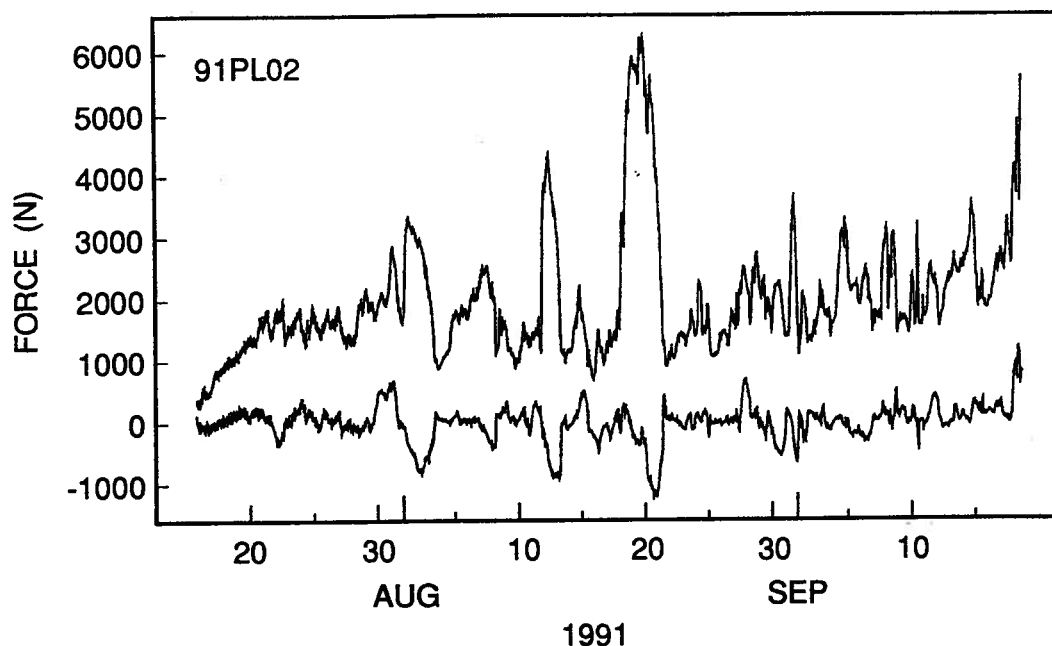
Fig. 3.2: Decomposition into down-flow (upper trace) and cross-flow (lower trace) force components of the data from ploughmeter 91PL02 shown in Figure 3.1.

to such forcing by interaction with a synthetic till. The model till was constructed assuming a porosity of 0.3 and a clast size distribution that is based on the analysis of grain sizes of a basal till from Trapridge Glacier (Clarke, 1987). The seven largest size classes were included in the model with clast diameters ranging from 4–32 mm (for more details of the numerical model see Section 2.4.1). Comparison of Figures 3.2 and 3.3 show that the records generated using this model display many of the features seen in the real data. Typical basal sliding rates at Trapridge Glacier, as indicated by drag spools, are $\gtrsim 40\,\mathrm{mm\,d^{-1}}$ (see Chapter 5). With this estimate of the glacier sliding velocity, ploughmeter 91PL02 would have travelled $\gtrsim 2.4\,\mathrm{m}$ through subglacial sediment during the period of observation. This conversion enables us to compare the model results (Fig. 3.3) with the observed data (Fig. 3.2) in more detail, and we note the lack of "broad" spikes in the synthetically generated record.
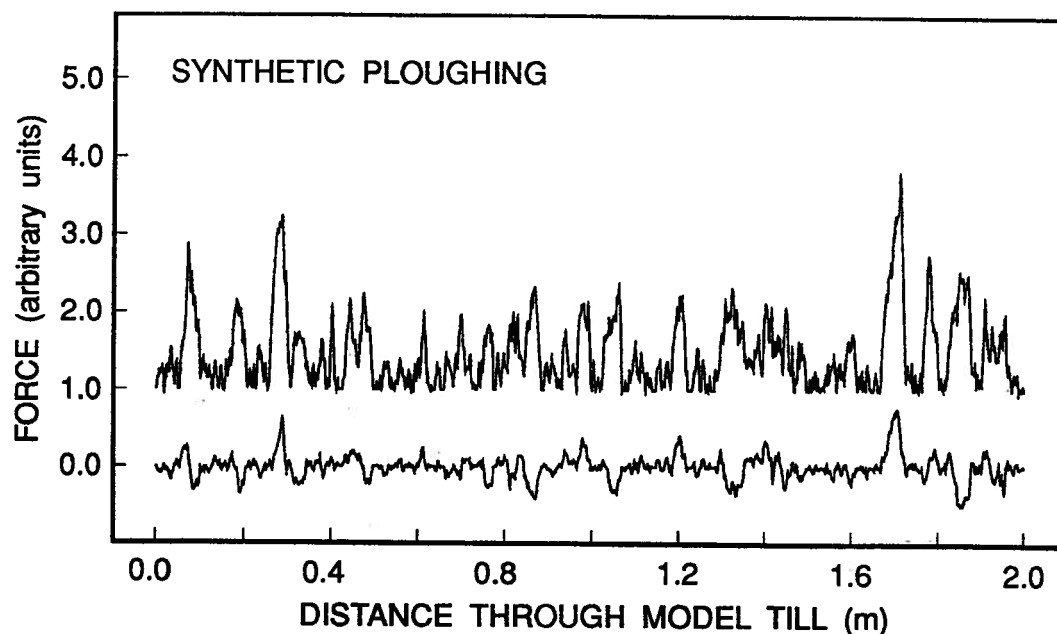
Fig. 3.3: Synthetically generated records of down-flow (upper trace) and cross-flow (lower trace) force components. Note the similar character to that of Figure 3.2.

3.4.1 Fractal scaling of Trapridge till

We suspect that the absence of broad spikes in the synthetically generated records of down-flow and cross-flow force components (Fig. 3.2) reflects the absence of clasts larger than 32 mm in diameter in our model till. Even though the largest clasts in the basal till sample from Trapridge Glacier (Clarke, 1987) were of this size, evidence from the ablation till in the forefield of the glacier indicates that the basal sediment layer contains clasts as large as cobbles and even boulders. The upper limit of clast diameter of 32 mm, as determined by sedimentological size analysis (Clarke, 1987), is likely to be artificial and results from a bias towards smaller clasts during the sampling procedure. The sampling involved filling a pail with roughly $0.008 \, m^3$ of "typical till", excluding material too large to shovel (Clarke, 1987). Clearly, the largest particles collected will be a function of the sample size taken and the sampling tools used. We illustrate

this idea in Figure 3.4, in which the distribution of different sized particles displays the property known as self-similarity. In this conceptual diagram of a cross section through a till, the self-similar nature of the particle-size distribution has been made obvious by recursively placing smaller particles into the voids between larger particles. If we were to examine this diagram at the smallest size scale, new and smaller particles would appear. Similarly, if we were to look at Figure 3.4 through a larger window, the largest clasts seen here would fill the gaps between even larger particles.

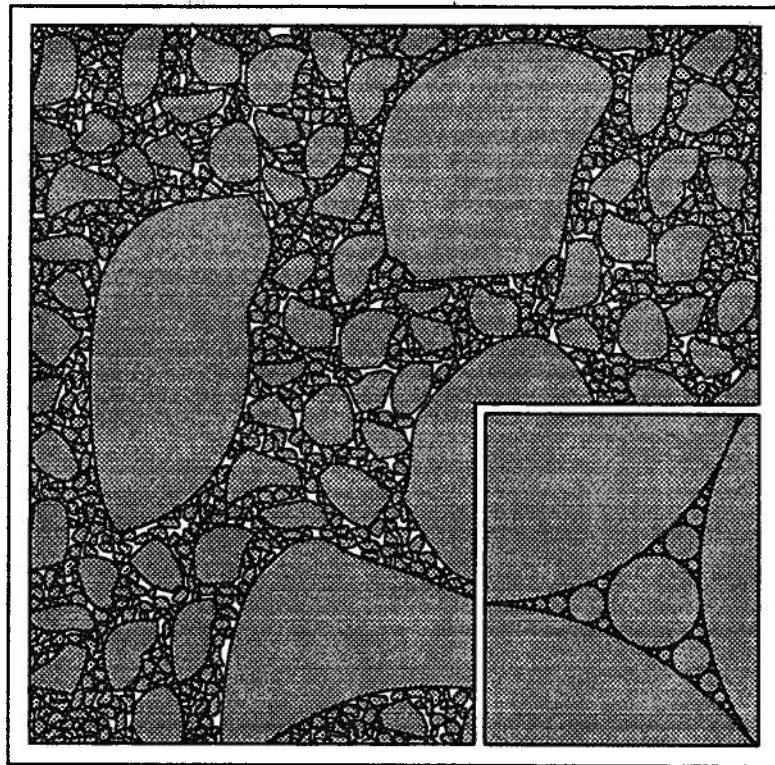Fig. 3.4: Conceptual diagram of the self-similar particle-size distribution in a cross sectional cut through a till. Inset shows a mathematically perfect Apollonian gasket (adapted from Mandelbrot, 1983, p. 170).

The cascades of smaller and smaller particles filling the gaps between larger particles is similar to the packing of circles in the mathematically perfect Apollonian gasket (Fig. 3.4, inset) (Mandelbrot, 1983, p. 170). There is an infinite number of smaller and smaller circles in any one curvilinear triangle formed by the bigger circles. We cannot tell the magnification of the overall structure of an Apollonian gasket because the whole system is self-similar at any scale. Thus, the size distribution of the different-sized circles packing the gasket is a fractal system. Likewise, due to the similarity, the particle distribution depicted in Figure 3.4 appears to resemble a statistically self-similar Apollonian gasket. We therefore suggest that the particle-size distribution of Trapridge till should be a fractal system similar to that of the theoretical Apollonian gasket system. If this is the case, fractal mathematics can be used to extrapolate our model till to grain sizes that are larger than 32 mm in diameter.

Rocks may be fragmented in a variety of ways. Weathering and grinding or crushing processes can lead to fragmentation. Fragments can also be produced by impacts and explosive processes, such as volcanic eruptions. If fragments are produced with a wide range of sizes and if natural scales are not associated with either the fragmented material or the fragmentation process, we would expect distributions of number versus size to be fractal.

A widely used statistical description used to represent the frequency–size distribution of fragments is the power-law relation

$$N = Cm^{-b} \tag{3.9}$$

where N is the cumulative number of fragments with mass greater than m. The constants C and b are chosen to fit observed distributions. Turcotte (1986) showed that the power-law distribution of Equation (3.9) is equivalent to the fractal distribution given in Equation (3.3). By defining a linear dimension r as the cube root of volume,

$r = V^{1/3}$, and assuming that the density is uniform, he noted that $m \sim r^3$. Now, comparing Equation (3.9) with Equation (3.3), he found that

$$D = 3b \tag{3.10}$$

The fractal dimension D defines the distribution of particles by size. For $D = 0$, the distribution is composed solely of particles having equal radius. When the fractal dimension is equal to 2.0, the number of particles greater than a given radius quadruples for each corresponding decrease in particle radius by one-half. A fractal dimension between 0 and 2.0 therefore reflects a greater number of larger particles, while a dimension greater than 2.0 reflects a distribution dominated by smaller particles.

Many experimental studies of the frequency–size distribution of materials fragmented by natural and industrial processes have been carried out. Table 3.1 lists more than twenty fragmented materials whose particle-size distribution behaves according to the fractal relation (3.3). Values of the fractal dimension are seen to vary considerably but most lie in the range $2.0 < D < 3.0$. Tyler and Wheatcraft (1989) investigated size distributions for 10 soils ranging in texture from sand to silty clay loam to silt. The fractal dimension of the distributions ranged from 2.7 to 3.485 and generally increased as the mean grain size decreased. Of the distributions listed in Table 3.1, those representing soils have fractal dimensions approaching 3.0, which is consistent with the results from Tyler and Wheatcraft (1989). Hartmann (1969) stated that the conditions under which rocks are fragmented play a significant role in determining the frequency–size distribution of the fragments. He found that values of the fractal dimension appear to be correlated with the degree of abrasion, grinding, and crushing — large D values being "associated with large expenditures of energy per particle". This finding accords with the results from fracture experiments on tuff, granite and basalt by Matsui and others (1982) that show that the fractal dimension of the size distribution of the fragments increases as the imparted energy density increases.

Material	D	Reference
Singly fractured basalt blocks	1.80	1
Artificially crushed quartz	1.89	1
Multiply fractured basalt blocks	2.01	1
Disaggregated gneiss	2.13	1
Disaggregated granite	2.22	1
Disintegrated igneous boulders	2.37	1
Disintegrated igneous glacial boulder	2.40	1
Fragmented granite (chemical explosion, 0.2 kt)	2.42	2
Fragmented granite (nuclear explosion, 61 kt)	2.50	2
Broken coal	2.50	3
Interstellar grains	2.50	4
Projectile fragmentation of quartzite	2.55	5
Projectile fragmentation of basalt	2.56	6
Fault gouge	2.60	7
Sandy clays	2.61	1
Detritus from weathered gneiss	2.67	1
Terrace sands and gravels	2.82	1
Glacial till (Engabreen)	2.84	8
Glacial till	2.88	1
Glacial till (Storglaciären)	2.92	8
Glacial till (Ice Stream B)	2.96	8
Ash and pumice	3.54	1

Table 3.1: Fractal dimensions for a variety of fragmented materials. (References are (1) Hartmann (1969), (2) Schoutens (1979), (3) Bennett (1936), (4) Mathis (1979), (5) Curran and others (1977), (6) Fujiwara and others (1977), (7) Sammis and Biegel (1989), (8) Hooke and Iverson (1995))

We studied the frequency–size distribution of a basal till sample obtained from Trapridge Glacier by Clarke (1987) by plotting the cumulative number of particles larger than a given sieve size versus the particle size (Fig. 3.5). If plotted on a log-log scale, we see that Trapridge till shows clear fractal or power-law scaling behaviour over the whole range of sampled grain sizes. The fractal dimension D is equivalent to the negative of the slope of the log particle size versus log number of particles (Fig. 3.5) and was calculated by using a least-squares regression. A good correlation with the fractal relation (3.3) is obtained over five orders of magnitude and gives $D = 2.95$. Note that

log-log plots suppress any subtle features of grain-size distributions. Thus, evidence for bimodality would be obscured by graphs of this kind.

The relatively large D value for our sample of basal till is probably the result of repeated abrasion taking place in the deformable sediment layer beneath Trapridge Glacier. Our finding is in agreement with the statement of Hartmann (1969) that geological samples, such as streambeds, alluvial fans, and glacial tills, have commonly been exposed to extreme grinding and crushing processes. In addition, our value of the fractal dimension for Trapridge till is consistent with those determined by Hooke and Iverson (1995) for three subglacial tills (ranging between 2.84 and 2.96) that have been shown to undergo shear deformation (see Table 3.1).
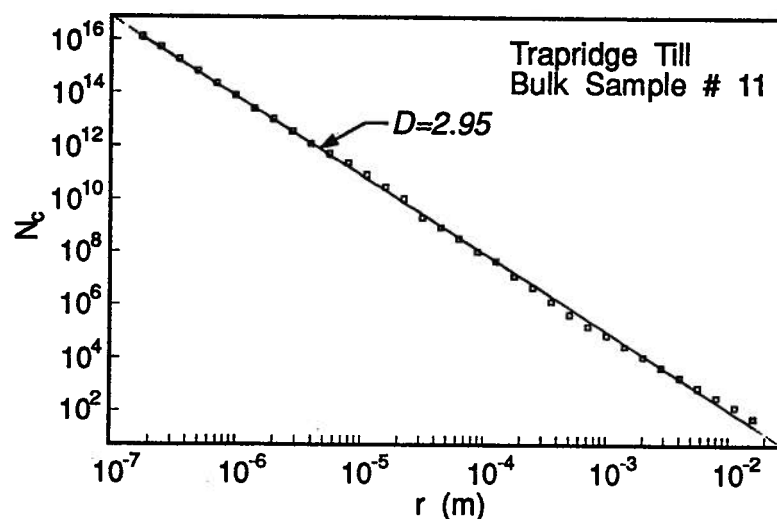

Fig. 3.5: The number N of particles with radius greater than r as a function of r for a sample of basal till from Trapridge Glacier. The solid line represents Equation (3.3) with $D = 2.95$.

3.5 Estimation of basal sliding rate

One implication of the fractal scaling of Trapridge till is that the response of a plough-meter also obeys fractal statistics. Because the interaction of a ploughmeter with the till will partly be influenced by the clast-size distribution, we expect the frequency-amplitude statistics of the force record to be fractal.

For both the data of ploughmeter 91PL02 (Fig. 3.2) and the synthetically generated data (Fig. 3.3), the records of the cross-flow force component were analyzed by the Fourier transform method (Press and others, 1992, p. 490), and the power spectral densities were estimated using the periodogram method (Press and others, 1992, p. 542). Both log-log plots — spectral energy $S_x(f_T)$ versus frequency f_T for the 91PL02 data (Fig. 3.6) and spectral energy $S_x(f_\lambda)$ versus spatial frequency f_λ for the synthetic data (Fig. 3.7) — show good power-law dependence over large portions of the spectra. Here, the subscript x indicates that the power spectra were calculated for the cross-flow force components (lower traces of Figs. 3.2 and 3.3). The least-squares log-log slopes from Equations (3.6) and (3.7) on the quasi-linear sections of the spectra give $\beta = 2.7$ for both cases. The corresponding fractal dimension from Equation (3.8) is $D = 1.15$, which we will refer to as the fractal dimension of the ploughmeter response. Obtaining the same value of spectral exponent β and consequently the same fractal dimension D for the data of ploughmeter 91PL02 and for the synthetically generated data indicates that the rate of change of power with scale is the same in both cases. This finding further validates the applicability of our simple numerical model to simulate collisions of a ploughmeter with individual clasts. However, for the model results (Fig. 3.7) the power spectrum rolls off at low spatial frequencies, an effect that is less noticeable for the spectrum of the 91PL02 data (Fig. 3.6). We attribute this difference again to the lack of clasts larger than 32 mm in diameter in the model till. We will further discuss this roll-off in Section 3.6 (below).

Fig. 3.6: Power spectral density function for the record of the cross-flow force component shown in Figure 3.2. The dashed line represents Equation (3.6) with $\beta = 2.7$ ($D = 1.15$).

The power-law spectra given in Figures 3.6 and 3.7 provide further information beyond simply the fractal dimension. In addition to the slope, the spectra are characterized by a spectral intercept which represents the power of a sinusoid of frequency $f_T = 1\,\mathrm{d}^{-1}$ or spatial frequency $f_\lambda = 1\,\mathrm{m}^{-1}$. The spectral intercepts of the two power spectra in Figures 3.6 and 3.7, unlike the spectral exponents, are not equal for the following reasons: (1) The amplitudes in the records of the cross-flow force component (Figs. 3.2 and 3.3) differ by more than three orders of magnitude. (2) The force record of ploughmeter 91PL02 (Fig. 3.2) represents a time series (horizontal axis in units of time) whereas units of distance along the horizontal axis in the force record of the synthetic data (Fig. 3.3) characterize a space series.

Because the power-law relations (3.6) and (3.7) are independent of scale, knowledge of the actual power at a specified scale is not required and we can normalize the two power spectra. This normalization corresponds to a relative, vertical displacement of
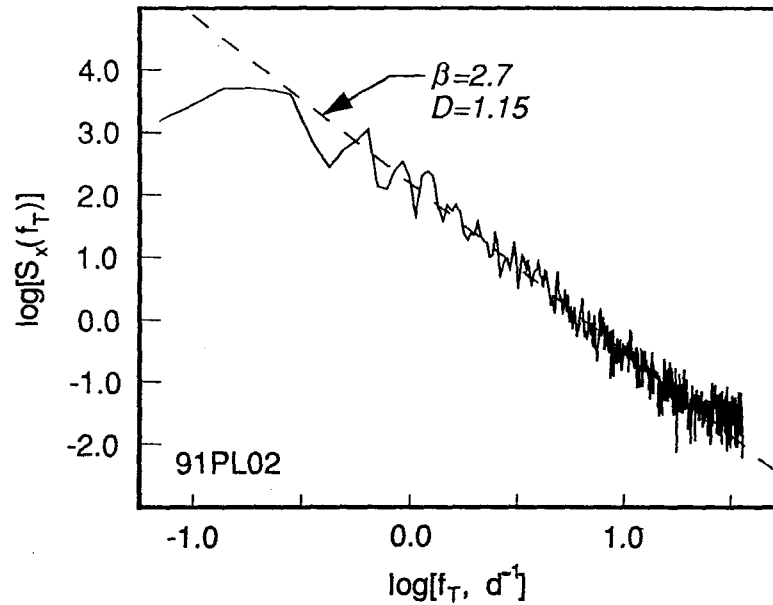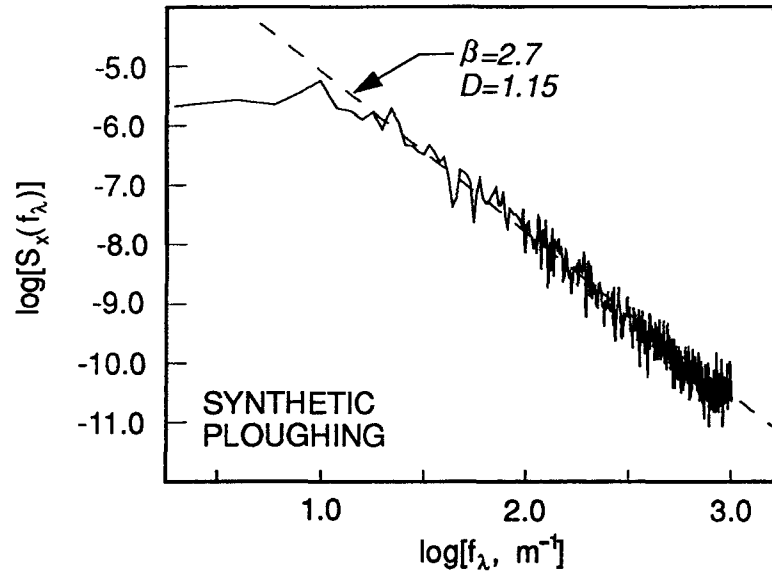
Fig. 3.7: Power spectral density function for the record of the cross-flow force component shown in Figure 3.3. The dashed line represents Equation (3.7) with $\beta = 2.7$ ($D = 1.15$). Notice the roll-off in power at low spatial frequencies.

the power spectra in log-log space. Now we can use reason (2) to make an estimate of the glacier sliding rate. By multiplying the spatial frequency f_λ by the velocity v with which the ploughmeter is being dragged through the till, we obtain the frequency f_T. This operation is equivalent to linearly translating one of the power spectra in log-log space along the horizontal axis, *i.e.*,

$$\log f_T = \log f_\lambda + \log v \tag{3.11}$$

If we denote the spectral intercepts of the normalized power spectra for the data of ploughmeter 91PL02 and the synthetic data with α_T and α_λ, respectively, we can calculate the velocity that will achieve perfect overlap of the two power spectra, thus

$$v = 10^{(\alpha_T - \alpha_\lambda)/\beta} \tag{3.12}$$

The velocity v in Equation (3.12) represents the differential velocity between plough-meter and sediment and is equivalent to the basal sliding rate of the glacier if sediment deformation is neglected. For the synthetic data set described above and illustrated in Figures 3.3 and 3.7 we calculate a sliding velocity of $36 \, \mathrm{mm \, d^{-1}}$. We recall that the model till was assumed to have a porosity of 0.3 (Section 2.4.1). Similar analyses for different model tills with porosities ranging from 0.1 to 0.5 yield a basal sliding rate that is a function of porosity as shown in Figure 3.8. The glacier sliding velocities of $\sim$30–50 $\mathrm{mm \, d^{-1}}$ calculated in this way are therefore in excellent agreement with direct measurements of sliding at the base of Trapridge Glacier using a drag spool ($\sim$40–60 $\mathrm{mm \, d^{-1}}$, see Chapter 5).
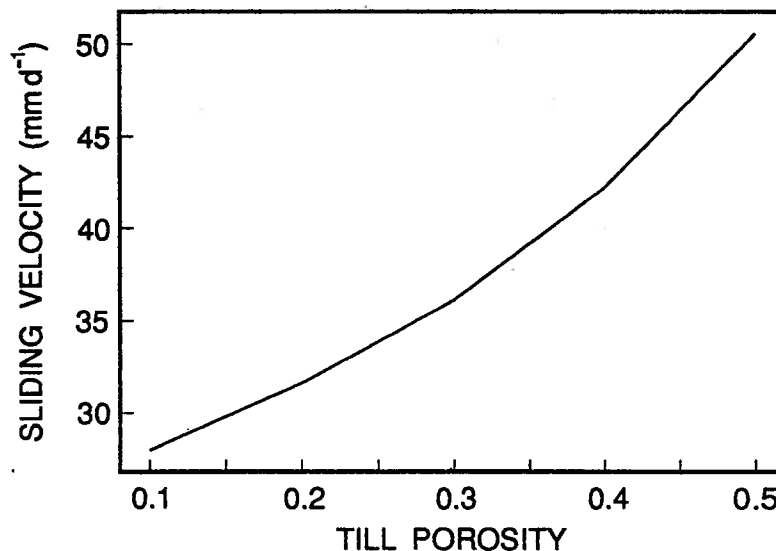

Fig. 3.8: Summary of the relationship between sliding velocity of Trapridge Glacier and till porosity as calculated using the clast collision model.

3.5.1 Discussion

In our analysis we had assumed a spatially uniform size distribution and that temporal variations in sliding rate are negligible. If, however, the subglacial sediment texture is unknown and the clast collision frequency is observed to vary with time, two contrasting interpretations present themselves: (1) the sliding rate is constant and sediment texture spatially inhomogeneous; (2) the sediment texture is spatially homogeneous and the sliding rate varies temporally. In the latter case, sliding rate is proportional to the clast collision frequency. Suppose that sliding occurs at some constant rate v_0 and that clast collisions yield a ploughmeter response $x(t)$. The frequency content of this response can be represented by the power spectrum $S(f_T)$ given by Equation (3.5). If, at some subsequent time, the sliding velocity changed to some new but constant value $v' = \gamma v_0$, the time axis of the ploughmeter response would become rescaled as $t' = t/\gamma$ to yield a response x' having a power spectrum $\gamma^2 S(\gamma f_T)$. (This result follows from the Fourier transform similarity theorem; see *e.g.*, Bracewell, 1986, p. 101). Thus, the relative change in sliding rate $\gamma = v'/v_0$ produces a proportional rescaling of the frequency axis. It may therefore prove possible to use ploughmeters to observe seasonal variations in the basal sliding rate.

3.6 Fractal response of ploughmeter–till interaction

Recalling that the fractal dimension of the particle-size distribution may be regarded as a measure of the till texture, we proceed by investigating the impact of changes in fractal scaling of the particle sizes upon the mechanical behaviour of the ploughmeter. Using the numerical clast collision model introduced in Section 2.4.1 we seek an empirical relationship between the fractal dimension of the particle-size distribution and the fractal dimension of the ploughmeter response. Based on a discrete model of fragmentation we present a simple method for generating different frequency–size

distributions of particles for our model till. The fragmentation model, which was developed by Turcotte (1992) and is illustrated in Figure 3.9a, yields a specific fractal dimension. A cube of linear dimension h is divided into eight equal-sized cubic blocks with dimensions $h/2$. We consider fragmentation such that some blocks are retained at each scale but others are fragmented. In the model given in Figure 3.9a two diagonally opposed blocks are retained at each scale. We therefore have $N_1 = 2$ for $r_1 = h/2$, $N_2 = 12$ for $r_2 = h/4$, and $N_3 = 72$ for $r_3 = h/8$. From Equation (3.2) we find that $D = \log 6/\log 2 = 2.585$. This is the fractal distribution of a discrete set which we want to compare with statistical fractals obtained from actual particle-size distributions. It is therefore of interest to consider also the cumulative statistics, where N_{nc} denotes the cumulative number of the fragments equal to or larger than r_n. For the model illustrated in Figure 3.9a we have $N_{1c} = 2$ for $r_1 = h/2$, $N_{2c} = 14$ for $r_2 = h/4$, and $N_{3c} = 86$ for $r_3 = h/8$ (Fig. 3.9b). Excellent agreement with the fractal relation (3.3) is obtained by taking $D_c = 2.593$. Thus the fractal dimensions for the discrete set (D) and the cumulative statistics (D_c) are nearly equal.

After carrying out an infinite number of recursions, retaining some blocks and fragmenting others, we obtain a fractal cube which is self-similar at all scales smaller than the initial cube (Fig. 3.9a). Once the fractal cube has been generated, the fragmentation model forms the basis for the frequency–size distribution of the model till with a specific fractal dimension. The numbers of the various sized blocks in a fractal cube determine the numbers of spheres of different sizes in our model till.

Synthetic ploughmeter data were generated for seven different frequency–size distributions of model till. Each distribution is based on a fractal cube which has a slightly different generating algorithm and therefore a different fractal dimension (Table 3.2). For every synthetically generated record of the cross-flow force component, the power spectral density was estimated and Equation (3.7) was fitted using a linear least-squares regression in log-log space.
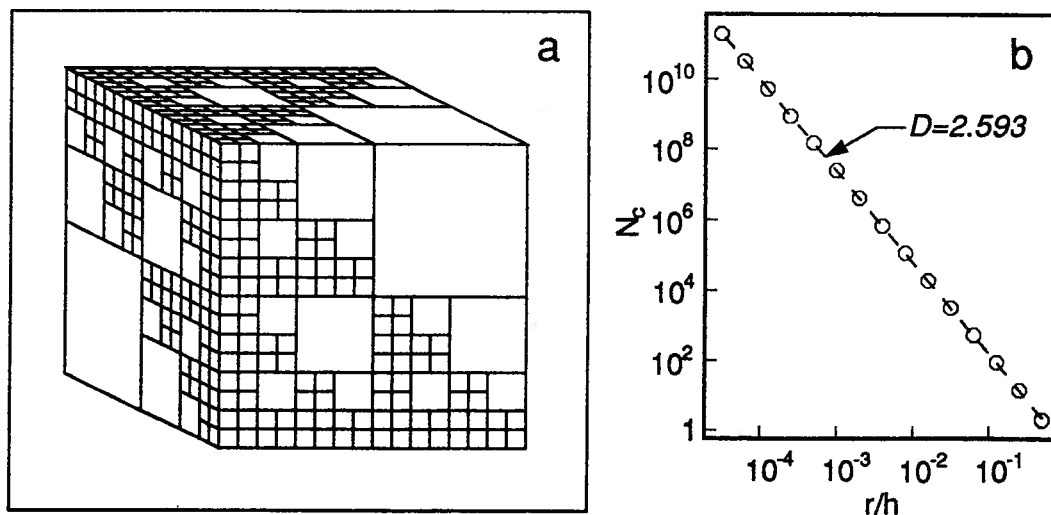
Fig. 3.9: (a) Illustration of a fractal model for fragmentation. Two diagonally opposite cubes are retained at each scale. With $r_1 = h/2$, $N_1 = 2$ and $r_2 = h/4$, $N_2 = 12$ we have $D = \log6/\log2 = 2.585$ (Turcotte, 1992). (b) Cumulative statistics for the fragmentation model illustrated in (a). Correlation with Equation (3.3) gives $D_c = 2.593$.

N_1	N_2	N_3	N_n	D	D_c
6	12	24	$6 \times 2^{n-1}$	1.0	1.039
5	15	45	$5 \times 3^{n-1}$	1.585	1.605
4	16	64	$4 \times 4^{n-1}$	2.0	2.013
3	15	75	$3 \times 5^{n-1}$	2.322	2.331
2	12	72	$2 \times 6^{n-1}$	2.585	2.593
1	7	49	7^{n-1}	2.807	2.814

Table 3.2: Fractal dimensions for a variety of fragmentation models.

For a low fractal dimension of the particle-size distribution, the model till is predominantly composed of larger particles and we expect more large scale interactions. On the other hand, a high fractal dimension indicates that the till consists of a significantly increasing number of smaller size particles which would result in an increase of small scale interactions. The power spectrum of the force record in the first case will therefore contain more low spatial frequency energy while in the second case more energy will be contained in the higher spatial frequencies. As a consequence, the slope of

the quasi-linear curve which characterizes the power spectrum in log-log space should decrease with increasing fractal dimension of the particle-size distribution of the model till. We can see some evidence of this inverse relation in Figure 3.10.
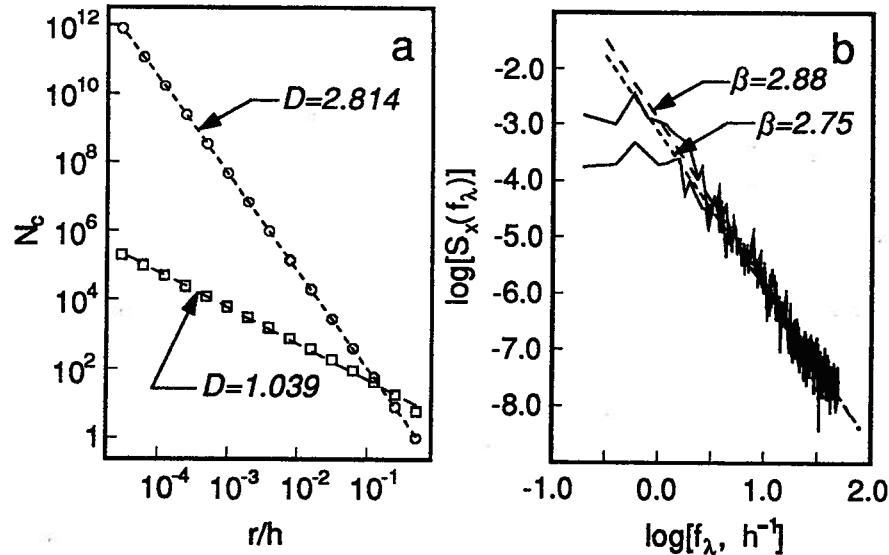
Fig. 3.10: Illustration of the inverse relationship between fractal dimension of the particle-size distribution of the model till and the slope of the power spectrum for the synthetically generated ploughmeter response. (a) Cumulative statistics for two fragmentation models listed in Table 3.2 with $D_c = 1.039$ (long dashed line) and $D_c = 2.814$ (short dashed line). (b) Composite of two power spectra plotted on log-log scales for two synthetically generated ploughmeter responses using model tills having particle-size distributions shown in (a).

The fractal dimension of the ploughmeter response can be determined from the log-log slope using Equation (3.8). Figure 3.11 displays the empirical relationship between the fractal dimension of the particle-size distribution and the fractal dimension of the ploughmeter response.
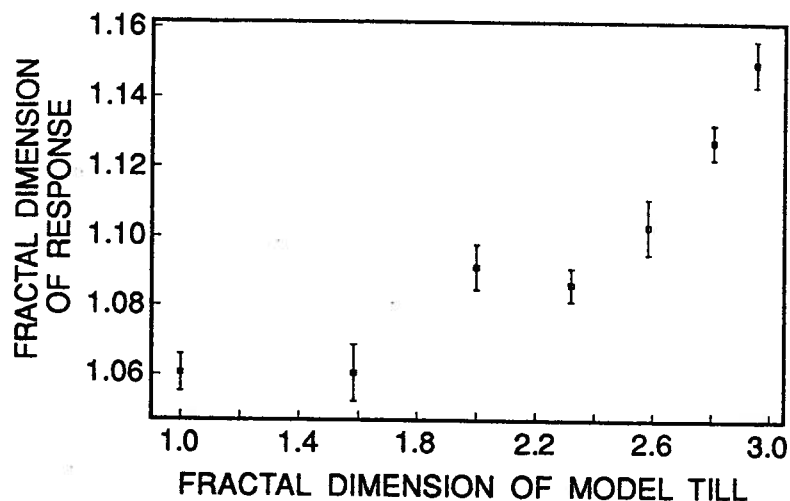
Fig. 3.11: Dependence of the fractal dimension of the ploughmeter response on the fractal dimension of the particle-size distribution. The error bars reflect the uncertainty in determining the log-log slopes of the quasi-linear sections in the power spectra.

Here, we included a model till whose particle-size distribution has a fractal dimension $D = 2.953$ ($D_c = 2.954$). This fractal distribution is based on a fragmentation model in which a cube is divided into 64 cubic blocks rather than 8 as in the case of the models listed in Table 3.2. The fractal dimension of the ploughmeter response for this case is $D = 1.15$ and agrees with that obtained for the data of ploughmeter 91PL02 (Fig. 3.6). From Figure 3.11 we see that the response of the ploughmeter displays only a weak dependence on the particle-size distribution. A change of the fractal dimension of the model till by a factor of three is accompanied by only a 10% change in the fractal dimension of the ploughmeter response.

These conclusions are based on model tills whose particles, though having a fractal size distribution, were randomly placed in space (see Section 2.4.1). A different result might be expected if the model tills are constructed by distributing the particles in space in a fractal arrangement similar to that depicted in Figure 3.4. This possibility is currently being explored separately.

As a second application we use the fragmentation model to investigate the roll-off in power at low spatial frequencies in the spectrum of the model results (Fig. 3.7, Section 3.5). For a model till with a particle-size distribution based on the fractal cube with fractal dimension $D = 2.585$ (Fig. 3.9a) we generated three sets of synthetic ploughmeter data. The largest clasts in the model till for the first data set were of diameter $h/2$. Subsequently, this clast size class was removed, leaving $h/4$ diameter particles to be the largest clasts for the second data set. We continued this procedure for one further iteration to obtain a model till for the third data set where the largest clasts have a diameter of $h/8$. The resulting power spectra for these three data sets are shown in Figure 3.12. We notice that the roll-off in power becomes more prominent as the size of the largest clasts in the model till decreases.
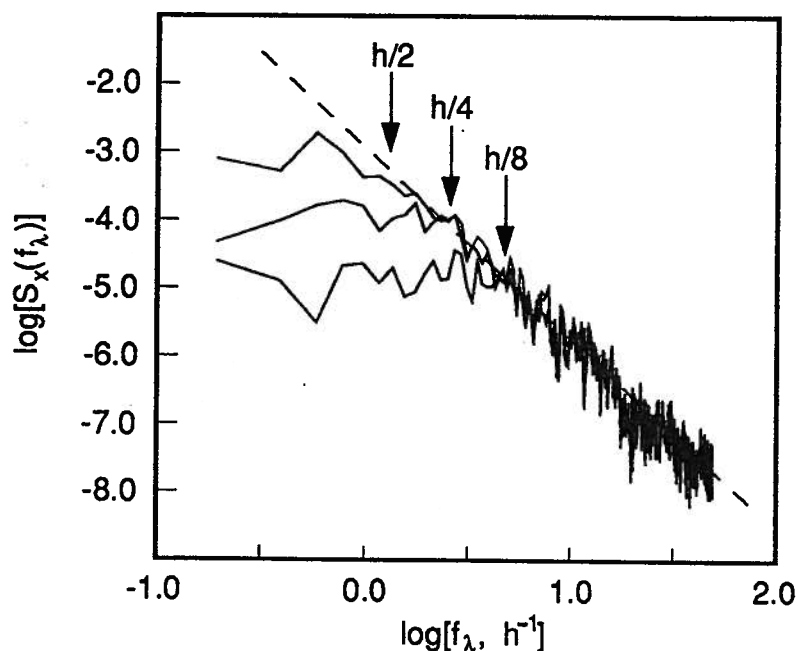

Fig. 3.12: Composite of three power spectra for three synthetic plough-meter interactions with a model till whose particle-size distribution is based on the fractal cube illustrated in Figure 3.9a. Arrows point to the roll-off points. Largest clasts in the model till have diameters $h/2$, $h/4$, and $h/8$.

Furthermore, the spatial frequency at which the power spectrum rolls off can be directly related to the size of the largest clasts in the model till. For the three power spectra the roll-off points correspond roughly to wavelengths (see arrows in Figure 3.12) which are about twice the diameter of the largest clasts in the respective model tills.

3.7 Concluding remarks

In this chapter, we have explored the usefulness of the ploughmeter as a tool for studying sediment texture. Analysis of the particle-size distribution of Trapridge sediment revealed that the size distribution forms a fractal system. This fractal scaling behaviour is not only an efficient representation of the frequency–size distribution of a sediment sample but also provides a useful extrapolation principle for the grain-size distribution to size scales that have not been sampled. We demonstrated that the response of ploughmeters interacting with a self-similar sediment also obeys fractal statistics. This result inspired us to examine whether we can relate the spectral characteristics of the ploughmeter response to the size distribution of the subglacial sediment. Regrettably, the fractal dimension of the ploughmeter response is remarkably insensitive to the fractal dimension of the particle-size distribution. We therefore concluded that it is not feasible to infer subglacial sediment texture from the response spectrum of ploughmeters. However, if the sediment texture is known and assumed to be spatially uniform, we can use the spectral response of a ploughmeter to estimate the basal sliding velocity. In the next chapter we apply data recorded with two ploughmeters and a water pressure sensor to study mechanical and hydrological coupling at the ice–bed interface.

Chapter 4

EVIDENCE FOR TEMPORALLY-VARYING "STICKY SPOTS"

"I am a kind of burr; I shall stick."

- William Shakespeare

4.1 Introduction

The flow of glaciers and ice streams is driven by gravity and opposed by resistive forces. The sources of the restraining forces that act at the bed are some unknown combination of so-called "sticky spots" at the ice–bed interface and bedrock roughnesses in the case of a hard-bedded glacier or the rheological properties of the basal material in the case of a soft-bedded glacier. Sticky spots are localized regions of the bed where the basal shear stress is concentrated and that balance some or all of the applied driving stress (Alley, 1993).

Recent data from West Antarctica suggest the presence of sticky spots that support high basal shear stress and that are surrounded by a generally well-lubricated, low-shear-strength bed. Force-budget calculations for ice flow at the Byrd Station Strain Network (Van der Veen and Whillans, 1989), where surface measurements were used to infer stresses at depth, showed that the basal drag is highly variable across the bed and concentrated at a few distinct sticky spots. These high-drag, slow-sliding sites are not always correlated with basal topographic highs, indicating that some process such as basal water drainage is involved in controlling resistance at the bed. MacAyeal (1992) used control methods to invert the observed surface velocity pattern of Ice Stream E for the distribution of subglacial friction. Irregularity of this inferred distribution suggests that the ice is not underlain by a uniform layer of deformable sediment and that increased basal friction is introduced by rigid bedrock or by variations in

60

subglacial water pressure. Alley and others (1994) suggested that basal water has been diverted away from Ice Stream C, resulting in a disruption of the lubricating water film. They therefore hypothesized that the ice stream has slowed and stopped due to the basal stress on a few sticky spots at the bed. Neighboring Ice Stream B flows rapidly (400–$800\,\mathrm{m\,a^{-1}}$) despite its similarity to Ice Stream C in physical dimensions, accumulation, temperature (Shabtaie and others, 1987) and substrate properties (Rooney and others, 1987; Atre and Bentley, 1993). Anandakrishnan and Alley (1994) suggest that sticky spots exist beneath Ice Stream B, but rarely manifest themselves in the force balance at the bed since they are better lubricated than those beneath Ice Stream C. This conclusion is supported by observations that microseismic events are 20 times more abundant at the base of Ice Stream C than at the base of Ice Stream B (Anandakrishnan and Bentley, 1993). The more frequent occurrence of microseismic events beneath Ice Stream C points to a difference in frictional character of sticky spots between the fast- and slow-moving ice streams.

The foregoing discussion highlights the reasons for current interest in the characteristics of subglacial sticky spots and the larger issue of ice–bed coupling. Simultaneous measurements of subglacial water pressure and ploughmeter response offer a unique approach to studying the mechanical and hydrological coupling between a glacier and its bed. In this chapter, we interpret data from two ploughmeters in terms of changes in basal sliding velocity in response to fluctuations of subglacial water pressure. We develop a mathematical model to describe the sliding motion of glacier ice over a flat surface having spatially and temporally variable drag. Solving for the velocity field of the ice immediately above the glacier bed, we can calculate the behaviour of ploughmeters as they respond to temporal and spatial evolution of basal resistance. Comparison of our model results with field measurements yields evidence for temporal and spatial variations of sticky spots that are linked to changes in basal lubrication.

4.2 Field observations

In July 1992, arrays of ploughmeters and subglacial water pressure transducers were installed beneath Trapridge Glacier. Figure 4.1 shows 15 days of observations for ploughmeters 92PL02 and 92PL05. Data from subglacial water pressure sensor 92P06 are also included and plotted along the same time axis. All three instruments are located within a circle of diameter ~10 m (Fig. 4.2) in the general vicinity of the 1991 ploughmeter positions. The two ploughmeters 92PL02 and 92PL05 were inserted approximately 10 m apart in boreholes that connected to the basal hydrological system. The line joining the two insertion sites was at an angle of ~8° from the direction of glacier flow (Fig. 4.2).

Fig. 4.1: Next page: Data from ploughmeters and pressure sensor. (a) Force record indicating force applied to the tip of ploughmeter 92PL02. (b) Azimuth of the forces with respect to the internal coordinates of ploughmeter 92PL02. (c) Force record indicating force applied to the tip of ploughmeter 92PL05. (d) Azimuth of the forces with respect to the internal coordinates of ploughmeter 92PL05. (e) Subglacial water pressure record from pressure sensor 92P06. Super-flotation pressures correspond to a water level of more than about 63 m.
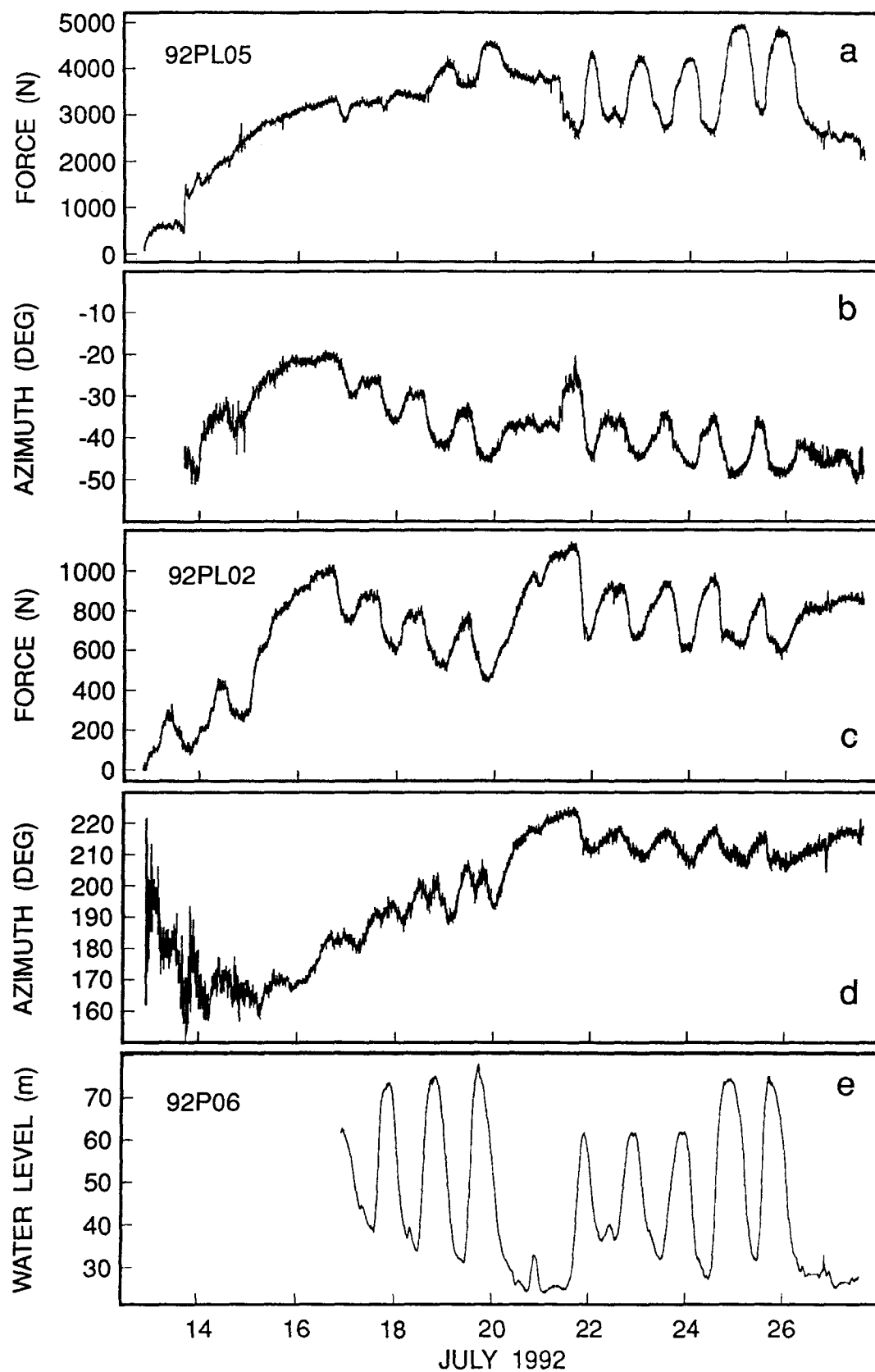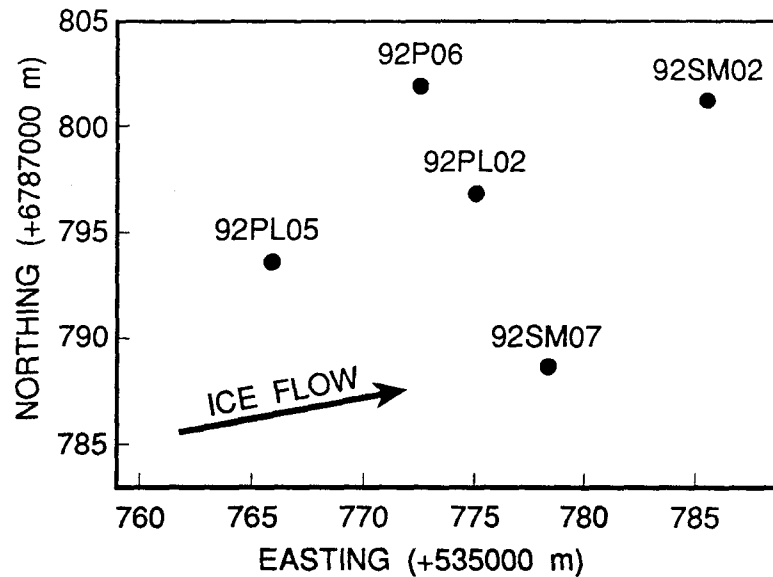
Fig. 4.2: Location map of sensors during the 1992 summer field season. Data from sensors 92SM02 and 92SM07 are presented and discussed in Chapter 5.

The records of both ploughmeters (Figs. 4.1a–4.1d) display strong diurnal signals which appear to be correlated to large and rapid fluctuations in subglacial water pressure registered with sensor 92P06 (Fig. 4.1e). This correlation suggests that mechanical conditions at the glacier bed vary temporally in response to changes in the basal hydrological system. However, there is a fundamental difference in how the two ploughmeters respond to these changes in basal conditions. In the case of ploughmeter 92PL05 we see that variations in subglacial water pressure (Fig. 4.1e) are in phase with variations in the force response (Fig. 4.1a): high and low water pressures correspond to high and low forcings, respectively. In fact, for the time period starting 21 July, the two records look virtually identical, even at the finest detail. In contrast, peak water pressures appear to coincide with low forcings experienced by ploughmeter 92PL02 and *vice versa* (Figs. 4.1c and 4.1e). Thus, comparing Figures 4.1a and 4.1c, we observe

that the force record of ploughmeter 92PL05 indicates a response that is 180° out-of-phase with respect to that of ploughmeter 92PL02. At the same time, however, the azimuth records (Figs. 4.1b and 4.1d) indicate ploughmeter responses that are in-phase with each other: both ploughmeters appear to be rotating in the same sense back and forth about their long axes by roughly 10–15°.

4.3 Qualitative interpretation

The correlation between the azimuth responses coupled with the strong anti-correlation between the force responses of the two ploughmeters could suggest: (1) that one ploughmeter is forcing the other, or (2) that both ploughmeters are responding to the same external forcing. While we do not believe that the response of one ploughmeter can force that of another, in the following analysis, we investigate the possibility that the mechanical behaviour of ploughmeters is forced by variations in subglacial water pressure by a mechanism that operates differently for the two ploughmeters.

In Section 2.4.3 we saw that, if subglacial sediment is treated as a layer of Newtonian viscous fluid, then the force on a ploughmeter that is moving through it, is linearly proportional to the effective fluid viscosity μ, the translational velocity v, and the shape and dimensions of the section of ploughmeter immersed in sediment (see Equation (2.9) in Section 2.4.3). The translational velocity v is equal to the basal glacier sliding velocity v_b if subglacial sediment deformation is neglected. Thus, variations in the force response of a ploughmeter could be due to any or all of the following: changes in the strength of basal material, changes in glacier sliding rate, and changes in ploughmeter insertion depth into subglacial sediment. However, as previously analyzed (see Section 2.4), we completely ignore the possiblity of a ploughmeter being lifted out and re-inserted into the sediment as a result of vertical uplift of the glacier driven by pressurized water between ice and bed. Furthermore, we assume that the strength of basal material is not significantly affected by fluctuating subglacial water

pressures and, hence, effective pressures. This assumption is reasonable because the low hydraulic conductivity usually associated with glacial sediments means that changes in subglacial water pressure take some time to diffuse into the sediment, which makes a near-instantaneous response of a ploughmeter unlikely. For this discussion, we therefore attribute all of the variations in the force response of a ploughmeter to changes in basal sliding rate in response to fluctuating subglacial water pressures.

Our measurements of water pressure beneath Trapridge Glacier show, that at any given time, basal water pressure is not uniform over the glacier bed (Stone, 1993). In addition, large spatial pressure gradients can be observed between boreholes that are connected and those that are unconnected to the subglacial drainage system (Murray and Clarke, 1995). These observations suggest that we must treat mechanical conditions at the glacier bed on a local scale rather than globally for the glacier as a whole, because mechanical conditions should vary in response to localized changes in the subglacial hydrological system. In the following, we base our interpretation on the idea that a lubricating water film is associated with high subglacial water pressure, which effectively decouples the glacier from its bed and promotes sliding. In contrast, low pressures cause increased bottom drag.

We consider a patch of glacier bed over which, at a starting time $t = t_1$, the basal water pressure is low. There is good coupling between the glacier and the subglacial sediment since bed lubrication is poor. Basal resistance is higher than average and little slip occurs between the sedimentary material and the overlying ice (Fig. 4.3a). At a later time $t = t_2$, subglacial water pressure has increased over the same patch. Now the ice–sediment interface is well lubricated, resulting in a strong local decoupling of the glacier from its bed, so that ice is allowed to slide freely over this patch with lower-than-average bottom drag (Fig. 4.3b). As the water pressure rises on the patch of glacier bed under consideration, some of the normal load of the overlying ice will be

redistributed onto surrounding regions. This lateral transfer of loading is accompanied by an increase in basal resistance in those regions.
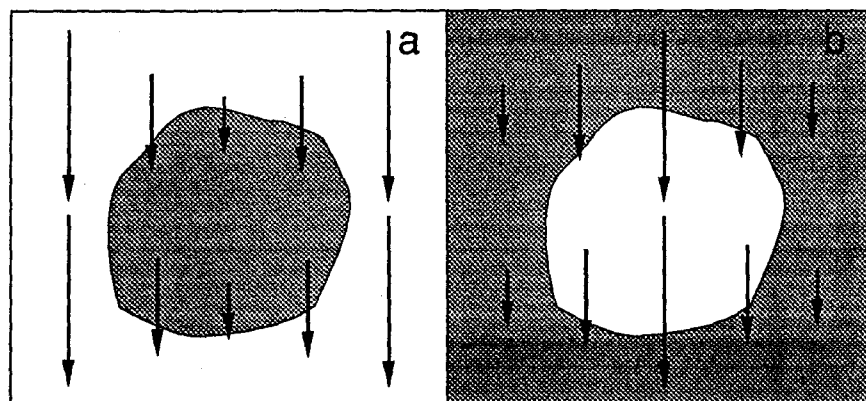
Fig. 4.3: Schematic diagram of temporal evolution of ice flow as a function of basal resistance. Shaded areas represent regions with higher-than-average bottom drag while white areas indicate lower-than-average drag. (a) Low subglacial water pressure in centre of diagram. (b) High subglacial water pressure in centre of diagram.

While this interpretation approach ensures a roughly constant mean basal resistance averaged over the glacier bed, it also allows for spatially and temporally varying bottom drag, as "sticky spots" are created and destroyed in response to changes in bed lubrication. If a ploughmeter was positioned within the "sticky/slippery" patch in Figure 4.3 and another in the surrounding region, we see that the two ploughmeters would respond to the same water pressure forcing in ways that are 180° out-of-phase with respect to each other.

4.4 Quantitative interpretation

Our success in giving a reasonable qualitative explanation for the data of ploughmeters 92PL02 and 92PL05 in conjunction with the subglacial water pressure record from pressure sensor 92P06 inspired a mathematical treatment of flow of ice over a bed

having varying basal resistance. In the following sections we compute the velocity field for the ice immediately above the glacier bed as a function of bottom drag and explore how ploughmeters respond to the creation and destruction of sticky spots. In our model, we treat the bed as a hard, flat surface over which glacier sliding is controlled by a variable drag along the ice–bed interface.

At first glance, there appears to be a paradox because an effective ice viscosity of the order of 10^{13} Pa s compared to our estimated till viscosities of $O(10^{10}$ Pa s$)$ (see Section 2.4.2.1) implies that any shear associated with the glacier motion is confined entirely to the deformable sediment rather than the ice. We therefore have to address the question of how a soft sediment bed can offer resistance to moving ice that is 1000 times as stiff. Clearly, basal drag can be induced by rigid bedrock bumps sticking into the base of a glacier. However, because we do not believe that sticky spots are spatially permanent features at Trapridge Glacier, they are unlikely to be caused by ice in contact with rigid subglacial bedrock. On the other hand, discontinuities or thinning of the deformable layer overlying a rigid substrate can result in enhanced basal resistance which has the potential to vary in space and time. Alternatively, the temporal and spatial variations of sticky spots can be caused by the formation and failure of grain bridges. During shearing of a granular material, grains can become aligned sufficiently coaxial such that the resulting bridges pose significant resistance to shear (Hooke and Iverson, 1995).

4.4.1 Physical model and outline of analysis

Ice is moving with an over-all velocity v_b, the basal sliding velocity, over a flat surface with a variable drag coefficient f. These assumptions contrast with those of standard glacier sliding theories where ice overlies a bedrock surface having a given topography. Sliding is possible because the ice is not frozen to the bed surface. Resistance to sliding is caused by patches of higher-than-average basal drag rather than by topographic

roughness elements that obstruct the motion. The ice responds to the increased drag on the upstream sides of sticky patches by slowing down and diverging laterally to the sides at these points and thereby permitting the ice to move forward; correspondingly, it speeds up and converges behind the sticky spots, in response to the reduced drag on the downstream sides. We describe the relationship between the sliding velocity v_b and the basal shear stress τ_b by the linear sliding law

$$\tau_b = f v_b \qquad (4.1)$$

where f is a drag coefficient. Equation (4.1) is in direct analogy to the approach taken by MacAyeal (1992) in his calculation to infer basal friction from the observed surface velocity pattern of Ice Stream E.

4.4.2 First order perturbation

We consider the drag coefficient f to consist of a spatially constant background component f^0, which could be a function of time, upon which is superimposed a perturbation component f' which varies with time and position across the glacier bed. For a coordinate system in which the glacier rests on a horizontal bed with the x axis directed in the glacier flow direction and the z axis pointed positive upward, we thus write

$$f(x, y, t) = f^0(t) + f'(x, y, t) \qquad (4.2)$$

With this assumption we note that the basal sliding velocity is also the sum of a time-varying background component and a temporally- and spatially-varying perturbation component, *i.e.*,

$$v_b(x, y, 0, t) = v_b^0(t) + v_b'(x, y, 0, t) \qquad (4.3)$$

Substituting Equations (4.2) and (4.3) into the linear sliding law (Equation (4.1)) and ignoring higher-order perturbation terms, yields

$$\tau_b(x, y, 0, t) = [f^0(t) + f'(x, y, t)][v_b^0(t) + v_b'(x, y, 0, t)] \tag{4.4a}$$

$$= f^0(t)v_b^0(t) + v_b^0(t)f'(x, y, t) + f^0(t)v_b'(x, y, 0, t) + \ldots \tag{4.4b}$$

We can split Equation (4.4) into two equations, one that represents linear background sliding,

$$\tau_b^0 = f^0(t)v_b^0(t) \tag{4.5}$$

and one that describes linear sliding due to the perturbation effects,

$$\tau_b'(x, y, 0, t) = v_b^0(t)f'(x, y, t) + f^0(t)v_b'(x, y, 0, t) \tag{4.6}$$

Note that in Equation (4.4) τ_b varies with both time and space but its variations are constrained by the fact that the spatial average $\langle \tau_b(x, y, 0, t) \rangle = \tau_b^0$. Likewise in Equation (4.6) the spatial average of the perturbation stress $\langle \tau_b'(x, y, 0, t) \rangle$ vanishes.

4.4.3 Variations in sliding due to perturbation effects

The ice mass can move forward with a velocity $v_b'(x, y, 0, t)$ provided that lateral motions of the ice allow a continually adjusting accommodation of the ice to changes in basal drag. We examine the case in which ice is assumed to be a linear viscous fluid.

The problem is formulated as follows. For a linear viscous fluid having constant density ρ_I and constant viscosity η and flowing at velocities slow enough that inertial effects can be neglected, the perturbation velocity field $\mathbf{v}'(x, y, z, t)$ satisfies

$$\frac{\partial \mathbf{v}'(x, y, z, t)}{\partial t} = \frac{\eta}{\rho_I} \nabla^2 \mathbf{v}'(x, y, z, t) \tag{4.7}$$

Note that we used η for the dynamic viscosity of ice in contrast to μ which is used to describe the viscous properties of subglacial sediment. Gravitational terms do not appear in Equation (4.7) since perturbation effects are not driven by gravity. In addition, the assumption of a completely flat bed leads to a constant pressure distribution along the ice–bed interface resulting in zero pressure gradients. The flow is incompressible, so that

$$\nabla \cdot \mathbf{v}'(x, y, z, t) = 0 \tag{4.8}$$

We turn to dimensional analysis and begin by defining dimensionless variables as follows: time $t^* = t/t_0$; distance $\mathbf{r}^* = \mathbf{r}/r_0$; velocity $\mathbf{v}'^* = \mathbf{v}'/v'_0$. With these definitions, Equation (4.7) can be written in dimensionless form

$$\frac{\partial \mathbf{v}'^*(x, y, z, t)}{\partial t^*} = \frac{\eta t_0}{\rho_\mathrm{I} r_0^2} \nabla^{2*} \mathbf{v}'^*(x, y, z, t) \tag{4.9}$$

The characteristic values t_0 and r_0 are arbitrary, but a reasonable choice involves a length scale that is representative of the actual physical system. We therefore set the characteristic distance r_0 equal to the thickness of the glacier ice h_I. The manner in which the ice velocity field $\mathbf{v}'(x, y, z, t)$ adjusts to perturbations at the bed is principally determined by the dimensionless factor on the right hand-side of Equation (4.9). We see that the order of magnitude of time t required for a perturbation to propagate through the ice to the glacier surface is given by $\eta t/\rho_\mathrm{I} h_\mathrm{I}^2 = 1$, whence

$$t = \frac{\rho_\mathrm{I} h_\mathrm{I}^2}{\eta} \tag{4.10}$$

i.e., t is proportional to the square of the ice thickness h_I, and inversely proportional to the kinematic viscosity $\nu = \eta/\rho_\mathrm{I}$. Indeed, ν serves as a diffusivity of momentum and as such has dimensions of $\mathrm{m^2\,s^{-1}}$. Substituting $h_\mathrm{I} = 72\,\mathrm{m}$, $\rho_\mathrm{I} = 900\,\mathrm{kg\,m^{-3}}$ and $\eta = 10^{13}\,\mathrm{Pa\,s}$ into Equation (4.10) yields $t = 4.7 \times 10^{-7}\,\mathrm{s}$ and suggests that we can

assume instantaneous adjustment to steady-state conditions throughout the ice. With this quasi-static assumption, Equation (4.7) reduces to

$$\nabla^2 \mathbf{v}'(x, y, z, t) = 0 \tag{4.11}$$

Equations (4.11) and (4.8) are to be solved subject to the conditions (a) that $\mathbf{v}'$ is tangential to the bed surface at $z = 0$, and (b) that the shear stress parallel to the ice surface at $z = h_I$ vanishes.

We follow the treatment used by Kamb (1970) on regelation sliding and solve Equation (4.11) by the Fourier-analytical method. For the perturbation velocity field $\mathbf{v}'(x, y, z, t)$ the Fourier transform pair is given as

$$\widetilde{\mathbf{V}}'(k_x, k_y, z, t) = \int_{-\infty}^{\infty} \int_{-\infty}^{\infty} \mathbf{v}'(x, y, z, t) \exp[-i(k_x x + k_y y)] \, dx dy \tag{4.12}$$

and

$$\mathbf{v}'(x, y, z, t) = \frac{1}{(2\pi)^2} \int_{-\infty}^{\infty} \int_{-\infty}^{\infty} \widetilde{\mathbf{V}}'(k_x, k_y, z, t) \exp[+i(k_x x + k_y y)] \, dk_x dk_y \tag{4.13}$$

where k_x and k_y are the wavenumbers in the x and y directions, respectively. Fourier transformation of Equation (4.11) therefore yields

$$\left(-k^2 + \frac{d^2}{dz^2}\right) \widetilde{\mathbf{V}}'(k_x, k_y, z, t) = 0 \tag{4.14}$$

where $k^2 = k_x^2 + k_y^2$. Equation (4.14) is a second-order linear homogeneous differential equation whose solution is readily obtained as

$$\widetilde{\mathbf{V}}'(k_x, k_y, z, t) = C_1(k_x, k_y, t) \exp(-kz) + C_2(k_x, k_y, t) \exp(+kz) \tag{4.15}$$

Applying the boundary conditions yields expressions for the two constants C_1 and C_2 and Equation (4.15) becomes

$$\widetilde{\mathbf{V}}'(k_x, k_y, z, t) = \frac{\widetilde{\mathbf{V}}'(k_x, k_y, 0, t) \exp(-kz)}{1 + \exp(-2hk)} + \frac{\widetilde{\mathbf{V}}'(k_x, k_y, 0, t) \exp(+kz)}{1 + \exp(+2hk)} \tag{4.16}$$

In order to relate the perturbation velocity field to the perturbation drag coefficient surface we make use of the stress–strain relations for a linear viscous fluid,

$$\sigma_{ij} = 2\eta\dot{\epsilon}_{ij} - \delta_{ij}p \qquad (4.17)$$

where η is the viscosity of the fluid and $\delta_{ij}p$ is the hydrostatic pressure. Substituting the definition of the strain rate tensor

$$\dot{\epsilon}_{ij} = \frac{1}{2}\left(\frac{\partial v_i}{\partial x_j} + \frac{\partial v_j}{\partial x_i}\right) \qquad (4.18)$$

into Equation (4.17) we write for the basal shear stress in the x direction (see Equation (4.6))

$$\tilde{\sigma}'_{xz}(k_x, k_y, 0, t) = \eta\frac{\partial \tilde{V}'_x}{\partial z} \qquad (4.19a)$$

$$= v_x^0(t)\tilde{f}'(k_x, k_y, t) + f^0(t)\tilde{V}'_x(k_x, k_y, 0, t) \qquad (4.19b)$$

We note that $\partial\tilde{V}'_z/\partial x = 0$ since the ice remains everywhere in contact with its flat bed. We now calculate

$$\frac{\partial \tilde{V}'_x}{\partial z} = \frac{\tilde{V}'_x(k_x, k_y, 0, t)k\exp(+kz)}{1 + \exp(+2hk)} - \frac{\tilde{V}'_x(k_x, k_y, 0, t)k\exp(-kz)}{1 + \exp(-2hk)} \qquad (4.20)$$

Substituting Equation (4.20) into Equation (4.19) and re-arranging terms, we solve for the x component of the perturbation velocity field, *i.e.*,

$$\tilde{V}'_x(k_x, k_y, 0, t) = \frac{v_x^0(t)\tilde{f}'(k_x, k_y, t)}{-f^0(t) + \eta\left(\dfrac{k}{1 + \exp(+2hk)} - \dfrac{k}{1 + \exp(-2hk)}\right)} \qquad (4.21)$$

The y component of the perturbation velocity field is now easily obtained by invoking the incompressibility condition (Equation (4.8)),

$$\tilde{V}'_y(k_x, k_y, 0, t) = -\frac{k_x}{k_y}\tilde{V}'_x(k_x, k_y, 0, t) \qquad (4.22)$$

4.4.4 Description of drag coefficient surface

We consider a part of the bed of area A, assumed to be rectangular of dimensions L_x and L_y in the x and y directions. Within this area we now define a drag coefficient surface $f(x, y, t)$ to consist of a spatially-constant background component $f^0(t)$ superimposed by a spatially- and temporally-variable perturbation component $f'(x, y, t)$ with the condition that

$$\langle f'(x, y, t) \rangle = 0 \qquad (4.23)$$

where $\langle \, \rangle$ denotes averaging over A (Fig. 4.4). The perturbation drag coefficient surface is described by blocks that are centred on coordinates $(\bar{x}, \bar{y})$, have widths w_x and w_y in the x and y directions, respectively, and rise f'_+ above zero while the remainder of the surface is depressed by f'_- below zero. The magnitude of f'_- cannot exceed $f^0(t)$ since a negative drag coefficient $f(x, y, t)$ is not physically meaningful. In addition, the magnitudes of f'_+ and f'_- are generally not equal and depend on the areal fraction that is covered by blocks, *e.g.*, narrow blocks with large positive f'_+ values are accompanied by small negative f'_- values for the remainder of the surface.

We suppose the drag coefficient surface $f(x, y, t)$ to be periodically repeated over the entire x-y plane, so that the bed, of assumed infinite extent, consists of a checker-board of identical areas A, across which the ice slides in the x direction. While a real glacier bed is not periodic in this strict sense, our assumption of repeat distances L_x and L_y is a necessary condition for calculating the Fourier transform of the perturbation drag coefficient surface (see Equation (4.21)).
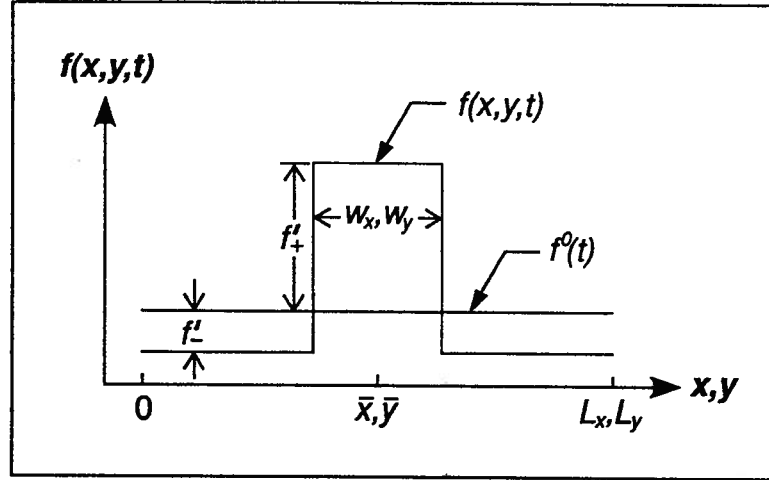
Fig. 4.4: Diagram of drag coefficient surface $f(x, y, t)$ defined on part of glacier bed of area $A = L_x L_y$.

4.4.5 Model results

In Table 4.1 we have listed the model parameter values that were used to obtain the calculated solutions. Glen's flow law for simple shear in the x-y plane

$$\dot{\epsilon}_{xz} = B\sigma_{xz}^n \tag{4.25}$$

combined with Equation (4.17), yields a theoretical estimate of the effective dynamic viscosity of ice

$$\eta = \frac{1}{2B\tau_b^{n-1}} \tag{4.26}$$

where $\sigma_{xz} = \tau_b$ is the basal shear stress. Using a flow law parameter for temperate ice $(B = 6.8 \times 10^{-15}\,\text{s}^{-1}\,\text{kPa}^{-3}$, $n = 3$ (Paterson, 1994, p. 97)) and a mean basal shear stress of $\tau_b = 77\,\text{kPa}$ (based on an ice thickness of 72 m (Blake, 1992)), we calculated a Trapridge Glacier ice viscosity of $\eta = 1.24 \times 10^{13}\,\text{Pa}\,\text{s}$. However, any debris entrained in the ice as well as the process known as enhanced creep due to stress concentrations near the bed are likely to soften this basal ice. We therefore used a dynamic viscosity of

$\eta = 5.0 \times 10^{12}$ Pa s in our model calculations (Table 4.1). With an average basal sliding velocity of $v_b^0 = 40\,\mathrm{mm\,d^{-1}}$ (see Chapter 5) substituted into Equation (4.5) we can calculate a background drag coefficient of $f^0 = 1.66 \times 10^{11}\,\mathrm{Pa\,s\,m^{-1}}$. The remaining parameters in Table 4.1 were determined on a trial and error basis to yield the desired results.

Parameter	Symbol	Value	Units
Effective dynamic ice viscosity	η	5.0×10^{12}	Pa s
Background basal sliding velocity	$v_x^0 = v_b^0$	40	mm d^{-1}
Background drag coefficient	f^0	1.66×10^{11}	Pa s m^{-1}
Peak perturbation drag coefficient	f'_+	2.3×10^{11}	Pa s m^{-1}
Length of area A in x direction	L_x	20	m
Length of area A in y direction	L_y	20	m
Number of grid points in x direction	N_x	32	
Number of grid points in y direction	N_y	32	
Width of blocks in x direction	w_x	7.5	m
Width of blocks in y direction	w_y	7.5	m

Table 4.1: Parameters for "sticky spot" model.

For the model calculations discussed in this section, area A has been divided into a 32×32 grid. Following the description in the previous section, positive f'_+ or negative f'_- values were then assigned to every grid point. The resulting drag coefficient surface $f'(x, y, t)$ was Fourier transformed using a two-dimensional FFT algorithm (Press and others, 1992, p. 515) to obtain $\tilde{f}'(k_x, k_y, t)$. Using Equations (4.21) and (4.22) we can now calculate the perturbation velocity field $\tilde{\mathbf{V}}'(k_x, k_y, 0, t)$ or, after taking the inverse Fourier transform, $\mathbf{v}'(x, y, 0, t)$.

The drag coefficient surface shown in Figure 4.5a consists of square patches with higher-than-average drag centred on grid point (17,17) and the four corners of area A, while the remainder of A has lower-than-average drag. For a peak perturbation drag coefficient $f'_+ = 2.3 \times 10^{11}\,\mathrm{Pa\,s\,m^{-1}}$ for the blocks and using $w_x = w_y = 12$ grid points, we used Equation (4.23) to calculate $f'_- = -0.9 \times 10^{11}\,\mathrm{Pa\,s\,m^{-1}}$ for the remainder of the surface. The resulting flow velocity field (Fig. 4.5b) shows how the ice is being

slowed down and diverted around the high-resistance patch in the centre of area A. Here and in subsequent plots of flow velocity fields, the background sliding velocity v_x^0 has been added to the pertubation velocity field (note that $v_y^0 = 0$). A flat drag surface ($f'_+ = f'_- = 0$, Fig. 4.5c) yields a uniform flow field with velocity $v_b(x, y, 0) = v_b^0 = v_x^0$ (Fig. 4.5d). In Figure 4.5e, the drag coefficient surface consists of a resistance low in the centre of area A with patches of higher-than-average drag located on the midpoints of the sides of the square area. Now the ice is allowed to accelerate and be channelled toward this low-resistance patch (Fig. 4.5f).

Fig. 4.5: Next page: Drag coefficient surfaces, as defined on a 32×32 grid of area A, and calculated ice flow velocity fields. (a) High drag centred on grid point (17,17). (b) Divergent and slowed down ice flow. (c) Flat drag surface. (d) Uniform ice flow. (e) Low drag in the centre of area A. (f) Convergent and accelerated ice flow.
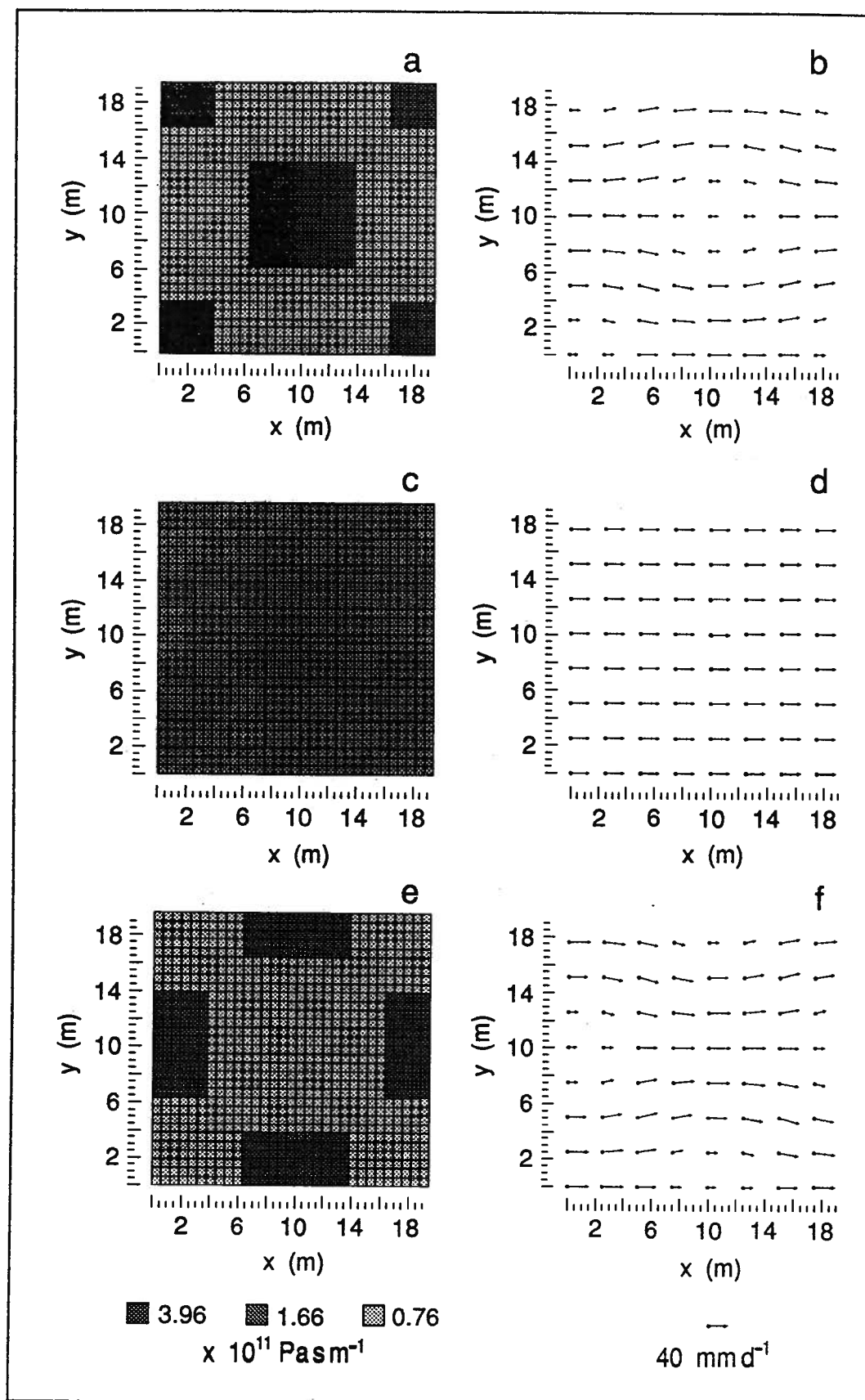
Combining Figures 4.5b, 4.5d and 4.5f (Fig. 4.6), we see that, as the central region of A alternates between being sticky and slippery, some of the flow vectors rotate back and forth and change their lengths. The change in length of a flow vector corresponds to a change in basal sliding velocity of ice at that point while rotation indicates a re-orientation of the ice flow direction. For further analysis, we imagine the consequence of positioning two ploughmeters (here denoted PL1 and PL2) at grid points (7,16) and (23,18) (Fig. 4.6). With the side lengths of area A chosen to be $L_x = L_y = 20\,\mathrm{m}$, the location of these two grid points corresponds to a separation of the two ploughmeters by approximately $10\,\mathrm{m}$ while the line joining the two points forms an angle of $\sim 7°$ with the x direction. This choice of ploughmeter positioning is therefore a good approximation to the field setup (the two insertion sites of ploughmeters 92PL02 and 92PL05 were $\sim 10\,\mathrm{m}$ apart while the line joining the sites was at an angle of $\sim 8°$ from the direction of glacier flow). With our assumption that the force response of a ploughmeter is linearly proportional to the basal sliding rate, we note that the change in length of the flow vectors at the two grid points translates into a change in forcing on ploughmeters PL1 and PL2. In addition, the rotation of the flow vectors is equivalent to an apparent rotation of the ploughmeters about their long axes. We computed idealized force and azimuth responses of ploughmeters PL1 and PL2 for three complete cycles of creating and destroying a sticky spot at the centre of A (Fig. 4.7). Recalling our assumption of a water-pressure-dependent basal resistance, we can associate the cycles with diurnal variations in subglacial water pressure. Figure 4.7 shows that the response of ploughmeters PL1 and PL2 in our model calculations are similar to those of ploughmeters 92PL02 and 92PL05 in the field (Fig. 4.1). The force records (Figs. 4.7a and 4.7b) show strongly anti-correlated responses with diurnal variations of $\sim 30\%$ while the azimuth records (Figs. 4.7c and 4.7d) indicate an apparent in-phase rotation by $15°$. The bends in the computed force responses of both ploughmeters (Figs. 4.7a and 4.7b)

are the result of the drag coefficient f'_+ for positive perturbations not being of equal magnitude to f'_- for negative perturbations.
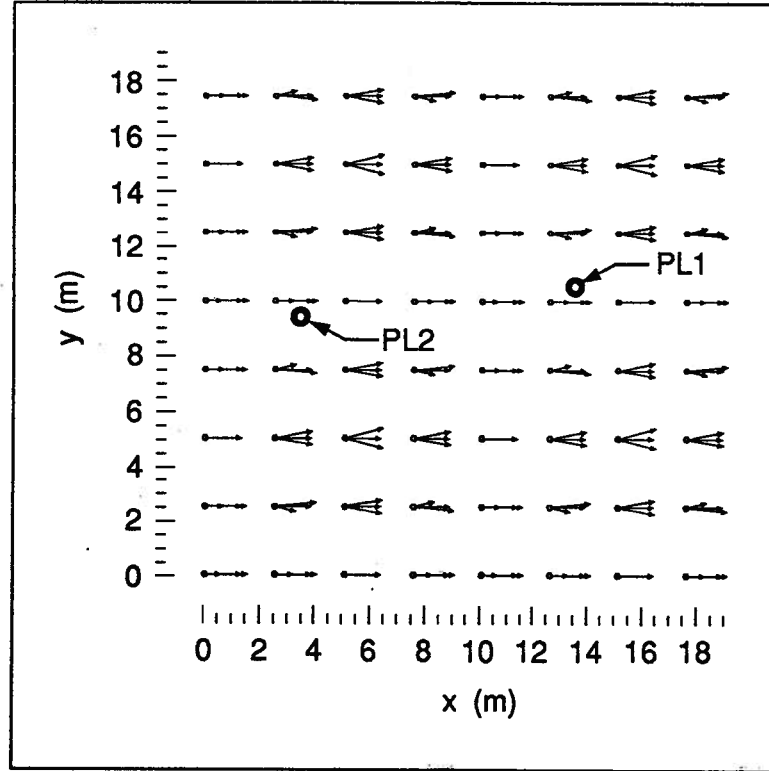
Fig. 4.6: Composite of Figures 4.5b, 4.5d and 4.5f showing the change in ice flow velocity field. The locations of the numerical ploughmeters PL1 positioned at grid point (7,16) and PL2 at (23,18) are indicated.

We further demonstrate the qualitative success of our model calculations by computing the force and azimuth responses of ploughmeters PL1 and PL2 for a varying basal drag that is based on the water pressure record shown in Figure 4.1e. In our calculations, low subglacial water pressures correspond to high resistance in the centre of area A. The computed results (Fig. 4.8) display a striking similarity to the field data shown in Figure 4.1: the force records (Figs. 4.8a and 4.8c) indicate ~30% variations that are 180° out-of-phase with each other while the azimuth records (Figs 4.8b and 4.8d) show an in-phase rotation by roughly 10–15°.

Fig. 4.7: Idealized responses of two numerical ploughmeters over three cycles of creating and destroying a sticky spot on the centre of area A. (a) Synthetically generated force record for ploughmeter PL1. (b) Synthetically generated force record for ploughmeter PL2. (c) Synthetically generated azimuth record for ploughmeter PL1. (d) Synthetically generated azimuth record for ploughmeter PL2.

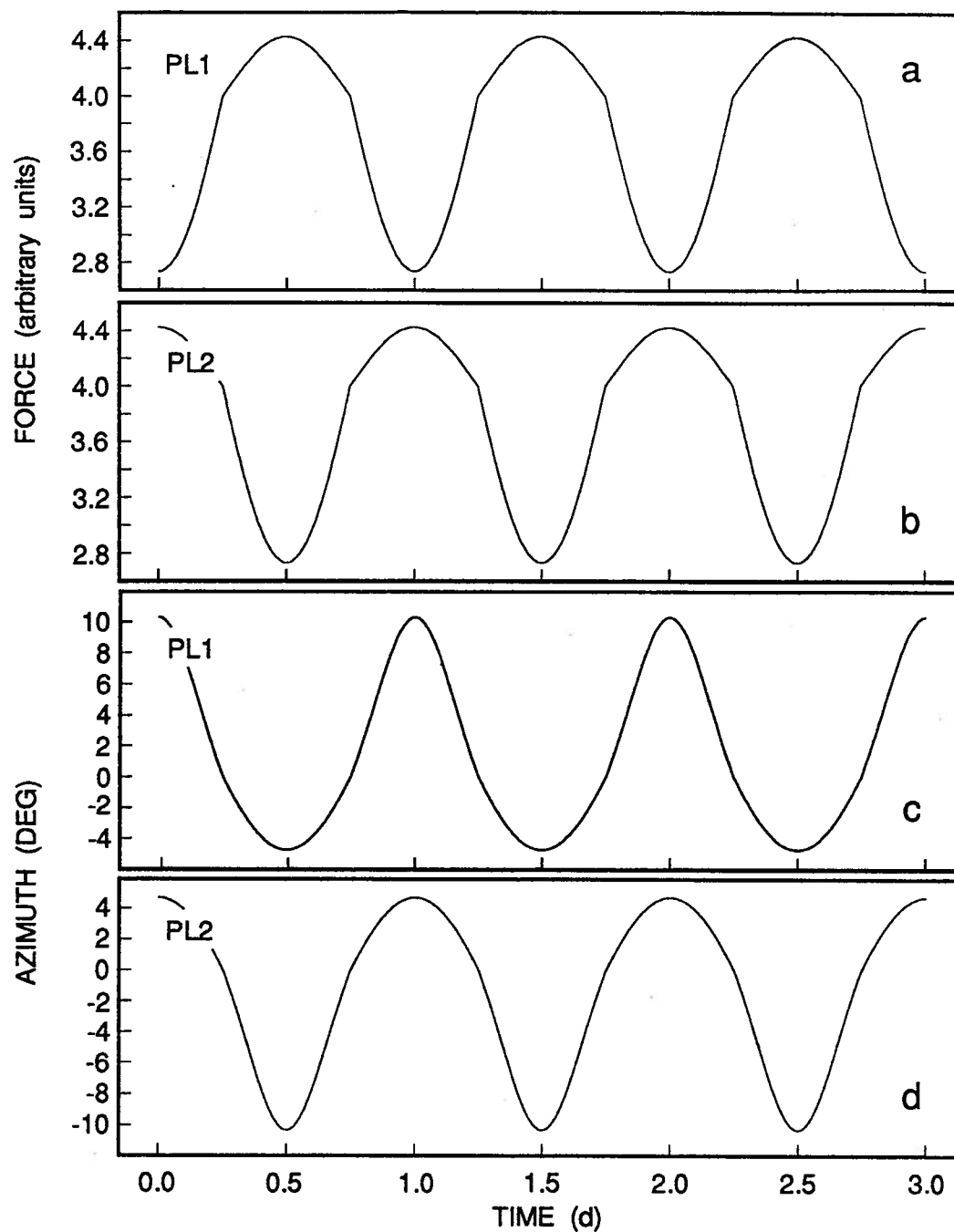## 4.5 Concluding discussion

Our model calculations for the flow of ice over a flat surface with variable resistance are based on the approximation that ice behaves as a linear viscous fluid. The purpose of the model is to demonstrate how local values of shear stress might vary with time and space. The nonlinearity of Glen's flow law would greatly complicate the model without contributing additional insight.

In our derivation of Equation (4.6) that describes sliding due to temporally- and spatially-varying perturbations in drag coefficient, we neglected higher-order perturbation terms (see Equation (4.4)), thereby linearizing the problem by ignoring non-linear effects. This is a reasonable approximation as long as perturbations of the drag coefficient are small compared to the background drag coefficient. However, from Table 4.1 we see that the coefficients for background drag and perturbation drag have values that are of the same order of magnitude. Nevertheless, a more rigorous calculation using Equation (4.6) which would include non-linear terms could not be justified in light of the other simplifications used in our model, *i.e.*, linear ice rheology and a very simplified sliding law (Equation (4.1)). Therefore, for our purpose of only demonstrating that we can explain our field observations in terms of changes of basal resistance in response to fluctuations of subglacial water pressure, we feel confident about our decision to ignore non-linear effects in Equation (4.4).

The results from our model calculations point to the existence of sticky spots beneath Trapridge Glacier. Although we have only demonstrated consistency for a single example, it is conceivable that there are sticky spots all across the bed of our main study region. These sites of enhanced basal drag are ephemeral in nature because they are created and destroyed in response to fluctuations in subglacial water pressure. Therefore, it is unlikely that they support a large fraction of the driving stress for ice flow. Our previous result, that the deformational resistance of the sedimentary bed is of comparable magnitude to that required to balance the applied basal shear stress
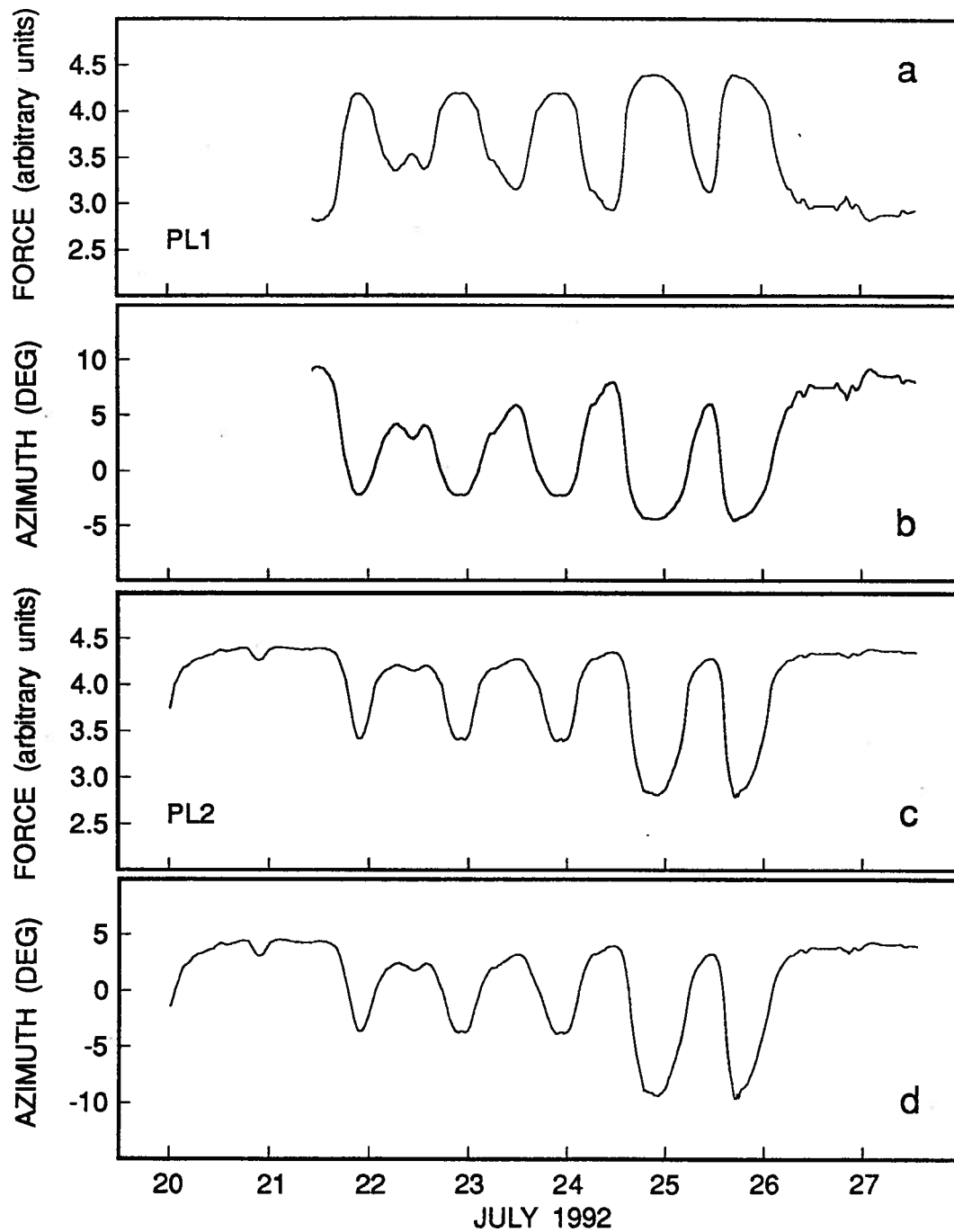
Fig. 4.8: Computed responses of two numerical ploughmeters for a varying basal drag that is based on the water pressure record shown in Figure 4.1e. (a) Synthetically generated force record for ploughmeter PL1. (b) Synthetically generated azimuth records for ploughmeter PL1. (c) Synthetically generated force record for ploughmeter PL2. (d) Synthetically generated azimuth records for ploughmeter PL2. Note the similarity to Figures 4.1a–4.1d.

(see Chapter 2), further strengthens our argument that sticky spots are probably not dominant in controlling the flow of Trapridge Glacier.

Our findings can be compared with results from Ice Stream B. Interpretation of data collected near the Upstream B camp (Alley, 1993) suggests that the lubricated regions of the bed support more than 87% of the basal shear force. This leaves <13% of the basal shear force to be supported on sticky spots implying that sticky spots do not dominate the force balance in this region of Ice Stream B. In contrast to our results, Whillans and others (1989) reported that Byrd Glacier, Antarctica, is held mainly by basal drag that is concentrated at a few sites separated by about 13 km. Analysis of work done on Ice Stream C (Anandakrishnan and Alley, 1994; Alley and others, 1993) indicated that the base of the ice stream consists of a weak till interspersed with sticky spots of area on the order of $10^2 \, \text{m}^2$ with a spatial density on the order of $10 \, \text{km}^{-2}$. As a result of a reduced water lubrication, it is claimed that these sticky spots support almost all of the driving stress and account for the negligible flow of Ice Stream C.

This chapter concludes our examination of ploughmeters as an instrument for studying mechanical conditions and processes at the base of the glacier. However, the analysis of data from this type of device cannot be complete without some means of measuring sliding. In Chapter 5, we present a newly developed method to measure *in situ* basal sliding, and we discuss some results from our measurements beneath Trapridge Glacier.

Chapter 5

DIRECT MEASUREMENT OF SLIDING AT THE GLACIER BED

"It would be more impressive if it flowed the other way."

- Oscar Wilde

5.1 Introduction

Mechanical measurements of sliding over a deforming substrate are rare. Boulton and Hindmarsh (1987) screwed an auger-like anchor into the sediment beneath the terminus of Breidamerkurjökull in Iceland. The anchor was inserted through a sealed hole in the floor of an englacial tunnel and connected by a string to a reel and chart recorder. As the glacier sole moved relative to the underlying sediment, the string was pulled over the reel and ice displacement recorded. Engelhardt and others (1990b) used the same principle and anchored a tethered stake in till beneath Ice Stream B. By observing the pull-in of the tether cable, they inferred a sliding rate high enough to account for the total motion of the ice stream.

In an effort to measure basal sliding of Trapridge Glacier, we have developed an instrument which is similar to the Boulton and Hindmarsh design in that an anchor is placed in the deformable bed and the amount of string payed out is measured. Our instrument can be installed *in situ* at the bottom of deep, narrow boreholes and has been termed a "drag spool". The device consists of a multi-turn potentiometer connected to a spooled string. The drag spool is suspended within the borehole close to the glacier bed, and continuously measures the length of string payed out to an anchor in the bed. In this chapter, we describe the physical characteristics and field operation of this device. We also present and discuss some results from our measurements beneath Trapridge Glacier.

5.2 Methods

The basic components of a drag spool are an anchor, a multi-turn potentiometer, and a spooled string (Fig. 5.1). A thin nylon string is wound onto a 3.0 cm diameter spool. A 25-turn 5 kΩ potentiometer (Bourns, part No. 3296W-1-502) is connected to the spool so that turns of the spool can be measured electrically from the glacier surface. The spool–potentiometer assembly is enclosed in an acrylic casing. To prevent water that enters the case from shorting out the potentiometer leads, the interior of the spool is filled with an electrically insulating grease. The free end of the string is led through a small hole that penetrates the case and then attached to a conical anchor tip. A percussion hammer (Blake and others, 1992), fitted with a 0.635 cm diameter metal-dowel attachment, is used to insert the anchor into the soft glacier bed. The dowel fits into a 0.635 cm diameter socket drilled into the back of the anchor tip. The dowel passes through loose-fitting loops on the drag-spool casing. After the anchor is inserted, the hammer and dowel are withdrawn, leaving the anchor and the drag-spool case at the bottom of the borehole. Although the hammer and the wire rope supporting it are drawn past the drag-spool cable, we have not had any problem with ropes and cables becoming entangled. Additionally, the dead weight of the drag-spool cable appears to exceed the frictional force between wire and cable; we have not observed any unwinding of the drag-spool string, which would indicate that the spool is being pulled, as the hammer is lifted. Once the hammer has been withdrawn, slack is removed from the drag-spool cable until a slight tension is sensed. Even though the force required to unwind the drag spool is only 1 N, it is possible to feel this tension point in the 70–80 m long cable that we use on Trapridge Glacier. Nevertheless, a few centimetres of string are usually pulled off the spool. As the cable freezes into the borehole, the position of the drag-spool case within the borehole becomes fixed. In response to glacier sliding, the anchor will distance itself from the glacier borehole and the spool will turn as the

string is payed out. Appoximately 2.5 m of thin nylon string are stored on the spool, which is enough to last for 3–5 weeks at the anticipated sliding rates.
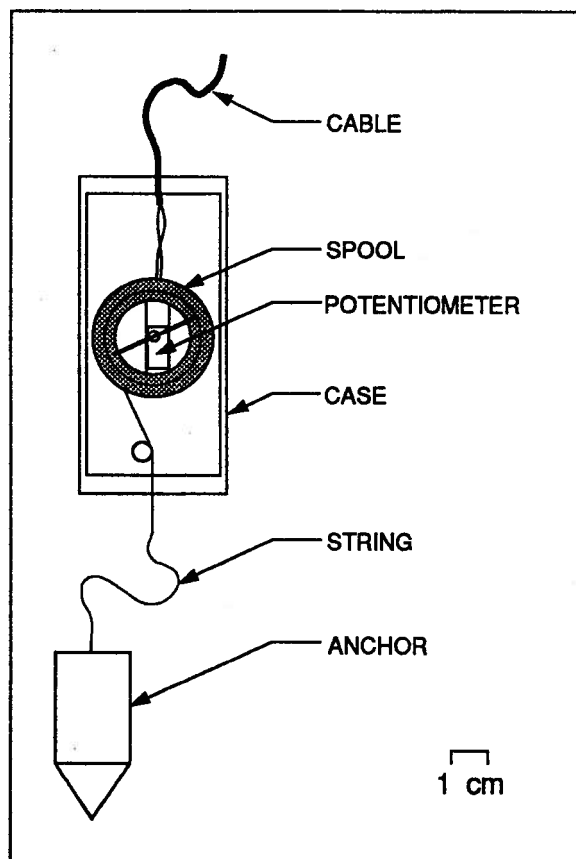
Fig. 5.1: Schematic diagram of the drag spool. As the string attached to the anchor is payed out, the potentiometer screw is turned and the resistance change can be measured.

5.3 Results and discussion

Figure 5.2 shows an example of data obtained from a drag spool during the 1992 field season on Trapridge Glacier. The data (Fig. 5.2a) indicate that the distance between anchor and drag-spool case increased by approximately 260 mm during the interval 21–27 July. This increase translates into an average rate of string-extension of roughly

$43\,\mathrm{mm\,d^{-1}}$. The displacement record (solid line in Fig. 5.2a) shows distinct diurnal deviations from the general trend of increase (dashed line in Fig. 5.2a). Strong diurnal fluctuations in subglacial water pressure (Fig. 5.2b) were contemporaneously observed in a borehole located approximately 12 m up-flow from drag spool 92SM02 and appear to be correlated with the variations in the displacement record. We now present two alternative interpretations in an attempt to explain the available data.

The stepwise increase in displacement seen in the drag-spool data (Fig. 5.2a) could indicate an increase in sliding velocity in response to a rise in subglacial water pressure. The idea of high sliding velocities resulting from smoothing of bed roughnesses by accumulation of pressurized water between ice and bed has been proposed by Weertman (1964) and further analyzed by Lliboutry (1979). We computed the sliding velocity (rate of displacement; Fig. 5.2c) by applying a five-point first-derivative filter to the displacement record (Abramowitz and Stegun, 1965, p. 914), followed by a Gaussian smoothing filter having a standard deviation of 100 min. Comparison of Figure 5.2b and 5.2c shows that peak displacement rates coincide with rises in water pressure. This result contrasts with observations by Iken and Bindschadler (1986), Kamb and others (1985), Kamb and Engelhardt (1987) and Hooke and others (1989) where peak subglacial water pressure and peak surface velocity (and by implication basal sliding velocity) appear to coincide.

Alternatively, the stepwise increase in displacement could be interpreted in terms of the growth of water-filled cavities at the glacier bed as a function of subglacial water pressure. As cavities grow, the glacier is separated from its bed, which results in an increase in distance between the anchor and the drag-spool case. The concept of growing and shrinking cavities at the ice–bed interface has been introduced into glacier sliding theories (Lliboutry, 1968; Kamb, 1970; Iken, 1981) to allow for the varying extents to which a glacier is separated from its bed. Field observations on Variegated Glacier in Alaska (Kamb and others, 1985; Kamb and Engelhardt, 1987)
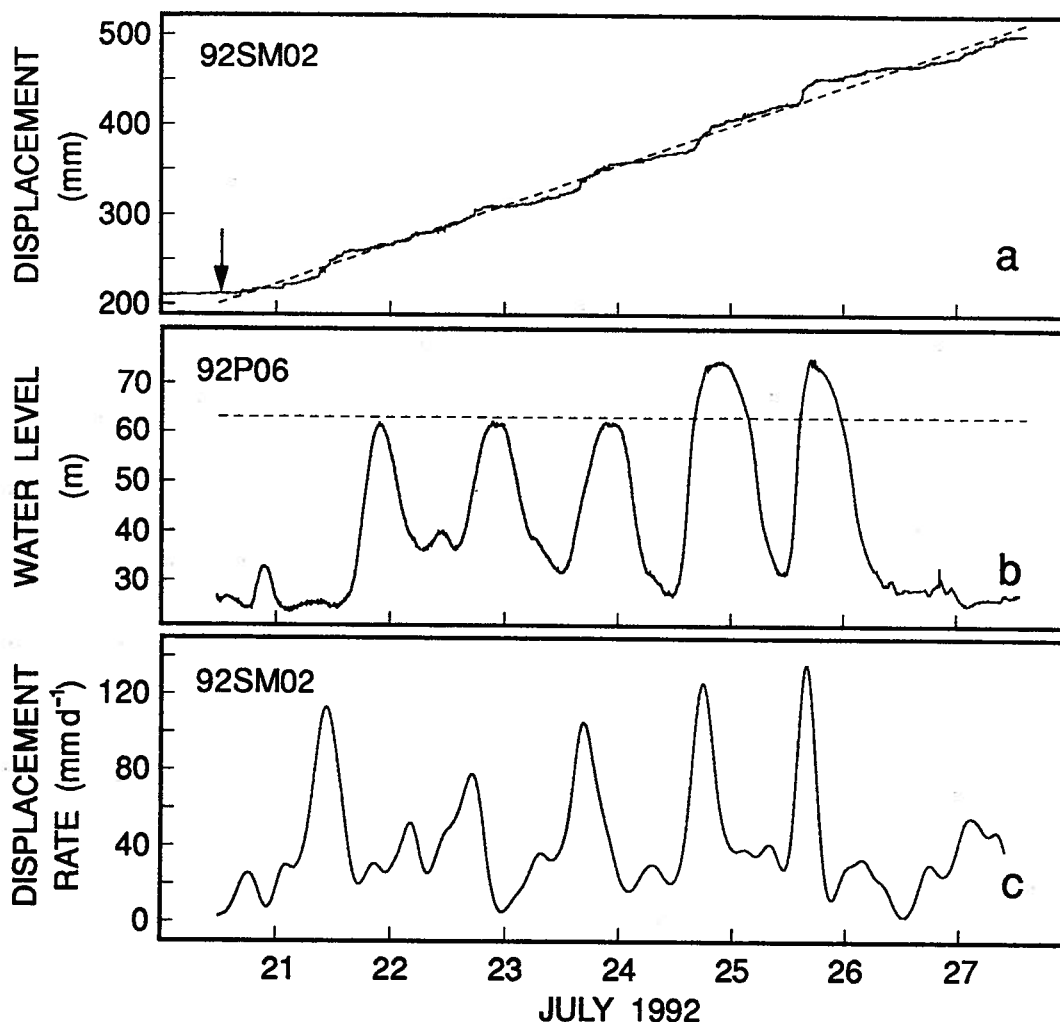
Fig. 5.2: Data from drag spool 92SM02 and pressure sensor 92P06 (see text for details). (a) General increasing trend (dashed line) obtained by linear regression, superimposed on the relative displacement between anchor and drag-spool case (solid line). The arrow indicates the time when the spool started to turn. (b) Subglacial water pressure record. Flotation pressure corresponds to a water level of roughly 63 m (dashed line). (c) Rate of displacement between anchor and drag-spool case, obtained by numerical differentiation of the displacement record.

and on two glaciers in the Swiss Alps — Unteraargletscher (Iken and others, 1983) and Findelengletscher (Iken and Bindschadler, 1986) — support the idea that glacier uplift is mainly due to basal cavitation driven by high basal-water pressures. We computed

the corresponding vertical uplift for Trapridge Glacier from the general displacement trend (dashed line in Fig. 5.2a) and the actual displacement record. The dashed line was obtained by fitting a regression line to the data from the time the spool started to turn (see arrow in Fig. 5.2a) until the end of the record. To consider trigonometric effects, we used two different models of drag-spool operation which represent end-members of a spectrum of possibilities (Fig. 5.3). In the first scenario the nylon string is free to move laterally through the soft sediment (Model A), while in the second the sediment is stiff enough to prevent the string from cutting through it (Model B). We expect that the position of the string is closer to Model B, since the tension required to unwind the spool is small (about 1 N); we do not believe that this tension is sufficient to allow the string to cut easily through the basal material. The exact depth of emplacement of the anchor in the basal sediment is uncertain. However, based on our experience with inserting other instruments using the same procedure (Blake and others, 1992; Chapter 2), we are able to reasonably constrain this uncertainty. For our calculations in this chapter we assume an insertion depth of the anchor of $18 \pm 3\,\text{cm}$.
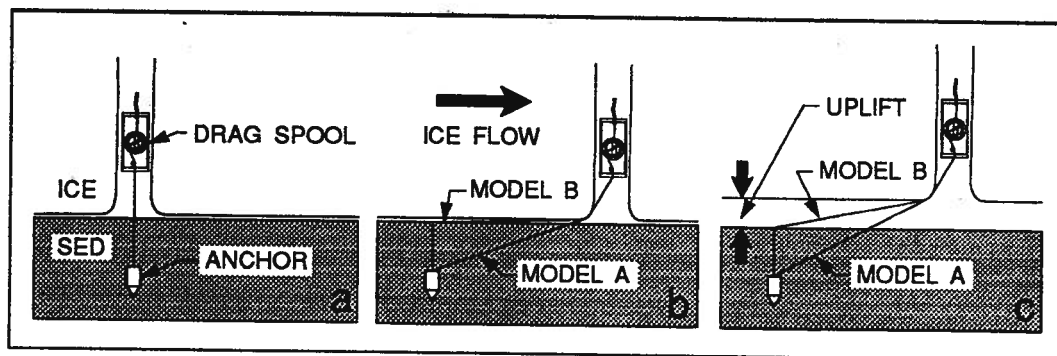

Fig. 5.3: Scenarios for drag-spool operation. Model A allows for lateral movement of the string through soft sediment. The sediment in Model B is sufficiently stiff to keep the string in place. (a) Situation immediately after installation of the device at the glacier bed. (SED indicates sediment) (b) Situation after some time has elapsed. (c) Same as (b) with vertical glacier uplift.

Model A requires a bed separation of 8 cm and Model B one of up to 20 cm to explain the available data. Daily surveying of marker poles on the glacier surface did not reveal vertical displacements of this magnitude. We therefore think that both models predict a vertical glacier uplift that is inconceivably high for Trapridge Glacier. However, we cannot completely dismiss the possibility of fluctuating bed separation. If increases in subglacial water pressures coincide with the growth of water-filled cavities at the glacier bed, then our field observations may correspond to model results by Iken (1981) that the largest sliding velocity occurs during cavity growth and not when the steady-state size of cavitation is attained. This interpretation agrees with observations at Unteraargletscher (Iken and others; 1983) that the highest horizontal velocity occurred when the rate of upward motion of the ice was largest rather than at the time when the uplift reached its maximum. From the foregoing discussion, we conclude that the diurnal character of the data recorded with drag spool 92SM02 (Fig. 5.2a) is mostly a result of variable sliding velocity. Unfortunately, we cannot settle this question using our current survey methodologies. We would require a survey accuracy of ± 10 mm to resolve diurnal fluctuations in Trapridge Glacier flow.

During the 1992 field season, the surface velocity of Trapridge Glacier at our study site was about 80 mm d^{-1}. Observations of lateral deformation of boreholes reveal that the velocity contribution from internal ice creep for this glacier does not exceed 10 mm d^{-1} (Blake, 1992). Therefore, almost the entire surface motion of the glacier is attributable to sliding and deformation processes at the bed. Our estimate of $\sim$40 mm d^{-1} for glacier sliding leaves roughly 30–40 mm d^{-1} of motion to be accounted for by subglacial sediment deformation beneath the anchor.

It should be noted that in the previous paragraph we have defined "sliding" in an operational manner, as the motion that occurs between the spool suspended in the borehole and the anchor in the sediment. However, glacier sliding is commonly defined as the motion between the base of the ice and the top of the bed. We recognize that

the two definitions are not equivalent and that measurements taken with a drag spool will place only an upper limit on glacier sliding because the anchor is placed within deformable sediment; any deformation of the sediment lying between the anchor and the ice–sediment contact will introduce additional string-extension. With an anchor insertion depth of $\sim$18 cm, a typical thickness of the deforming sediment layer of $\sim$0.5 m (Blake and Clarke, 1989) and the assumption that the sediment velocity varies linearly with depth, about 5–10% of the measured displacement is due to sediment deformation. This proportion can increase significantly for a velocity–depth profile that is concave-down (Boulton and Hindmarsh, 1987), and thus a large fraction of the ice motion occurs by bed deformation. Alternatively, if the anchor is being pulled through the sediment by tension on the string, all the motion observed at the glacier surface could be due to basal sliding. We do not believe that this is the case, since the tension required to unwind the spool is small ($\sim$1 N). In other instrument-insertion experiments using similar-sized anchors, the force required to dislodge a freshly inserted anchor was at least 20 N, so it appears that the bed has a good grip on the anchor.

Figure 5.4 shows drag-spool data from three consecutive field seasons. The results from our 1990 measurements indicate different displacement rates for different points across the glacier bed, ranging between $\sim$40 mm d^{-1} (traces 90b and 90c) and $\sim$80 mm d^{-1} (trace 90a). This finding is not paradoxical, since we expect mechanical coupling to vary with location because of spatial differences in the subglacial water system. With uniform surface motion observed over large parts of the glacier, our results imply a spatially varying partitioning between basal sliding and subglacial sediment deformation. In addition, changes in displacement rate that we observe from year to year (Fig. 5.4) probably reflect temporal variations of mechanical ice–bed coupling in response to changes in the subglacial hydrological system. As an alternative, we cannot ignore the possibility that different depths to which anchors of different instruments

are inserted, can account for differences in measured displacement rates. From inspection of Table 5.1, we see that for the 1990 measurements, low displacement rates are indicated for drag spools that have their anchors inserted quite deeply while a shallow insertion depth corresponds to a high displacement rate. This finding is inconsistent with what would be expected if sediment deformation contributes significantly to the displacement as measured with a drag spool. The 1991 observations are inconclusive in that respect because two instruments with their anchors inserted to almost the same depth measured rates that are different by 50%. For the 1992 measurements, our findings are opposite to those from 1990 but are consistent with the postulate that high displacement rates correspond to deep anchor insertion depths and *vice versa*. Because of these differences in results from one year to the next we conclude that there appears to be no clear correlation between insertion depth and displacement rate.

Sensor ID (see Fig. 5.4)	Insertion depth (cm)	Displacement rate (mm d^{-1})
90a	19 ± 3	$\sim$80
90c	24 ± 3	$\sim$40
90b	25 ± 3	$\sim$40
91b	20 ± 3	$\sim$40
91a	21 ± 3	$\sim$60
92b	18 ± 3	$\sim$40
92a	23 ± 3	$\sim$60

Table 5.1: Anchor insertion depths and average displacement rates for drag spools used from 1990–92 (see Fig. 5.4).
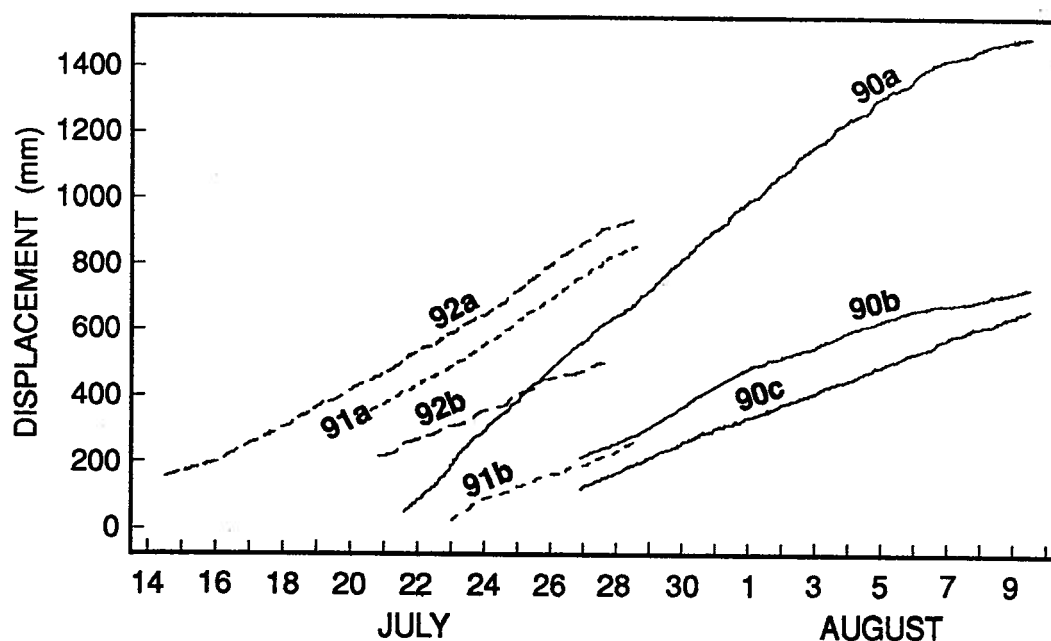
Fig. 5.4: Drag-spool data from the 1990 (solid lines), 1991 (short dashed lines), and 1992 field seasons (long dashed lines), showing the variability of basal sliding observed at Trapridge Glacier. Measured sliding rates range between $\sim$40 mm d^{-1} (traces 90b, 90c, 91b, 92b) and $\sim$80 mm d^{-1} (trace 90a); ($\sim$60 mm d^{-1} for traces 91a and 92a). Trace 92b shows the data from drag spool 92SM02, which is discussed in detail in the text (see also Fig. 5.2a).

5.4 Water pressure induced variations in glacier sliding

The apparent 90° phase shift between water pressure and sliding rate (see Fig. 5.2) is a noteworthy feature of the data. In the previous section, we suggested that a viable interpretation of this feature corresponds to the numerical results by Iken (1981) that maximum horizontal velocities coincide with times when basal water-filled cavities are growing. Unfortunately, the heavy smoothing required to clarify the velocity record (Fig. 5.2c) masks finer detail that might illuminate the motion mechanism. The unsmoothed displacement rate record (Fig. 5.5a) suggests the idea that a localized stick–slip relaxation process is at work. As water pressure rises (Fig. 5.5b), a local strain build-up in the ice is released and the sliding rate increases momentarily; this

small rapid motion produces δ-function-like spikes in the velocity record as shown in Figure 5.5a. Once the finite relaxation has occurred, further rises in water pressure do not produce additional enhancement of basal sliding.

On a cautionary note, the δ-function like pulses in sliding velocity (Fig. 5.5a) would be indistinguishable from stick–slip behaviour of the drag spool, a possibility that we cannot ignore. Such behaviour of our instrument might result from the physical setup during operation; a "sticky" spool being suspended by an "elastic" cable. However, the small force (~ 1 N) required to unwind the spool is not sufficient to significantly stretch the drag-spool cable. We therefore believe that stick–slip behaviour of the instrument is unlikely to be the cause of the spikes in the velocity record.
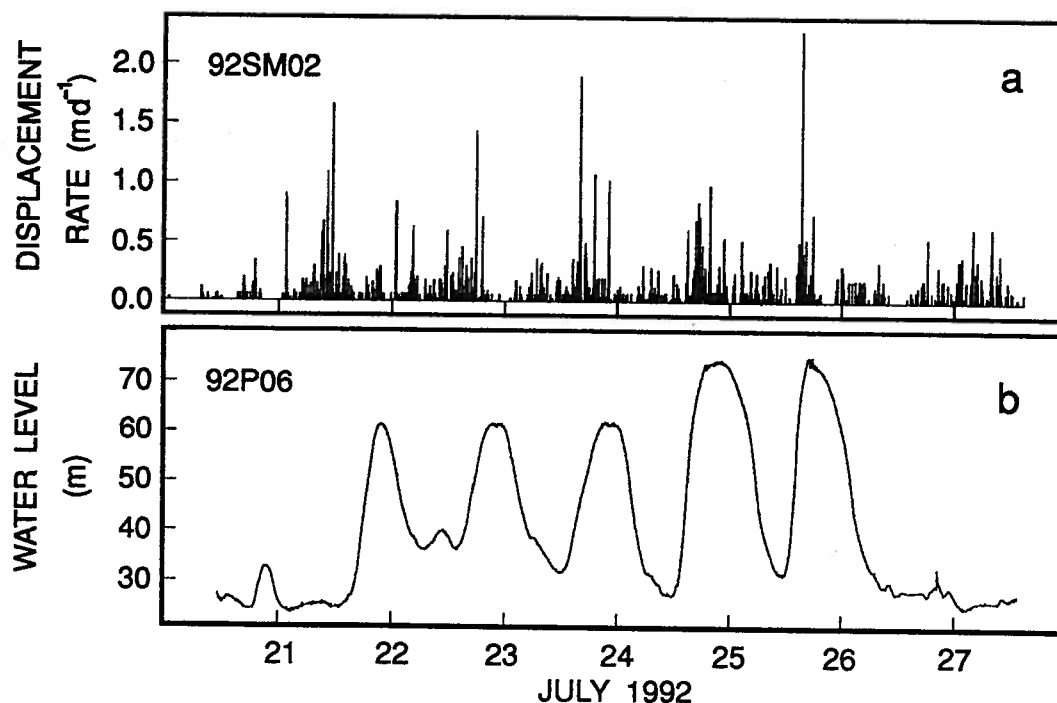

Fig. 5.5: (a) Unsmoothed record of displacement rate between anchor and drag-spool case for drag spool 92SM02, obtained by numerical differentiation of the displacement record shown in Figure 5.2a. (b) Subglacial water pressure record of pressure sensor 92P06 (same as in Fig. 5.2b).

5.4.1 Slider-block model

A simple model for stick–slip behaviour is a slider block pulled by a spring as illustrated in Figure 5.6. Slider-block models have been used to simulate fault behaviour, fore-shocks, aftershocks, and pre- and post-seismic slip, and to explain earthquake statistics (Burridge and Knopoff, 1967; Dieterich, 1972; Rundle and Jackson, 1977; Cohen, 1977; Cao and Aki, 1984, 1986). The block is constrained to move horizontally along a plane surface. It interacts with the surface through friction, which prevents sliding of the block until a critical value of the pulling force is reached. The block sticks and the force in the spring increases until it equals the frictional resistance to sliding on the surface; then slip occurs. The extension of the spring is analogous to elastic strain in rock adjacent to a fault. The slip is analogous to an earthquake on a fault. The stored elastic strain in the spring is relieved in analogy to the elastic rebound on a fault.
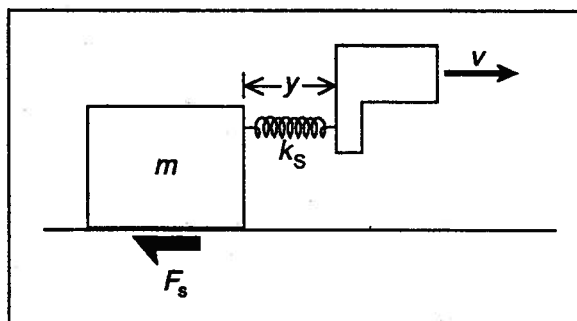
Fig. 5.6: Illustration of the slider-block model for fault behaviour. The constant velocity driver extends the spring until the pulling force $k_s y$ exceeds the static friction force F_s. A similar model has been used in this study.

Because the stick–slip relaxation process postulated for the glacier bed resembles the behaviour of a fault, we attempted to model glacier sliding using a slider block similar to that shown in Figure 5.6. The extension in the spring is analogous to the build-up of elastic strain in the ice and the slip corresponds to the momentary enhancement of basal sliding.

A quantitative study of the behaviour of this simple spring–block model immediately reveals that the periodicity of the stick–slip events depends solely on parameters that are inherent to the system, *i.e.*, the mass of the block, the spring constant and the ratio of static to dynamic friction. In contrast, the stick–slip events observed with drag spool 92SM02 (Fig. 52a) appear to be forced by diurnal subglacial water pressure fluctuations (Fig. 5.2b). In addition, the displacement record (Fig. 5.2a) indicates that after an enhanced sliding event the ice flow slows down to roughly half the average sliding rate rather than coming to a complete stop. For these reasons, the spring–block model as presented above is not suitable for simulating the stick–slip relaxation process which might operate at the bed of a glacier. The analogy between a glacier and a spring attached to a block lacks precision. We therefore seek a more physically based model in which we can choose model parameter values that approximate more closely conditions on real glaciers.

5.4.2 Elastic block model

In the following sections we compute the motion of ice that is purely elastic and slides over a flat surface with a basal resistance that varies in response to fluctuating subglacial water pressures. We begin by looking at our visualization of the bed beneath Trapridge Glacier.

5.4.2.1 Ice–bed contact

Murray and Clarke (1995) described the ice–bed contact beneath Trapridge Glacier as a thin macroporous horizon, a layer consisting of granule- and pebble-sized clasts between the glacier ice and the underlying matrix-rich sediments. Depending on local conditions the intergranular pore space in this horizon is occupied by water or ice. As a result, we can identify at least two distinct components of the subglacial water system,

which we refer to as the connected and unconnected water systems. Meltwater that reaches the bed through crevasses or moulins from the glacier surface or water that originates at the bed by melting due to frictional or geothermal heat is evacuated from the glacier bed through the connected water system. We visualize this water as flowing through the pore space of the macroporous horizon in a drainage configuration that consists of patches connected by a channelized system (Fig. 5.7). The remainder of the glacier bed is covered by the unconnected water system. Here, the ice penetrates into the pore space of the horizon, possibly interspersed with isolated pockets of water which is not in communication with other free water in the subglacial water system. With the two components of the subglacial water system, we effectively divide the glacier bed into two regions. Let α be the fractional area of bed which is covered by the connected system. We shall refer to this part of the bed as region A. Consequently, the area fraction of the bed which is covered by the unconnected system, refered to as region B, is $1 - \alpha$. Despite our belief that the areal coverage of the connected region can increase as rising water pressures cause local uplift of ice in the vicinity of a connected water channel, we assume α to be constant in the following analysis.

5.4.2.2 Description of model

Modeling ice flow over a complex glacier bed such as the one shown in Figure 5.7 is beyond the scope of this thesis. Instead, we take a simplified approach and represent the glacier/substrate interaction by a system consisting of three ice blocks and three substrate blocks (Fig. 5.8a). Block A_I represents the parts of the glacier that slide over the connected region of the bed with area fraction α while block B_I represents all the ice that slides over the unconnected region of the bed with area fraction $1 - \alpha$. At the top, block A_I and block B_I are attached to block C_I. In this way the two blocks are coupled to each other, but otherwise are allowed to deform and thus move independently. We
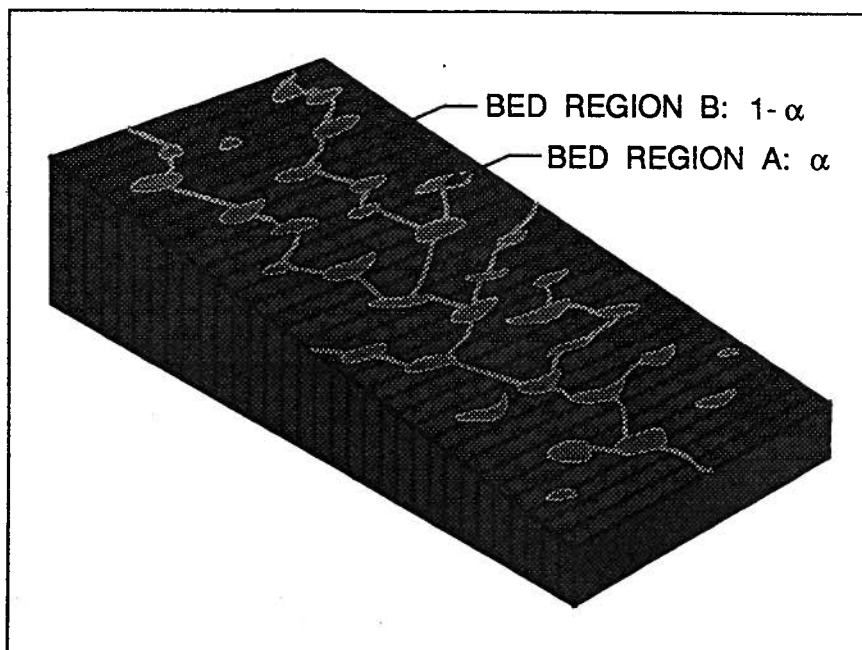
Fig. 5.7: Conceptual diagram of our image of the ice–bed contact beneath Trapridge Glacier. Bed region A is covered by the connected water system while bed region B is covered by the unconnected water system. The fractional areas of these two regions are α and $1 - \alpha$.

can view blocks A_I and B_I as being hinged to block C_I. The height of block A_I and block B_I represents what we call the "strain equilibration distance". This is the distance above the bed at which strain differences within the glacier disappear and all the ice moves at the same rate. Below the ice–bed interface, the ice blocks are opposed by a similar system of substrate blocks A_S, B_S and C_S.

We first consider the basal water pressure to be low in the connected region of the glacier bed. In terms of our block model, a poorly lubricated ice–bed interface implies a high resistance to sliding for block A_I because there is a strong coupling between blocks A_I and A_S. As a result the two blocks start to deform under the applied shear stress imposed by block B_I, which continues to slide (Fig. 5.8b). When subglacial water pressure rises in the connected region, block A_I becomes decoupled
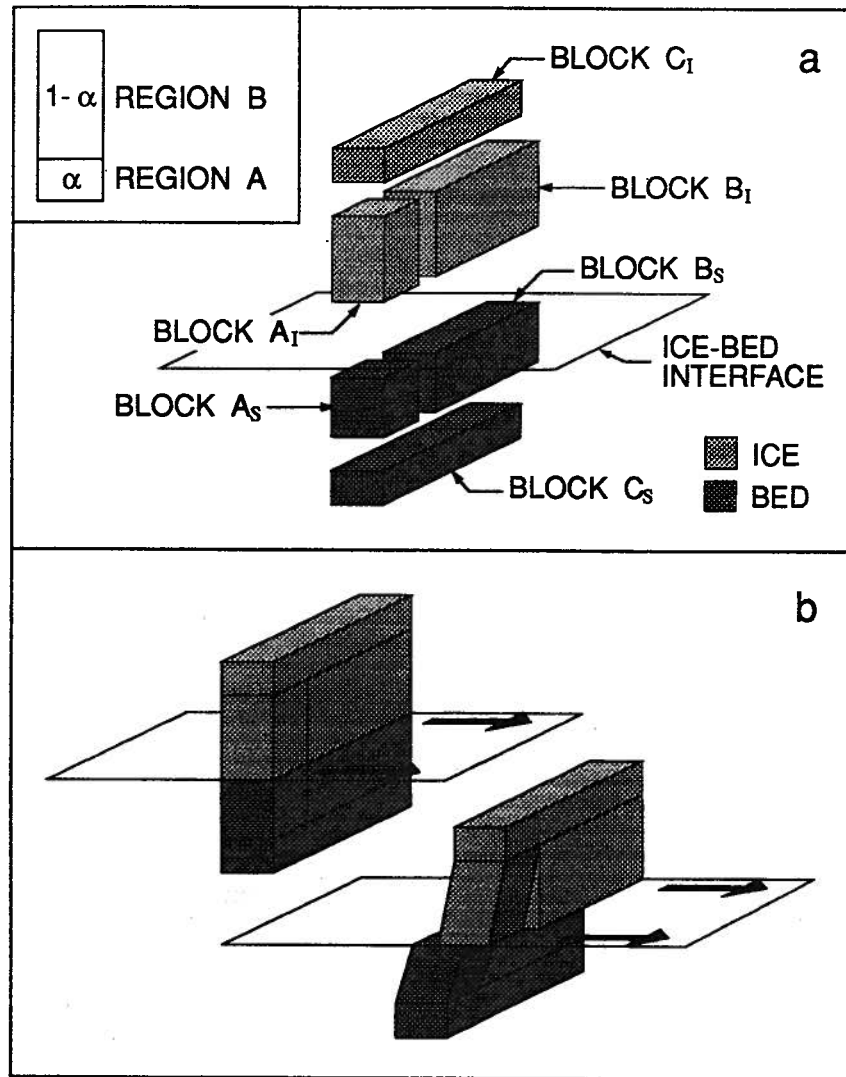
Fig. 5.8: Conceptual diagram of the elastic block model. (a) Building blocks of the model consisting of a system of three ice blocks and a similar system of three substrate blocks separated by the ice–bed interface. Inset shows a plan view indicating the area fractions that represent the connected and unconnected regions of glacier bed. (b) Behaviour of blocks as the glacier slides along the ice–bed interface. Subglacial water pressure is assumed to be low implying a high resistance to sliding for block A_I due to strong local ice–bed coupling.

from block A_S due to increased lubrication of the bed. At this point, any elastic

component of the deformation can be recovered, *i.e.*, block A_{I} snaps forward while block A_{S} snaps backward.

5.4.2.3 Mathematical formulation

We consider a glacier of thickness h_{I} that flows over a horizontal bed. The x axis is directed in the glacier flow direction and the z axis is vertical, pointing positive upward through the ice. With the two bed regions A and B as introduced in Section 5.4.2.1, the basal shear stress

$$\tau_{\mathrm{b}} = \rho_{\mathrm{I}}\, g\, h_{\mathrm{I}} \sin\theta \tag{5.1}$$

can be unevenly distributed on the bed so that

$$\tau_{\mathrm{b}} = \alpha\, \sigma^{\mathrm{A}}(x,y,0,t) + (1-\alpha)\, \sigma^{\mathrm{B}}(x,y,0,t) \tag{5.2}$$

where ρ_{I} is the density of ice, g is the gravitational acceleration, θ is the surface slope of the glacier and σ^{A} and σ^{B} represent the basal shear stresses in regions A and B, respectively. In the following we again base our analysis on the assumption that glacier flow obeys the linear sliding law as given in Equation (4.1), where the basal sliding velocity v_{b} is related to the basal shear stress τ_{b} by a drag coefficient f. With reference to Figure 5.9 we can then write down expressions for the shear stresses on region A

$$\sigma^{\mathrm{A}}(x,y,0,t) = f^{\mathrm{A}}\, \frac{\mathrm{d}}{\mathrm{d}t}(x_2 - x_1) \tag{5.3}$$

and region B

$$\sigma^{\mathrm{B}}(x,y,0,t) = f^{\mathrm{B}}\, \frac{\mathrm{d}x_3}{\mathrm{d}t} \tag{5.4}$$

where f^{A} and f^{B} are the drag coefficients for the connected and unconnected regions of glacier bed, respectively.
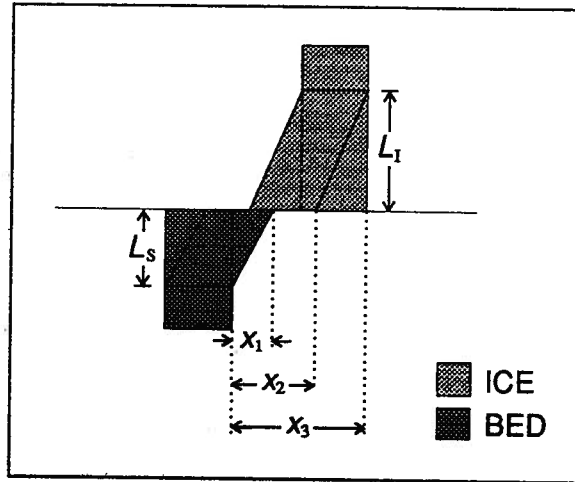
Fig. 5.9: Sideview of ice and substrate blocks showing dimensions and displacements of blocks (see text for details).

Furthermore, we consider that blocks A_I and A_S only deform elastically and completely ignore any creep deformation within the ice and viscous deformation of the sediment. As will be subsequently shown (see Section 5.4.2.5), this simplification is a serious shortcoming of the model. Nevertheless, with this assumption and noting that L_I and L_S are the strain equilibration distances in the ice and the substrate (see Fig. 5.9), we can easily write down stress–strain relations for block A_I

$$\sigma^A(x, y, 0, t) = \left(\frac{x_3 - x_2}{L_I} \right) \frac{G_I}{2} \tag{5.5}$$

and block A_S

$$\sigma^A(x, y, 0, t) = \frac{x_1}{L_S} \frac{G_S}{2} \tag{5.6}$$

where G_I and G_S denote the shear moduli of ice and substrate.

Substitution of Equations (5.5) and (5.6) into Equation (5.3) yields an equation which describes the motion of block A_I with respect to block A_S

$$\frac{d}{dt}(x_2 - x_1) = \frac{1}{2f^A} \frac{x_3 - (x_2 - x_1)}{\left(\dfrac{L_I}{G_I} + \dfrac{L_S}{G_S} \right)} \tag{5.7}$$

To obtain the corresponding equation of motion for block B_I we substitute Equations (5.4) and (5.7) into Equation (5.2)

$$\frac{dx_3}{dt} = \frac{\alpha - 2\tau_b}{2f^B(\alpha - 1)} \frac{x_3 - (x_2 - x_1)}{\left(\dfrac{L_I}{G_I} + \dfrac{L_S}{G_S}\right)} \tag{5.8}$$

5.4.2.4 Model results

Table 5.2 summarizes the model parameter values that were used to obtain the calculated solutions. Using an ice thickness of $h_I = 72\,\text{m}$, a surface slope of $\theta = 7°$ (Blake, 1992; Clarke and Blake, 1991) and a density of ice of $\rho_I = 900\,\text{kg}\,\text{m}^{-3}$ substituted into Equation (5.1), we calculated a mean basal shear stress for Trapridge Glacier of $\tau_b = 77\,\text{kPa}$. The drag coefficient for the unconnected region of the glacier bed was taken to be essentially an average constant value. In principle, it is the same as the background drag coefficient in Section 4.4.5; thus, we chose $f^B = 1.66 \times 10^{11}\,\text{Pa}\,\text{s}\,\text{m}^{-1}$. The areal distribution of connected and unconnected regions of the bed beneath Trapridge Glacier can be estimated from our drilling program. About 20–25% of holes drilled to the glacier bed appear to connect to the subglacial water system. We therefore assigned $\alpha = 0.2$ for the area fraction of the connected region in our model calculations. Elastic properties of ice are reasonably well known. Hobbs (1974, p. 258) and Sinha (1984) list values of the shear modulus of ice in the range 3.36×10^9–$3.80 \times 10^9\,\text{Pa}$. For our model calculations, we used $G_I = 3.4 \times 10^9\,\text{Pa}$. In contrast, elastic properties of soils are less well constrained. The shear modulus is found to depend on stress state as well as stress history of the particular soil sample (Yu and Richart, 1984). Typical values for sands and clays easily span one order of magnitude. An estimate of the shear modulus of Trapridge sediment can be calculated from the results of seismic reflection studies conducted on Ice Stream B (Blankenship and others, 1986, 1989). The shear wave

velocity of $v_s = 150\,\text{m}\,\text{s}^{-1}$ measured in the till layer immediately beneath the ice and an assumed substrate density of $\rho_S = 2000\,\text{kg}\,\text{m}^{-3}$ substituted into

$$v_s = \left(\frac{G_S}{\rho_S}\right)^{\frac{1}{2}} \tag{5.9}$$

yields a theoretical estimate of the shear modulus of the substrate $G_S = 4.5 \times 10^7\,\text{Pa}$. The values for the strain equilibration distance in ice and in the substrate were determined on a trial and error basis to yield the final results.

Parameter	Symbol	Value	Units
Basal shear stress	τ_b	77	kPa
Drag coefficient for region B	f^B	1.66×10^{11}	$\text{Pa}\,\text{s}\,\text{m}^{-1}$
Area fraction of connected region	α	0.2	
Shear modulus of ice	G_I	3.4×10^9	Pa
Shear modulus of substrate	G_S	4.5×10^7	Pa
Strain equilibration distance in ice	L_I	50	m
Strain equilibration distance in bed	L_S	3	m

Table 5.2: Parameters for the elastic block model.

To simulate the variable resistance to sliding in the connected region of the glacier bed in response to varying subglacial water pressures, a pressure dependence was included in the calculation of the drag coefficient f^A. However, from inspection of Figures 5.2a and 5.2b, we note that the strain build-up in the ice is only released after a certain threshold level of subglacial water pressure has been reached. For this reason, a simple linear inverse relationship between drag coefficient and subglacial water pressure, as had been used in Section 4.4.5, is not appropriate for these model calculations. Figure 5.10 shows a composite plot of data from pressure sensor 92P06 (Fig. 5.2b) and displacement record from drag spool 92SM02 (Fig. 5.2a) where we have also identified the strain release events by arrows. Examination of these strain release events shows that these occur over a range of water pressures and there is no clearly defined trigger level at which ice slip is initiated. We are not perplexed by this behaviour because the

slip condition is probably stochastic rather than deterministic so that each slip event is distinct from previous ones. Due to our inability to identify an obvious condition for strain release, we take the trigger levels of water pressure for ice slip initiation as known *a priori*. We incorporated the strain build-up followed by the slip initiation by calculating the drag coefficient as a function of subglacial water pressure, $f^A(p_W)$, as follows (Fig. 5.11)

$$f^A(p_W) = \begin{cases} a^+ p_W + b^+ & p_W < p_W^{\text{trig}+} \\ a^\pm p_W + b^\pm & p_W^{\text{trig}+} \leq p_W \leq p_W^{\text{trig}-} \\ a^- p_W + b^- & p_W > p_W^{\text{trig}-} \end{cases} \tag{5.10}$$

where $p_W^{\text{trig}+}$ denotes the threshold level for slip initiation, $\delta = p_W^{\text{trig}-} - p_W^{\text{trig}+}$ is the transition zone over which most of the ice slip occurs and (see Table 5.3 for parameter values)

$$a^+ = -\frac{f_{\max}^A - f_{\text{trig}+}^A}{p_W^{\max} - p_W^{\min}}, \qquad b^+ = \frac{f_{\max}^A + f_{\text{trig}+}^A}{2} - a^+ \frac{p_W^{\max} + p_W^{\min}}{2} \tag{5.11}$$

$$a^- = -\frac{f_{\text{trig}-}^A - f_{\min}^A}{p_W^{\max} - p_W^{\min}}, \qquad b^- = \frac{f_{\text{trig}-}^A + f_{\min}^A}{2} - a^- \frac{p_W^{\max} + p_W^{\min}}{2} \tag{5.12}$$

$$a^\pm = -\frac{f_{\max}^A - f_{\min}^A}{p_W^{\text{trig}-} - p_W^{\text{trig}+}}, \qquad b^\pm = \frac{f_{\max}^A + f_{\min}^A}{2} - a^\pm \frac{p_W^{\text{trig}-} + p_W^{\text{trig}+}}{2} \tag{5.13}$$

Parameter	Symbol	Value	Units
Maximum subglacial water pressure	p_W^{max}	76	$m(H_2O)$
Minimum subglacial water pressure	p_W^{min}	23	$m(H_2O)$
Maximum drag coefficient for region A	f_{max}^A	3.0×10^{11}	$Pa\,s\,m^{-1}$
Minimum drag coefficient for region A	f_{min}^A	0	$Pa\,s\,m^{-1}$
Drag coefficient at p_W^{max} (upper line)	f_{trig+}^A	2.0×10^{11}	$Pa\,s\,m^{-1}$
Drag coefficient at p_W^{min} (lower line)	f_{trig-}^A	1.0×10^{11}	$Pa\,s\,m^{-1}$
Transition zone for ice slip	δ	1	$m(H_2O)$

Table 5.3: Parameters for calculation of drag coefficient for region A.

For water pressures below the trigger level p_W^{trig+}, the drag coefficient does not change significantly; once the water pressure reaches the trigger level, there is a dramatic drop in drag coefficient (Fig. 5.11). The threshold level for slip initiation can be altered by shifting the steep section (transition zone) in Figure 5.11 along the water pressure axis.
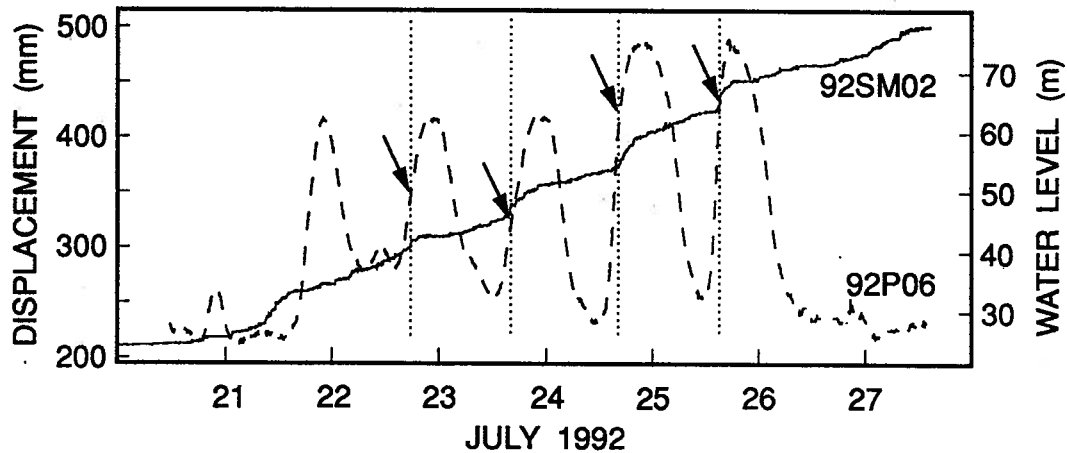

Fig. 5.10: Displacement record from drag spool 92SM02 (same as Figure 5.2a) and data from water pressure sensor 92P06 (dashed line, same as Figure 5.2b). Arrows indicate our identification of the trigger levels of water pressure for strain release events.
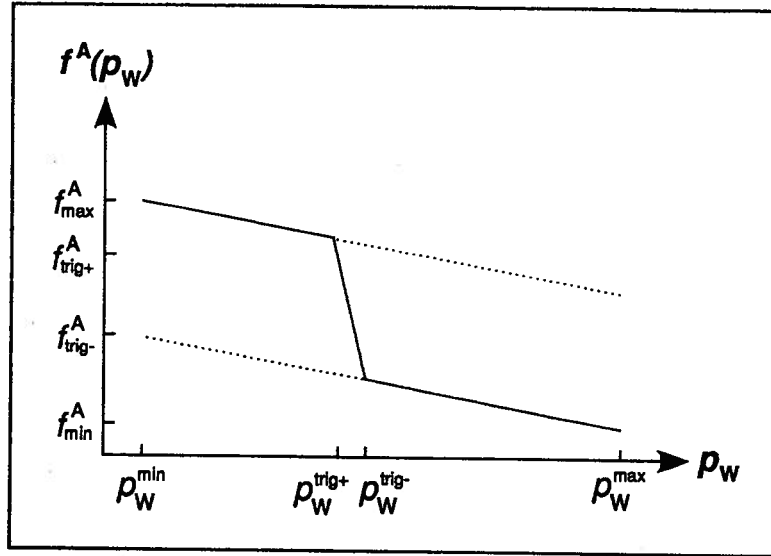
Fig. 5.11: Relationship between the drag coefficient for the connected region of glacier bed f^A and subglacial water pressure p_W.

Figure 5.12 shows the results from our calculations using the elastic block model. The computed displacement of block A_I (Fig. 5.12a) displays a remarkable similarity to the field data from 92SM02. At the same time, the motion of block B_I (Fig. 5.12b) appears to be characteristic of the responses that have been recorded with other drag spools (*i.e.*, linearly increasing displacement without distinct diurnal signal) (see Fig. 5.4).

5.4.2.5 Discussion

The assumption that glacier ice and substrate only deform elastically is certainly a gross over-simplification because our model only takes into account the short-term responses of ice and sediment. We essentially ignore any long-term responses such as those of a Glen-law viscous fluid in the case of ice. The deformation behaviour of ice is found to have a complex time-dependence. Sinha (1978, 1981) investigated and analyzed the
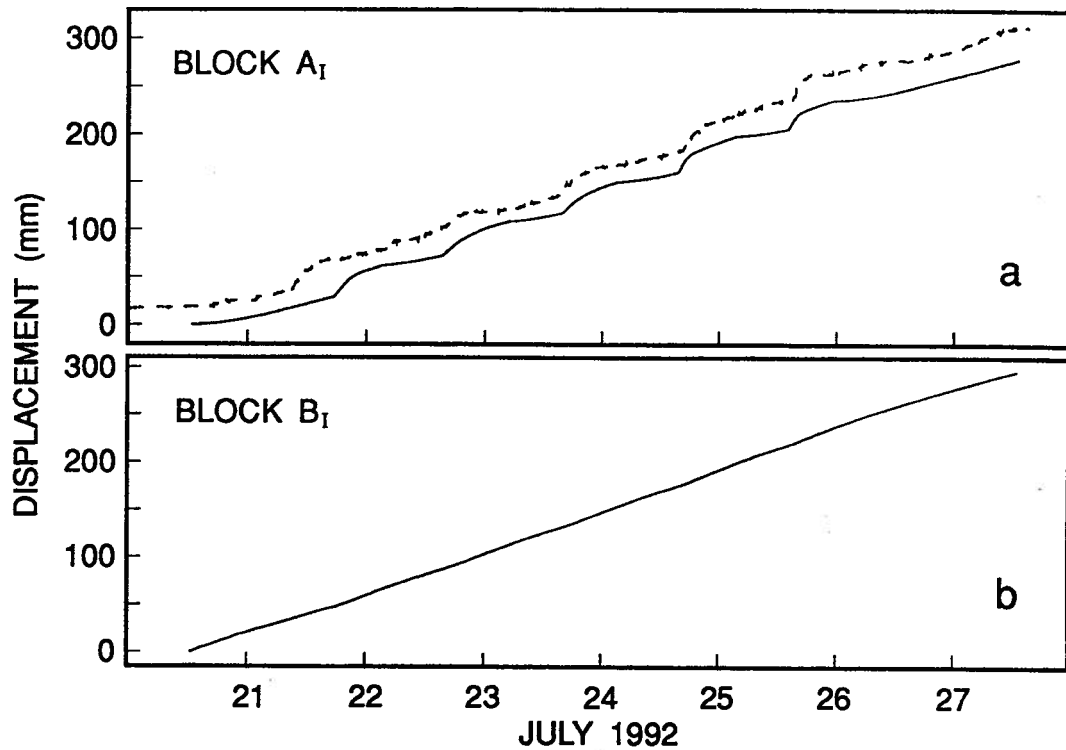
Fig. 5.12: Computed displacements of (a) block A_I and (b) block B_I. Note the similarity of the displacement record of block A_I to that as measured with drag spool 92SM02 (included for comparision in (a), dashed line).

phenomenological viscoelasticity of polycrystalline ice and showed that ice creep under uniaxial compression is composed of an instantaneous elastic response followed by a delayed elastic and viscous deformation. Therefore, the question of whether viscoelastic relaxation of elastic strain proceeds so rapidly that elastic strain cannot be accumulated effectively, has to be examined.

To simplify the following analysis, we approximate the transient rheological behaviours of ice and sediment by assuming that both behave as viscoelastic Maxwell materials. In this case, the viscoelastic relaxation time (Malvern, 1969, p. 315) for ice is given by

$$\tau_I = \frac{\eta}{G_I} \tag{5.14}$$

and for sediment by

$$\tau_S = \frac{\mu}{G_S} \tag{5.15}$$

where η and μ denote the effective linear viscosities of ice and sediment, respectively. For 0°C ice we had previously (see Section 4.4.5) calculated a dynamic viscosity of $\eta = 1.24 \times 10^{13}\,\mathrm{Pa\,s}$ which substituted in Equation (5.14) yields a lower limit on the viscoelastic relaxation time of $\tau_I = 1.0\,\mathrm{h}$. For Trapridge Glacier in the region of this study, the melting point is reached only near the bed and upper layers consist of cold ice with below-freezing temperatures. Taking $B = 1.6 \times 10^{15}\,\mathrm{s^{-1}\,kPa^{-3}}$ (parameter value from Paterson (1994, p. 97) for −5°C ice) in Equation (4.26) yields an upper limit on the stiffness of the flow law and gives the dynamic viscosity as $\eta = 5.27 \times 10^{13}\,\mathrm{Pa\,s}$. For this colder and stiffer ice, the relaxation time increases to $\tau_I = 4.3\,\mathrm{h}$. Similarly, we can calculate upper and lower limits on the viscoelastic relaxation time for the substrate by substituting our estimates of the linear viscosities for Trapridge sediment (see Chapter 2) into Equation (5.15). For viscosities μ between $3.0 \times 10^9\,\mathrm{Pa\,s}$ and $3.1 \times 10^{10}\,\mathrm{Pa\,s}$ (see Section 2.4.2.1), we calculated relaxation times τ_S ranging from 0.02 h to 0.19 h.

Although viscoelastic relaxation in ice is unlikely to proceed so rapidly that the elastic strain build-up is completely cancelled out, accumulation of elastic strain in the substrate over time scales of days cannot operate because of the short relaxation times. At first glance it might be tempting to use sediment viscosities that are an order of magnitude higher than our estimates (*e.g.*, those inferred from work done by Boulton and Hindmarsh (1987) beneath Breidamerkurjökull in Iceland) to calculate viscoelastic relaxation times τ_S of the order of hours. Concerns about the suitability of our model, however, remain. While the sediment layer beneath Trapridge Glacier is believed to be up to ~10 m thick in places (Stone, 1993), we think that a strain equilibration distance of $L_S = 3\,\mathrm{m}$ (see Table 5.2) is inconceivably high because measurements of

subglacial deformation (Blake and Clarke, 1989) suggest that the typical thickness of the deforming layer does not exceed 0.5 m. We could remove this concern by substituting a lower shear wave velocity into Equation (5.9) to yield a softer substrate with a lower shear modulus G_S. However, an already very low shear wave velocity of $v_s = 150\,\mathrm{m\,s^{-1}}$ is only found in very porous materials under low effective pressures. Although saturated with water at a high pore pressure, the porosity of the sediment layer beneath Trapridge Glacier is not believed to exceed that of Ice Stream B.

We note that our estimate of the shear modulus for the substrate G_S was obtained using a method based on the propagation of shear waves and therefore represents the dynamic value. However, in our case of a deforming subglacial sediment, a static shear modulus would be more appropriate. Nevertheless, dynamic methods that are based on seismic wave propagation remain applicable in estimating elastic properties provided we know how to relate the dynamic moduli to the moduli from static measurements. In laboratory studies, Brace (1965) and Simmons and Brace (1965) investigated the relationship between static and dynamic Young's moduli in diabase and granite and found that the dynamic modulus is about 20% greater than the static modulus for both rocks. Results from investigations on sandstones and shales (Cheng and Johnston, 1981; Jizba, 1991) show that the static moduli are generally lower than the dynamic ones. The discrepancy in moduli from static versus dynamic methods were found to be as large as a factor of five.

Despite the obvious shortcomings discussed above, the good fit that we were able to achieve between model results and field observations (Fig. 5.12) suggests that the elastic block model is successful in explaining the data that have been recorded with drag spool 92SM02 (Fig. 5.2a) and pressure sensor 92P06 (Fig. 5.2b). An attractive feature of our model is the potential ability to explain negative subglacial shear-strain rates observed at Trapridge Glacier (Blake, 1992) and Storglaciären (Iverson and others, 1995) during periods of high subglacial water pressures. The release of accumulated elastic strain

in the sediment as the ice becomes decoupled from the bed due to increased water lubrication (corresponding to the backwards snapping of block A_S (Fig. 5.8) in our model) could account for the observed up-glacier rotation of tilt sensors.

Chapter 6

SUMMARY AND CONCLUSIONS

*"Every great scientific truth goes through three stages. First, people say
it conflicts with the Bible. Next they say it had been discovered before.
Lastly they say they always believed it. "*

- Louis Agassiz

This thesis describes an investigation of mechanical conditions at the ice–bed interface of Trapridge Glacier, a surge-type glacier currently in the late quiescent phase. The study of basal conditions and processes that control the coupling between a glacier and its bed is of critical importance in understanding the dynamics of surging glaciers.

We have documented the development of two novel techniques for exploring the subglacial environment: measurements of sliding and of mechanical phenomena at the base of the glacier. Using these new techniques, we have recorded unique subglacial processes that had not been observed before. Our instruments enabled continuous and long-term measurements of basal sliding over a soft substrate and observation of mechanical processes at the ice–bed interface. Both instruments were devised bearing in mind sizes and shapes that permit their *in situ* installation at the bottom of narrow boreholes ($\sim$5 cm diameter). Other important features include their simplicity in design and low costs. It should therefore prove useful to deploy arrays of both types of instruments at various locations across the bed in order to study evolving conditions beneath normal and surge-type glaciers.

The 1991 ploughmeter measurements suggest that across the bed of Trapridge Glacier, either the texture of subglacial sediment is not uniform or ice-sediment coupling varies significantly. If one assumes that, at the scale of 10 m, lateral variations in

sliding velocity are insignificant, ploughmeter 91PL01 appears to have been immersed in a region of the bed that predominantly consists of fine-grained material, whereas ploughmeter 91PL02 seems to interact with a clast-rich sediment. We showed that by assuming simple model rheologies, we can use results from ploughmeter 91PL01 to calculate estimates of rheological parameters for Trapridge sediment: linear effective viscosity and plastic yield strength. We have also demonstrated that if the subglacial sediment texture is known, the collision frequency as indicated by ploughmeter 91PL02 can be used to obtain an estimate of the basal sliding velocity. Our analysis assumed temporal variations in sliding rate to be negligible and a spatially uniform sediment texture. In the case of Trapridge Glacier we were able to confirm our velocity estimates by comparing them with drag spool measurements.

We found that the particle-size distribution for Trapridge sediment obeys fractal statistics and shows clear power-law scaling behaviour over five orders of magnitude. The fractal dimension of $D = 2.95$ is consistent with those reported for other geological samples and suggests that Trapridge sediment is repeatedly subjected to abrasive grinding as it deforms under the applied shear stress of the glacier. This fractal scaling behaviour was used to extrapolate the grain-size distribution to larger size scales than those sampled and to examine the self-similar character of the ploughmeter response spectrum. Furthermore, using a fractal analysis, we have explored the possibility that the spectral characteristics of the ploughmeter response can be used to infer subglacial sediment texture, specifically the fractal dimension of the particle-size distribution. Regrettably, it was found that the mechanical response of a ploughmeter is only to a small extent a function of the size distribution in the sediment, as evidenced by the weak dependence of the fractal dimension of the ploughmeter response on the fractal dimension of the particle-size distribution.

Field data from our drag spool instruments suggest that, during the period of observation, up to 45–65% of the total flow observed at the glacier surface can be due

to basal sliding. With the contribution from ice creep known to be small, most of the remaining surface motion must be attributed to bed deformation processes.

We presented data recorded simultaneously during the 1992 field season with a water pressure sensor, a drag spool and two ploughmeters. The measurements indicate that the basal resistance beneath Trapridge Glacier is spatially and temporally variable but also suggest that the role of the subglacial water system appears to be complex and not always intuitive. We therefore developed a theoretical framework for the sliding motion of ice over a surface with basal resistance which we have allowed to vary. Based on our model calculations, we have shown that the strongly anti-correlated force responses in conjunction with in-phase azimuth responses of the two ploughmeters can be interpreted in terms of sticky spots being created and destroyed. These spatial and temporal variations of sticky spots are believed to be linked to changes in basal lubrication in response to fluctuations in subglacial water pressure. We have also demonstrated that the 90° phase shift between water pressure and sliding rate might be indicative of a stick–slip sliding process at the glacier base, whereby accumulated elastic strain in the ice is released as the rising water pressure decouples the ice from the bed. However, such an interpretation seems to require unrealistic assumptions about material properties, and so remains speculative.

Even though we have only demonstrated consistency on a scale of ~10 m for a single example, it is conceivable that high-drag, slow sliding sites exist all across the bed of Trapridge Glacier. Sticky patches appear to be created and destroyed in response to fluctuations in subglacial water pressure leading to time-varying lateral transfer of shear stress beneath the glacier. By associating high water pressures with slippery patches and low water pressures with sticky patches, we expect the stresses at the bed to form a patchwork distribution which is similar to the pressure distribution in the subglacial water system.

Based on our estimates of sediment strength as calculated from the ploughmeter results, we have suggested that the deformation resistance of the bed is comparable to but less than that needed to balance the applied driving stress. Because stresses are continuously redistributed on the bed, we also proposed that sticky patches do not dominate the force balance in our main study area of Trapridge Glacier and are thus likely candidates for supporting the remainder of the basal shear force required to ensure mechanical stability in this region of the glacier.

In summary, we have developed inexpensive and reliable sensors for directly monitoring mechanical conditions in a subglacial environment. Measurements taken with these sensors provided records of unique and heretofore unobserved basal processes. Such data are essential for improving our understanding of glacier dynamics. We have analyzed our measurements to assess rheological properties of subglacial sediment. Estimates of these properties constrain conditions that could be responsible for controlling the motion and stability of glaciers. To aid the interpretation of our field observations, we have developed models of how the ice flows in response to variations in basal drag. These models significantly furthered our understanding of coupling processes at the ice–bed interface. While many questions concerning the surge mechanism remain unanswered, the results and interpretation presented in this thesis provide a framework for current and future discussions of basal processes and their interaction with the subglacial hydrological system.

REFERENCES

Abramowitz, M. and I. A. Stegun, *eds.* 1965. *Handbook of mathematical functions with formulas, graphs, and mathematical tables.* Cambridge University Press, Cambridge.

Alley, R. B. 1989. Water–pressure coupling of sliding and bed deformation: II. Velocity–depth profiles. *J. Glaciol.*, **35**(119), 119–129.

Alley, R. B. 1993. In search of ice-stream sticky spots. *J. Glaciol.*, **39**(133), 447–454.

Alley, R. B., D. D. Blankenship, C. R. Bentley and S. T. Rooney. 1987. Till beneath Ice Stream B: 3. Till deformation: evidence and implications. *J. Geophys. Res.*, **92**(B9), 8921–8929.

Alley, R. B., S. Anandakrishnan, C. R. Bentley and N. Lord. 1994. A water-piracy hypothesis for the stagnation of Ice Stream C, Antarctica. *Ann. Glaciol.*, **20**, 187–194.

Anandakrishnan, S. and C. R. Bentley. 1993. Micro-earthquakes beneath Ice Streams B and C, West Antarctica: observations and implications. *J. Glaciol.*, **39**(133), 455–462.

Anandakrishnan, S. and R. B. Alley. 1994. Ice Stream C, Antarctica, sticky spots detected by microearthquake monitoring. *Ann. Glaciol.*, **20**, 183–186.

Atre, S. R. and C. R. Bentley. 1993. Laterally varying basal conditions under Ice Streams B and C, West Antarctica. *J. Glaciol.*, **39**(133), 507–514.

Batchelor, G. K. 1970. Slender-body theory for particles of arbitrary cross-section in Stokes flow. *J. Fluid Mech.*, **44**(3), 419–440.

Bennett, J. G. 1936. Broken coal. *J. Inst. Fuel*, **10**, 22-39.

Berry, M. V. and Z. V. Lewis. 1980. On the Weierstrass-Mandelbrot fractal function. *Proc. R. Soc. Lond.*, A(370), 459–484.

Blake, E. W. 1992. The deforming bed beneath a surge-type glacier: measurement of mechanical and electrical properties. (Ph.D. thesis, University of British Columbia).

Blake, E. W. and G. K. C. Clarke. 1989. In situ bed strain measurements beneath a surge-type glacier. *EOS*, **70**(43), 1084. [Abstract].

Blake, E. W., G. K. C. Clarke and M. C. Gérin. 1992. Tools for examining subglacial bed deformation. *J. Glaciol.*, **38**(130), 388–396.

Blake, E. W., U. H. Fischer and G. K. C. Clarke. 1994. Direct measurement of sliding at the glacier bed. *J. Glaciol.*, **40**(136), 595–599.

116

Blankenship, D. D., C. R. Bentley, S. T. Rooney and R. B. Alley. 1986. Seismic measurements reveal a saturated porous layer beneath an active Antarctic ice stream. *Nature*, **322**(6074), 54–57.

Blankenship, D. D., C. R. Bentley, S. T. Rooney and R. B. Alley. 1987. Till beneath ice stream B: 1. Properties derived from seismic travel times. *J. Geophys. Res.*, **92**(B9), 8903–8911.

Boulton, G. S. and R. C. A. Hindmarsh. 1987. Sediment deformation beneath glaciers: rheology and geological consequences. *J. Geophys. Res.*, **92**(B9), 9059–9082.

Boulton, G. S. and A. S. Jones. 1979. Stability of temperate ice caps and ice sheets resting on beds of deformable sediment. *J. Glaciol.*, **24**(90), 29–43.

Boulton, G. S., D. L. Dent and E. M. Morris. 1974. Subglacial shearing and crushing, and the role of water pressures in tills from south-east Iceland. *Geogr. Ann.*, **56A**(3-4), 135–145.

Brace, W. F. 1965. Some new measurements of linear compressibility of rocks. *J. Geophys. Res.*, **70**(2), 391–398.

Bracewell, R. N. 1986. *The Fourier transform and its application. Second edition.* McGraw-Hill Publishing Company, New York.

Brown, N. E., B. Hallet and D. B. Booth. 1987. Rapid soft bed sliding of the Puget Sound glacial lobe. *J. Geophys. Res.*, **92**(B9), 8985–8997.

Burridge, R. and L. Knopoff. 1967. Model and theoretical seismicity. *Seismol. Soc. Am. Bull.*, **57**, 341–371.

Byars, E. F., R. D. Snyder and H. L. Plants. 1983. *Engineering mechanics of deformable bodies. Fourth edition.* Harper and Row, New York.

Cao, T. and K. Aki. 1984. Seismicity simulation with a mass–spring model and a displacement hardening–softening friction law. *Pure Appl. Geophys.*, **122**, 10–24.

Cao, T. and K. Aki. 1986. Seismicity simulation with a rate-and-state friction law. *Pure Appl. Geophys.*, **124**, 487–513.

Carol, H. 1947. The formation of *roches moutonnées*. *J. Glaciol.*, **1**(2), 57–59.

Cheng, C. H. and D. H. Johnston. 1981. Dynamic and static moduli. *Geophys. Res. Let.*, **8**(1), 39–42.

Clarke, G. K. C. 1987. Subglacial till: a physical framework for its properties and processes. *J. Geophys. Res.*, **92**(B9), 9023–9036.

Clarke, G. K. C. 1991. Length, width and slope influences on glacier surging. *J. Glaciol.*, **37**(126), 236–246.

Clarke, G. K. C. and E. W. Blake. 1991. Geometric and thermal evolution of a surge-type glacier in its quiescent state: Trapridge Glacier 1969–1989. *J. Glaciol.*, **37**(125), 158–169.

Clarke, G. K. C., S. G. Collins and D. E. Thompson. 1984. Flow, thermal structure, and subglacial conditions of a surge-type glacier. *Can. J. Earth Sci.*, **21**, 232–240.

Clarke, G. K. C., J. P. Schmok, C. S. L. Ommanney and S. G. Collins. 1986. Characteristics of surge-type glaciers. *J. Geophys. Res.*, **91**(B7), 7165–7180.

Cohen, S. 1977. Computer simulation of earthquakes. *J. Geophys. Res.*, **82**, 3781–3796.

Cox, R. G. 1970. The motion of long slender bodies in a viscous fluid. Part 1. General theory. *J. Fluid Mech.*, **44**(4), 791–810.

Curran, D. R., D. A. Shockey, L. Seaman and M. Austin. 1977. Mechanics and models of cratering in earth media. *In* Eoddy, D. J., R. O. Pepin and R. P. Merrill, *eds. Impact and explosion carterway*, Pergamon Press, New York, 1057–1087.

Dieterich, J. H. 1972. Time-dependent friction as a possible mechanism for aftershocks. *J. Geophys. Res.*, **77**, 3771–3781.

Engelhardt, H. F., W. D. Harrison and B. Kamb. 1978. Basal sliding and conditions at the glacier bed as revealed by bore-hole photography. *J. Glaciol.*, **20**(84), 469–508.

Engelhardt, H. F., N. Humphrey, B. Kamb and M. Fahnestock. 1990a. Physical conditions at the base of a fast moving Antarctic ice stream. *Science*, **248**(4951), 57–59.

Engelhardt, H. F., N. Humphrey and B. Kamb. 1990b. Borehole geophysical observations on Ice Stream B, Antarctica. *Antarct. J. U.S.*, **25**(4), 80–82.

Feder, J. 1988. *Fractals*. Plenum Press, New York.

Fischer, U. H. and G. K. C. Clarke. 1992. Ploughing of subglacial sediment. *EOS*, **73**(43), 182. [Abstract].

Fischer, U. H. and G. K. C. Clarke. 1993. Hydro-mechanical control of ice–bed coupling. *EOS*, **74**(43), 263. [Abstract].

Fischer, U. H. and G. K. C. Clarke. 1994a. Ploughing of subglacial sediment. *J. Glaciol.*, **40**(134), 97–106.

Fischer, U. H. and G. K. C. Clarke. 1994b. Water pressure induced variations in glacier sliding. *EOS*, **75**(44), 221. [Abstract].

Fox, C. G. 1989. Empirically derived relationships between fractal dimension and power law spectra. *Pure Appl. Geophys.*, **131**(1/2), 1–29.

Fujiwara, A., G. Kamimoto and A. Tsukamoto. 1977. Destruction of basaltic bodies by high-velocity impact. *Icarus*, **10**, 277–288.

Gilbert, L. E. 1989. Are topographic data sets fractal?. *Pure Appl. Geophys.*, **131**(1/2), 241–254.

Haefeli, R. 1951. Some observations on glacier flow. *J. Glaciol.*, **1**(9), 496–500.

Happel, J. and H. Brenner. 1973. *Low Reynolds number hydrodynamics. Second edition.* Noordhoff International Publishing, Leyden.

Harrison, W. D. and B. Kamb. 1970. Direct measurement of sliding velocity at the base of a glacier. *EOS*, **51**(4), 431. [Abstract].

Harrison, W. D. and B. Kamb. 1973. Glacier bore-hole photography. *J. Glaciol.*, **12**(64), 129–137.

Hartmann, W. K. 1969. Terrestrial, lunar, and interplanetary rock fragmentation. *Icarus*, **10**, 201–213.

Hill, R. 1969. *The mathematical theory of plasticity.* Oxford University Press, Oxford.

Hobbs, P. V. 1974. *Ice physics.* Clarendon Press, Oxford.

Hooke, R. LeB., P. Holmlund and N. R. Iverson. 1987. Extrusion flow demonstrated by bore-hole deformation measurements over a riegel, Storglaciären, Sweden. *J. Glaciol.*, **33**(113), 72–78.

Hooke, R. LeB., P. Calla, P. Holmlund, M. Nilsson and A. Stroeven. 1989. A 3 year record of seasonal variations in surface velocity, Storglaciären, Sweden. *J. Glaciol.*, **35**(120), 235–247.

Hooke, R. LeB., V. A. Pohjola, P. Jansson and J. Kohler. 1992. Intra-seasonal changes in deformation profiles revealed by borehole studies, Storglaciären, Sweden. *J. Glaciol.*, **38**(130), 348–358.

Hooke, R. LeB. and N. R. Iverson. 1995. Grain-size distribution in deforming subglacial tills: role of grain fracture. *Geology*, **23**(1), 57–60.

Humphrey, N. F., H. F. Engelhardt, M. Fahnstock, and B. Kamb. 1993. Characteristics of the bed of the lower Columbia Glacier, Alaska. *J. Geophys. Res.*, **98**(B1), 837–846.

Iken, A. 1981. The effect of the subglacial water pressure on the sliding velocity of a glacier in an idealized numerical model. *J. Glaciol.*, **27**(97), 407–421.

Iken, A. and R. A. Bindschadler. 1986. Combined measurements of subglacial water pressure and surface velocity of Findelengletscher, Switzerland: conclusions about drainage system and sliding mechanism. *J. Glaciol.*, **32**(110), 101–119.

Iken, A., H. Röthlisberger, A. Flotron and W. Haeberli. 1983. The uplift of Unteraargletscher at the beginning of the melt season – a consequence of water storage at the bed?. *J. Glaciol.*, **29**(101), 28–47.

Iverson, N. R. 1993. Regelation of ice through debris at glacier beds: implications for sediment transport. *Geology*, 21(6), 559–562.

Iverson, N. R., P. Jansson and R. LeB. Hooke. 1994. In situ measurement of the strength of deforming subglacial till. *J. Glaciol.*, 40(136), 497–503.

Iverson, N. R., B. Hanson, R. LeB. Hooke and P. Jansson. 1995. Flow mechanism of glaciers on soft beds. *Science*, 267(5194), 80–81.

Jizba, D. L. 1991. Mechanical and accoustical properties of sandstones and shales. (Ph.D. thesis, Stanford University).

Kamb, B. 1970. Sliding motion of glaciers: theory and observation. *Rev. Geophys. Space Phys.*, 8(4), 673–728.

Kamb, B. 1991. Rheological nonlinearity and flow instability in the deforming bed mechanism of ice stream motion. *J. Geophys. Res.*, 96(B10), 16,585–16,595.

Kamb, B. and H. Engelhardt. 1987. Waves of accelerated motion in a glacier approaching surge: the mini-surges of Variegated Glacier, Alaska, U.S.A. *J. Glaciol.*, 33(113), 27–46.

Kamb, B. and H. Engelhardt. 1989. Flow mechanics of West Antarctic ice streams: observations by borehole geophysics. *EOS*, 70(43), 1081. [Abstract].

Kamb, B. and E. LaChapelle. 1964. Direct observation of the mechanism of glacier sliding over bedrock. *J. Glaciol.*, 5(38), 159–172.

Kamb, B. and E. LaChapelle. 1968. Flow dynamics and structure in a fast-moving icefall. *Trans. Am. Geophys. Union*, 49(1), 312. [Abstract].

Kamb, B., H. F. Engelhardt and W. D. Harrison. 1979. The ice–rock interface and basal sliding process as revealed by direct observation in bore holes and tunnels. *J. Glaciol.*, 23(89), 416–419. [Abstract].

Kamb, B., C. F. Raymond, W. D. Harrison, H. Engelhardt, K. A. Echelmeyer, N. F. Humphrey, M. M. Brugman and T. Pfeffer. 1985. Glacier surge mechanism: 1982–83 surge of Variegated Glacier, Alaska. *Science*, 227(4686), 469–479.

Kamb, B., H. Engelhardt, M. A. Fahnestock, N. Humphrey, M. Meier and D. Stone. 1994. Mechanical and hydrologic basis for the rapid motion of a large tidewater glacier 2. Interpretation. *J. Geophys. Res.*, 99(B8), 15231–15244.

Katz, A. J. and A. H. Thompson. 1985. Fractal sandstone pores: Implications for conductivity and pore formation. *Phys. Rev. Lett.*, 54, 1325–1328.

Kohler, J. and R. Proksch. 1991. *In-situ* measurement of subglacial till deformation beneath Storglaciären, N. Sweden. *EOS*, 72(44), 158. [Abstract].

Krohn, C. E. 1988a. Fractal measurements of sandstones, shales, and carbonates. *J. Geophys. Res.*, 93, 3297–3305.

Krohn, C. E. 1988b. Sandstone fractal and Euclidean pore volume distributions. *J. Geophys. Res.*, **93**, 3286–3296.

Krohn, C. E. and A. H. Thompson. 1986. Fractal sandstone pores: Automated measurements using scanning-electron microscope images. *Phys. Rev.*, **B33**, 6366–6374.

Lingle, C. S. and T. J. Brown 1987. A subglacial aquifer model and water pressure dependent basal sliding relationship for a West Antarctic ice stream. *In* Van der Veen, C. J. and J. Oerlemans, *eds. Dynamics of the West Antarctic Ice Sheet*, Riedel Publishers, Dordrecht, 249–285.

Lliboutry, L. 1968. General theory of subglacial cavitation and sliding of temperate glaciers. *J. Glaciol.*, **7**(49), 21–58.

Lliboutry, L. 1979. Local friction laws for glaciers: a critical review and new openings. *J. Glaciol.*, **23**(89), 67–95.

MacAyeal, D. 1992. The basal stress distribution of Ice Stream E, Antarctica, inferred by control methods. *J. Geophys. Res.*, **97**(B1), 595–603.

Malvern, L. E. 1969. *Introduction to the mechanics of a continuous medium*. Prentice-Hall, Englewood Cliffs.

Mandelbrot, B. B. 1983. *The fractal geometry of nature*. Freeman, New York.

Mathis, J. S. 1979. The size distribution of interstellar particles, II, Polarization. *Astrophys. J.*, **232**, 747–753.

Matsui, T., T. Waza, K. Kani and S. Suzuki 1982. Laboratory simulation of planetesimal collision. *J. Geophys. Res.*, **87**(B13), 10968–10982.

McCall, J. G. 1952. The internal structure of a cirque glacier: report on studies of the englacial movements and temperatures. *J. Glaciol.*, **2**(12), 122–130.

McKenzie, G. D. and D. N. Peterson. 1975. Correspondence. Subglacial cavitation phenomena: comments on the paper by R. Vivian and G. Bocquet. *J. Glaciol.*, **14**(71), 339–340.

Meier, M. F. and A. Post. 1969. What are glacier surges?. *Can. J. Earth Sci.*, **6**(4), 807–817.

Meier, M., S. Lundstrom, D. Stone, B. Kamb, H. Engelhardt, N. Humphrey, W. W. Dunlap, M. Fahnestock, R. M. Krimmel and R. Walters. 1994. Mechanical and hydrological basis for the rapid motion of a large tidewater glacier 1. Observations. *J. Geophys. Res.*, **99**(B8), 15219–15229.

Moore, C. A. and M. Krepfl. 1991. Using fractals to model soil fabric. *Géotechniq.*, **41**(1), 123–134.

Murray, T. and G. K. C. Clarke. 1995. Black-box modeling of the subglacial water system. *J. Geophys. Res.*, (in press).

Murray, W. M. and W. R. Miller. 1992. *The bonded electrical resistance strain gage.* Oxford University Press, New York.

Oberbeck, A. 1876. Über stationäre Flüssigkeitsbewegungen mit Berücksichtigung der inneren Reibung. *Crelles J.,* **81**, 62–80.

Oseen, C. W. 1927. *Neuere Methoden und Ergebnisse in der Hydrodynamik.* Akademische Verlagsgesellschaft M.B.H., Leibzig.

Paterson, W. S. B. 1994. *The physics of glaciers. Third edition.* Pergamon Press, Toronto.

Post, A. 1969. Distribution of surging glaciers in western North America. *J. Glaciol.,* **8**(53), 229–240.

Press, W. H., S. A. Teukolsky, W. T. Vetterling and B. P. Flannery. 1992. *Numerical recipes in fortran: the art of scientific computing. Second edition.* Cambridge University Press, Cambridge.

Raymond, C. F. 1971. Flow in a transverse section of Athabasca Glacier, Alberta, Canada. *J. Glaciol.,* **10**(58), 55–84.

Raymond, C. F. 1987. How do glaciers surge? A review. *J. Geophys. Res.,* **92**(B9), 9121–9134.

Rooney, S. T., D. D. Blankenship, R. B. Alley and C. R. Bentley. 1987. Till beneath Ice Stream B. 2. Structure and continuity. *J. Geophys. Res.,* **92**(B9), 8913–8920.

Ross, B. 1986. Dispersion in fractured fractal networks. *Water Resour. Res.,* **22**, 823–827.

Rundle, J. B. and D. D. Jackson. 1977. Numerical simulation of earthquake sequences. *Seismol. Soc. Am. Bull.,* **67**, 1363–1377.

Sammis, C. G. and R. L. Biegel. 1989. Fractals, fault-gouge, and friction. *Pure Appl. Geophys.,* **131**(1/2), 255–271.

Schlichting, H. 1979. *Boundary-layer theory. Seventh edition.* McGraw-Hill, New York.

Schoutens, J. E. 1979. Empirical analysis of nuclear and high-explosive cratering and ejecta, *In Nuclear Geoplosics Sourcebook.* **55**, part2, section 4, Rep. DNA OIH-4-2, Def. Nuclear Agency, Bethesda, MD.

Shabtaie, S., I. M. Whillans and C. R. Bentley. 1987. The morphology of Ice Streams A, B, and C, West Antarctica, and their environs. *J. Geophys. Res.,* **92**(B9), 8865–8883.

Sharp, M. 1988. Surging glaciers: behaviour and mechanisms. *Progr. Phys. Geog.,* **12**(3), 349–370.

Shoemaker, E. M. 1986. Subglacial hydrology for an ice sheet resting on a deformable aquifer. *J. Glaciol.,* **32**(110), 20–30.

Simmons, G. and W. F. Brace. 1965. Comparison of static and dynamic measurements of compressibility of rocks. *J. Geophys. Res.*, **70**(22), 5649–5656.

Sinha, N. K. 1978. Rheology of columnar-grained ice. *Exp. Mech.*, **18**(12), 464–470.

Sinha, N. K. 1981. Constant stress rate deformation modulus of ice, *In Proceedings, Sixth International Conference on Port and Ocean Engineering under Arctic Conditions.* I (POAC 81), 216–224.

Sinha, N. K. 1984. Intercrystalline cracking, grain-boundary sliding, and delayed elasticity at high temperatures. *J. Mat. Sci.*, **19**(2), 359–376.

Stokes, G. G. 1851. On the effect of the internal friction of fluids on the motion of pendulums. *Trans. Cambridge Philos. Soc.*, **9**, 8–106.

Stone, D. B. 1993. Characterization of the basal hydraulic system of a surge-type glacier: Trapridge Glacier, 1989–92. (Ph.D. thesis, University of British Columbia).

Tillet, J. P. K. 1970. Axial and transverse Stokes flow past slender axisymmetric bodies. *J. Fluid Mech.*, **44**(3), 401–417.

Thompson, A. H., A. J. Katz and C. E. Krohn. 1987. The microgeometry and transport properties of sedimentary rock. *Adv. Phys.*, **36**, 625–694.

Turcotte, D. L. 1986. Fractals and fragmentation. *J. Geophys. Res.*, **91**(B2), 1921–1926.

Turcotte, D. L. 1987. A fractal interpretation of topography and geoid spectra on the earth, moon, venus, and mars. *J. Geophys. Res.*, **92**(B4), E597–E601.

Turcotte, D. L. 1989. Fractals in geology and geophysics. *Pure Appl. Geophys.*, **131**(1/2), 171–196.

Turcotte, D. L. 1992. *Fractals and chaos in geology and geophysics.* Cambridge University Press, Cambridge.

Tyler, S. W. and S. W. Wheatcraft. 1989. Application of fractal mathematics to soil water retention estimation. *Soil Sci. Soc. Am. J.*, **53**(4), 987–996.

Tyler, S. W. and S. W. Wheatcraft. 1990. Fractal processes in soil water retention. *Water Resour. Res.*, **26**(5), 1047–1054.

Van der Veen, C. J. and I. M. Whillans. 1989. Force budget: II. Application to two-dimensional flow along Byrd Station strain network, Antarctica. *J. Glaciol.*, **35**(119), 61–67.

Vivian, R. and G. Bocquet. 1973. Subglacial cavitation phenomena under the Glacier d'Argentière, Mont Blanc, France. *J. Glaciol.*, **12**(66), 439–451.

Voss, R. F. 1985. Random fractal forgeries. *In* R. A. Earnshaw, *ed. Fundamental algorithms for computer graphics*, NATO ASI Series, **F17**, Springer-Verlag, Berlin, 805–835.

Waddington, B. S. 1992. Trapridge Glacier average annual velocity, as determined from survey data. (Internal report, University of British Columbia).

Weertman, J. 1964. The theory of glacier sliding. *J. Glaciol.*, **5**(39), 287–303.

Whillans, I. M., Y. H. Chen, C. J. Van der Veen and T. J. Hughes. 1989. Force budget: III. Application to three-dimensional flow of Byrd Glacier, Antarctica. *J. Glaciol.*, **35**(119), 68–80.

Yu, P. and F. E. Richart. 1984. Stress ratio effects on shear modulus of dry sands. *J. Geotech. Eng.*, **110**(3), 331–345.

Appendix A

FORCES ON AN ELONGATED BODY IN STOKES FLOW

For very small Reynolds numbers, inertial forces are negligible compared with the pressure and viscous forces. Thus, for a body having surface S at rest in an incompressible fluid which at infinity is undergoing a uniform translational motion at velocity $\mathbf{U}$, the velocity $\mathbf{v}$ and pressure p in the fluid satisfy the creeping motion equations (Schlichting, 1979, p. 112)

$$\mu \nabla^2 \mathbf{v} = \nabla p \qquad (A.1a)$$

$$\nabla \cdot \mathbf{v} = 0 \qquad (A.1b)$$

with the boundary conditions

$$\mathbf{v} = 0 \quad \text{on} \quad S \qquad (A.2a)$$

$$\mathbf{v} \to \mathbf{U} \quad \text{as} \quad \mathbf{x} \to \infty \qquad (A.2b)$$

where μ is the fluid viscosity and $\mathbf{x}$ the position vector of a general point. Oberbeck (1876) solved this problem in the case of an ellipsoid and obtained the total drag exerted on such a body. In particular, for an elongated ellipsoid of revolution having semi-axes a and c with $c > a$, Oberbeck's formula for fluid motion perpendicular to the symmetry axis leads to a drag of magnitude

$$F_D = \frac{16\pi\mu aU}{\left[\dfrac{c/a}{(c/a)^2 - 1} + \dfrac{2(c/a)^2 - 3}{[(c/a)^2 - 1]^{3/2}} \ln\left(\dfrac{c}{a} + \sqrt{(c/a)^2 - 1}\right) \right]} \qquad (A.3)$$

For large length-to-diameter ratios c/a, Equation (A.3) reduces to

$$F_D = \frac{8\pi\mu cU}{\ln(2c/a) + 0.5} \qquad (A.4)$$

Also, in the limit, as the length-to-diameter ratio c/a approaches unity, Oberbeck's solution (A.3) yields Stokes' law

$$F_{\mathrm{D}} = 6\pi\mu a U \qquad (A.5)$$

which describes the total drag of a sphere of radius a undergoing uniform translation through a viscous fluid (Stokes, 1851).

To obtain the force distribution along an elongated axisymmetric body moving perpendicularly through a viscous fluid, we follow the treatment by Batchelor (1970), which is based on slender-body theory for Stokes flow with negligible inertial forces. The key idea is that it is possible to approximate the body by a suitably chosen system of forces, known as "Stokeslets", distributed along the symmetry axis. The effect of these Stokeslets is to disturb the uniform motion of the surrounding fluid. For a force **F** applied at the origin in an infinite body of fluid, the velocity at the point **x** in flow with negligible inertial forces is (Oseen, 1927)

$$\frac{F_j}{8\pi\mu}\left(\frac{\delta_{ij}}{|\mathbf{x}|} + \frac{x_i x_j}{|\mathbf{x}|^3}\right) \qquad (A.6)$$

where μ is the fluid viscosity. Thus, if Stokeslets are distributed over the portion $-c < x_3 < c$ of the x_3 axis so that the line density of the applied force is $\mathbf{F}(x_3)$, the resulting fluid velocity at point **x** is

$$v_i(\mathbf{x}) = \frac{1}{8\pi\mu}\int_{-c}^{c}\left[\frac{F_i(x_3')}{\left((x_3 - x_3')^2 + r^2\right)^{1/2}} + \frac{(x_i - x_i')(x_j - x_j')F_j(x_3')}{\left((x_3 - x_3')^2 + r^2\right)^{3/2}}\right]\, dx_3' \quad (A.7)$$

where $x_1' = x_2' = 0$ and $r^2 = x_1^2 + x_2^2$. This distribution of Stokeslets represents the disturbance motion of an axisymmetric body of length $2c$, and points on the body surface are given by $r = a(x_3)$, where $a(x_3)$ is the radius of the body as a function of x_3 and $a(x_3)/c$ is small compared to unity. If we choose the axes of reference so that the body is stationary, the undisturbed velocity is $-\mathbf{U}$. This case corresponds to the translational motion of the body with velocity **U** through a fluid at rest at infinity.

In order to satisfy the no-slip condition of Equation (A.2), the resultant fluid velocity $\mathbf{v} - \mathbf{U}$ must be zero at the body surface. Thus, the unknown function $\mathbf{F}(x_3)$, representing the Stokeslet strength distribution, must be chosen so that the velocity due to the line of Stokeslets cancels the undisturbed velocity at all points on the surface of the body. It is possible to use a line distribution of Stokeslets as a means of satisfying the no-slip condition at points on the surface only if the body is slender. Thus, the integral Equation (A.7) with $\mathbf{v} = \mathbf{U}$ at $r = a(x_3)$ can be approximated by an asymptotic expansion in terms of the ratio of cross-sectional radius to body length $(a(x_3)/c \to 0)$ (Batchelor, 1970; Cox, 1970; Tillet, 1970). If the undisturbed velocity $\mathbf{U}$ is in the x_1 direction, the force per unit length on the body can be expressed as

$$F(x_3) = \frac{4\pi\mu U}{\ln(2c/a)} \left\{ \frac{2\ln(2c/a) - \frac{1}{2}\ln\left[\frac{a}{a(x_3)}\left(1 - \frac{x_3^2}{c^2}\right)^{1/2}\right]}{2\ln(2c/a) + 1} \right\} \qquad (A.8)$$

where a is the radius of the body at $x_3 = 0$.

In the particular case of an ellipsoidal body (Batchelor, 1970)

$$\frac{a(x_3)}{a} = \left(1 - \frac{x_3^2}{c^2}\right)^{1/2} \qquad \text{for} \qquad -c \le x_3 \le c \qquad (A.9)$$

and Equation (A8) reduces to

$$F(x_3) = \frac{4\pi\mu U}{\ln(2c/a) + 0.5} \qquad (A.10)$$

To obtain the total drag of the ellipsoid, we integrate Equation (A.10) over the length of the body. This yields

$$F_{\mathrm{D}} = \int_{-c}^{c} F(x_3)\,dx_3 = \frac{8\pi\mu cU}{\ln(2c/a) + 0.5} \qquad (A.11)$$

which corresponds to Oberbeck's result given in Equation (A.4). In the case of a cylindrical body, we substitute (Cox, 1970)

$$\frac{a(x_3)}{a} = 1 \qquad \text{for} \qquad -c \le x_3 \le c \qquad (A.12)$$

into Equation (A.8).